2010

Hard-Switching and Soft-Switching Two-Switch Flyback PWM DC-DC Converters and Winding Loss due to Harmonics in High-Frequency Transformers

Dakshina S. Murthy Bellur
Wright State University

HARD-SWITCHING AND SOFT-SWITCHING TWO-SWITCH FLYBACK PWM DC-DC CONVERTERS AND WINDING LOSS DUE TO HARMONICS IN HIGH-FREQUENCY TRANSFORMERS

A dissertation submitted in partial fulfillment

of the requirements for the degree of

Doctor of Philosophy

By

Dakshina Murthy Bellur

B. E., Visvesvaraya Technological University, Belgaum, India, 2003

M. S., Wright State University, Dayton, Ohio, 2006

2010

Wright State University

Abstract

Murthy Bellur, Dakshina. Ph.D., Engineering Ph.D. Program, Wright State University, 2010. *Hard-Switching and Soft-Switching Two-Switch Flyback PWM DC-DC Converters and Winding Loss due to Harmonics in High-Frequency Transformers.*

The flyback pulse-width modulated (PWM) DC-DC power converter is a very important circuit in switching mode power supply (SMPS) converters for low power applications. The main drawback of the conventional single-switch flyback converter is the high turn-off voltage stress suffered by the switch. The high voltage transients are caused by the resonant behavior of the transformer leakage inductance and the transistor output capacitance, resulting in ringing superimposed on the steady-state switch voltage level. This requires a transistor with higher voltage rating. However, a transistor with higher voltage rating has higher on-resistance causing higher conduction loss. The high voltage ringing also increases the switching loss. In addition, the switch voltage stress is not easily predictable because it is difficult to determine the magnitude of ringing during the design stage. The two-switch flyback DC-DC converter is an extended version of the single-switch flyback converter. The circuit arrangement with an addition of a power transistor and two clamping diodes to the conventional single-switch flyback converter leads to the two-switch flyback PWM DC-DC converter, which effectively reduces the switch overvoltage and eliminates the uncertainty of its value. The clamping diodes in the two-switch flyback converter clamps the voltage across each switch to the DC input voltage and also provide a path to return most of the energy stored in the transformer leakage inductance to the DC input source.

In the first part of this research, detailed steady-state analyses of the two-switch flyback PWM DC-DC converter for continuous conduction mode (CCM) and discontinuous conduction mode (DCM) are performed. The transistor output capacitance

and the transformer leakage inductance are included in the analyses. Design equations for both CCM and DCM operation modes are derived. Furthermore, by incorporating an active clamp circuit into the hard-switching two-switch flyback converter, a new soft-switching two-switch flyback converter, namely, zero-current transition (ZCT) two-switch flyback is proposed. The principle of circuit operation, steady-state analysis, equivalent circuits, converter steady-state waveforms, and design procedure of the proposed ZCT two-switch flyback converter is presented. The key features of the proposed soft-switching converter are 1) the voltage stresses of the main switches are reduced to DC input voltage V_I, and 2) all the semiconductor devices are turned off under zero-current (ZC) switching condition. Clamping of the switch overvoltages and reduction in switching loss are achieved in the proposed ZCT two-switch flyback converter. Saber Sketch simulation and experimental results of the hard-switching and the proposed ZCT soft-switching two-switch flyback converters are presented to validate the theoretical analyses.

High frequency (HF) transformers used in PWM converters, such as flyback transformers conduct periodic nonsinusoidal currents, which give rise to additional winding losses due to harmonics. In the second part of this research, a theory is developed to find the harmonic winding loss in an HF transformer conducting periodic nonsinusoidal current. Dowell's equation is used to determine the winding resistances due to eddy currents as a function of frequency. Both skin and proximity effects are taken into account. Fourier series of the primary and secondary current waveforms in a two-winding flyback transformer and the primary and secondary winding resistances are used to determine the primary and secondary winding power losses at various harmonics for both CCM and DCM cases, respectively. The harmonic winding loss factors F_{Rph} and F_{Rsh} are introduced. The theory is illustrated by the case study of flyback converter for both CCM and DCM operations. Using the equations developed

to find the winding losses due to harmonics, detailed methodology and step-by-step procedures to design two-winding flyback transformers for CCM and DCM operations, respectively, are given. Examples illustrating the design of two-winding flyback transformer for CCM and DCM operations are presented. Computed characteristics of the designed flyback transformer for a wide range of operating conditions of the flyback converter in CCM and DCM modes are presented.

Contents

List of Figures

List of Tables

Acknowledgements

To my mother Seegehalli Gopalakrishna Rao Sarala Devi,
to my father Bellur Krishnaswamy Subba Rao, and
to my wife Smitha Srinivasan

1 Introduction

1.1 Background

This dissertation is mainly divided into two parts. In the first part, principles of circuit operation, steady-state analyses, and design procedures of the hard-switching two-switch flyback converter and the proposed soft-switching zero-current transition (ZCT) two-switch flyback converter are presented. In the second part, the theory developed to find the winding loss due to harmonics in a high-frequency (HF) transformer, such as flyback transformer, conducting periodic nonsinusoidal current, and a step-by-step procedure to design a HF flyback transformer for both continuous conduction mode (CCM) and discontinuous conduction mode (DCM) are presented.

1.1.1 Part I: Hard-Switching and Soft-Switching Two-Switch Flyback PWM DC-DC Converters

The pulse-width modulated (PWM) DC-DC power converter is an integral part of switching-mode power supplies (SMPSs) widely used in any modern day electronic equipment which requires a DC supply. In all applications, input-to-output electrical isolation is required at the power supply stage in order to protect the loading device from input transients. For low power applications requiring electrical isolation, flyback and forward DC-DC converters are the most popular choices [1]-[11]. An HF transformer is used in flyback and forward converters to provide input-to-output electrical isolation. In a flyback converter, the magnetizing inductance of the HF transformer is utilized to store the energy required for power conversion, thereby eliminating the need for an additional inductor which is required in a forward converter. An additional winding is also required in the transformer of the forward converter to reset the residual magnetic flux in the transformer core. Thus, flyback PWM DC-DC converters are preferred over forward converters since the former is simpler and has fewer semiconductor and magnetic components than the latter. Flyback
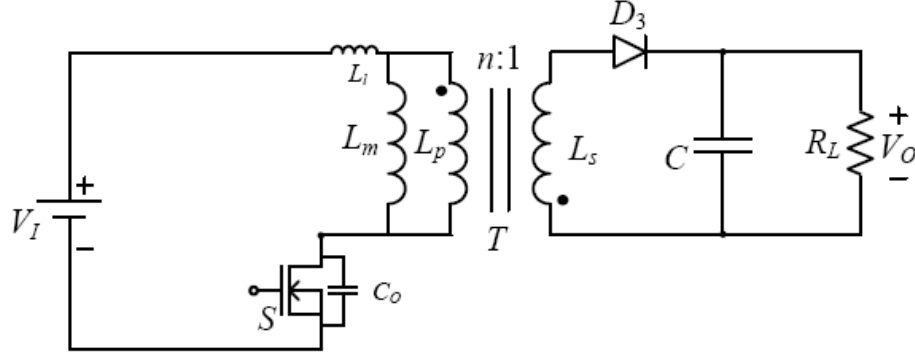
Figure 1.1: Classical single-switch flyback PWM DC-DC converter.

PWM DC-DC power converter is an important circuit extensively used in various electronic applications (< 250 W) [6]-[11], such as universal adapters/chargers for laptops and cell phones, battery charge equalizers, power supplies for telecommunication equipments, DVD players, Power-over-Ethernet (PoE), audio amplifiers, multiple output power supplies for charge-coupled devices (CCDs), TV set-top box, vacuum fluorescent displays (VFDs), LED displays, and cathode-ray tube TVs/monitors.

The circuit of the classical single-switch flyback PWM DC-DC converter is shown in Fig. 1.1. The circuit comprises a power transistor S used as a controllable switch, a HF transformer T modeled as an ideal transformer with its magnetizing inductance L_m referred to the primary side, and a rectifier diode D_3 (uncontrollable switch). The filter capacitor and the load resistance are denoted by C and R_L, respectively. The principle of circuit operation of an ideal flyback converter is mainly categorized into two time intervals. In the first time interval, the main switch S is turned on and the energy from the input source is stored in the transformer magnetizing inductance L_m while the rectifier diode D_3 remains off. In the second time interval, the switch S is turned off and the energy stored in L_m is transferred to the output via transformer T and the rectifier diode D_3. The maximum voltage stress of the main switch V_{SM} in an ideal flyback converter is the sum of the DC input and reflected DC output voltages

($V_I + nV_O$), where n is the HF transformer primary-to-secondary turns ratio. However, in a practical flyback converter circuit, the switch S suffers from higher voltage stress due to the resonance caused by the parasitic transformer leakage inductance L_l and the transistor output capacitance C_O, resulting in ringing superimposed on the steady-state ideal switch voltage of $V_I + nV_O$. Additionally, the ringing caused by the parasitic resonance also creates HF noise in the circuit, thereby increasing the problem of electromagnetic interference (EMI). In order to avoid the voltage breakdown of the switch S, a transistor with higher voltage blocking capability must be selected. A transistor with higher voltage rating is usually accompanied by higher on-resistance r_{DS}, which leads to higher conduction loss. The ringing also increases switching loss. Furthermore, the magnitude of the additional voltage stress caused by the ringing is not easily predictable as it depends on the value of the transformer leakage inductance and other stray inductances and capacitances in the circuit, which is also not easily predictable. Increased conduction and switching losses in the switch S leads to reduced converter efficiency.

Several techniques to mitigate the problems due to parasitic ringing in the classical flyback converter (or the single-switch flyback converter) are available in the literature. The earliest and the most commonly used techniques to reduce the magnitude of ringing are the dissipative Zener diode voltage clamp and the passive resistor-capacitor-diode (RCD) snubber [12]-[14]. In the Zener diode voltage clamp, a Zener diode and a clamping diode are connected back-to-back across the primary winding of the transformer to clamp the voltage across the switch S at turn-off. The maximum switch voltage stress in this case is $V_{SM} = V_I + nV_O + V_z$, where V_z is the Zener voltage. In the RCD passive clamp snubber, a parallel combination of R and C in series with the diode D is connected across the primary winding. The energy stored in the leakage inductance is dissipated in the snubber resistor R, reducing the converter
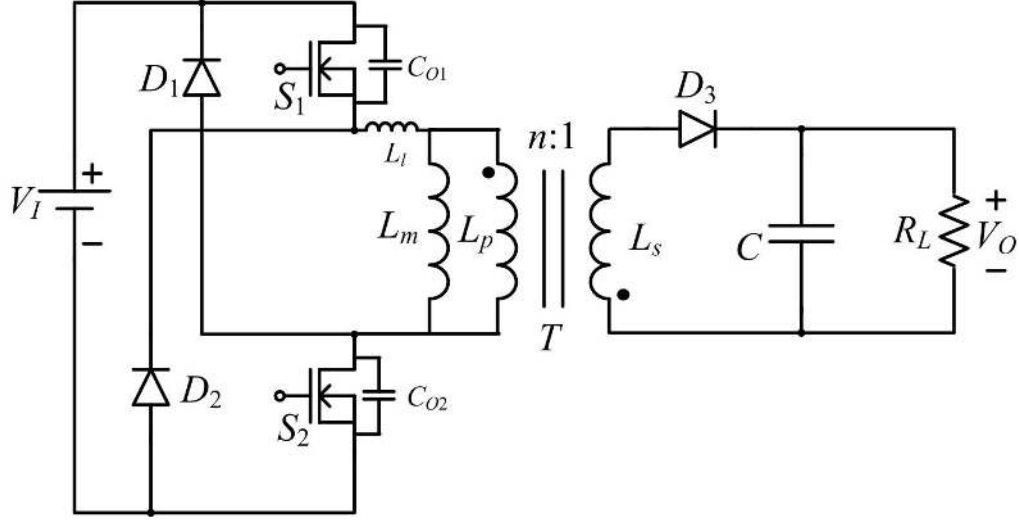
Figure 1.2: Two-switch flyback PWM DC-DC converter.

efficiency. The maximum voltage stress of the main switch is approximately $2V_I$.

In another technique, passive elements L and C are used in various combinations across the main switch and the primary winding of the flyback converter to transfer the leakage energy to either the input or the output. This type of snubber is known as the non-dissipative passive snubber [15]-[16]. The disadvantage of this type of snubber is that it increases the current stress of the main switch, while the voltage stress $V_{SM} \approx 2V_I$, thereby increasing the conduction loss. Recently, active clamp circuits have been extensively used to address the problem of ringing in single-switch flyback converters [17]-[23]. The active clamp circuit consists of a clamp capacitor and an additional active device such as a power MOSFET. The active clamp circuit effectively clamps the voltage across the switch to $V_{SM} = V_I + nV_O$ and also provides zero-voltage switching (ZVS) condition for both main and auxiliary switches, reducing switching losses, reducing EMI, and increasing the converter efficiency. The auxiliary switch of the active clamp circuit is driven complementarily with respect to the main switch to achieve ZVS condition. Incorporation of the active clamp circuit into the hard-switching single-switch flyback converter results in a soft-switching flyback converter.

A simpler alternative to passive and active clamp circuits used to remove ringing in the single-switch flyback converter is the two-switch flyback PWM DC-DC converter shown in Fig. 1.2 [40], [41], [1], [4], [5]. The two-switch flyback DC-DC converter is an extended version of the single-switch flyback converter. An additional switch and two clamping diodes serve as a simple, yet an effective way to limit the switch overvoltages. The clamping diodes which are cross connected across the primary winding effectively clamp the voltages across both the switches at turn-off and also provide a path to return the leakage inductance energy to the input source. The maximum voltage stress of the switch in a two-switch flyback converter is limited only to the DC input voltage V_I, reducing the switching and conduction losses. The additional switch is driven in phase with the main switch, thus making the control logic for the gate drive signal easier than that of the active clamp control circuit. Although the two-switch flyback converter is simpler and more advantageous than the single-switch flyback converter, there is neither analytical work nor design methodology of the two-switch flyback converter available in the literature. In this work, detailed steady-state analyses of the two-switch flyback converter including the parasitc transformer leakage inductance and the switch output capacitance is performed for both CCM and DCM operations. Based on the analyses, the design equations for the two-switch flyback converter for both CCM and DCM operations are derived. Furthermore, combining the reduced switch-voltage stress feature provided by the hard-switching two-switch flyback converter topology along with the soft-switching feature provided by the active clamp circuit, a new soft-switching two-switch flyback converter circuit, namely, *ZCT two-switch flyback PWM DC-DC converter* is proposed. The principle of circuit operation, steady-state analysis, equivalent circuits, and converter steady-state waveforms of the proposed soft-switching ZCT two-switch flyback converter is presented. The key features of the hard-switching and the soft-switching two-switch

flyback converters are listed below:

Hard-Switching Two-Switch Flyback PWM DC-DC Converter

1. The maximum switch voltage is clamped to the DC input voltage V_I.

2. The clamping diodes provide a path to return the transformer leakage energy into the DC input source.

3. The transistor turn-off switching loss is reduced.

Soft-Switching ZCT Two-Switch Flyback PWM DC-DC Converter

1. The maximum switch voltage is clamped to the DC input voltage V_I.

2. Zero-current (ZC) switching of all the switches and diodes.

3. Simple auxiliary circuit with low component count.

Based on the theoretical analyses presented and using the design procedure, the hard-switching and the soft-switching two-switch flyback converters are simulated in Saber Sketch circuit simulator. Experimental results from laboratory prototypes of the hard-switching and the ZCT soft-switching two-switch flyback converters are given to validate the theoretical analyses.

1.1.2 Part II: Harmonic Winding Loss in High-Frequency Transformers

Magnetic components such as inductors and transformers are an integral part of high efficiency, high power density power electronic equipments. They occupy more volume and are heavier when compared to other parts in a power electronic converter. In order to reduce the size of the magnetic components, the switching frequency of the PWM converters is increased. Increasing the switching frequency of the converter increases the transformer winding losses due to skin and proximity effects. Additionally, since PWM switching converters conduct nonsinusoidal currents, the losses due

to harmonics increase the winding power losses. The harmonic losses in transformer windings due to high-frequency (HF) operation also increase the operating temperature. HF transformers are widely used in power-factor correction and DC-DC power conversion applications [6]-[11].

Several studies on the effect of high-frequency operation in windings are available in the literature [24]-[38]. The equation for winding ac resistance caused by the skin and proximity effects due to sinusoidal current in a winding is presented in [24]-[26]. The theoretical analyses presented in [24]-[26] are further extended to nonsinusoidal (rectangular and trapezoidal) current waveforms in [27]-[30]. In [27]-[30], the Fourier analysis is applied to rectangular and trapezoidal current waveforms to obtain the winding power loss at harmonic frequencies and hence to obtain the total winding loss by adding all the losses calculated at each harmonic frequency along with the DC power loss. In the approach presented in [27]-[30], the winding power loss at each harmonic is calculated by the product of the square of the amplitude of current and the value of winding ac resistance at the corresponding harmonic. In another recently proposed method [34], the rms values of the current waveform and the rms value of its derivatives are used to find the ac resistance for several current waveforms. Approximate equations are derived in [34] to find the ratio of sum of ac and DC resistance to DC resistance for several current waveforms. The Fourier expansion of the flyback transformer current in PWM converters operating in either CCM or DCM has not been given in the literature. In this work, a general expression for the transformer winding power loss for periodic nonsinusoidal current waveform is presented. Dowell's equation is used to determine the winding resistance due to eddy currents as a function of frequency. Both skin and proximity effects are taken into account. Fourier series of the primary and secondary current waveforms in isolated DC-DC power converters and the primary and secondary winding resistances are used

to determine the primary and secondary winding power losses at various harmonics, respectively. The harmonic winding loss factors F_{Rph} and F_{Rsh} are introduced. The theory presented is illustrated by the case study of flyback converter operating in both CCM and DCM.

The design of HF transformers are not studied well in the literature. A procedure to design transformers for PWM DC-DC converters is available in [39]. However, the transformer design in [39] neither calculates the winding losses due to high-frequency effects nor due to harmonics. Incorporating the equations developed to calculate the winding power losses in an HF transformer, step-by-step procedures to design two-winding transformers operating in CCM and DCM modes, respectively, are presented. Criteria for the selection of transformer core and winding wire using the area product method for nonsinusoidal excitations are developed. Practical examples to design a two-winding flyback transformer for both CCM and DCM operations are given. The computed characteristics of the transformers designed are presented for a wide range of converter operating conditions.

1.2 Motivation

The requirement for compact, high efficiency, high density, low noise switching mode PWM DC-DC converters is ever increasing. The reduction in size of the PWM switching converters is mostly brought about by reducing the size of the magnetic components. This is primarily achieved by increasing the converter switching frequency which in turn has three major effects 1) the switching losses, which is directly proportional to the switching frequency, increases, thus reducing the converter efficiency, 2) the high speed switching action will increase EMI, and 3) the HF switching leads to additional winding losses due to eddy current phenomenon in the transformer winding. The analysis and design of the two-switch flyback converter including the transformer leakage inductance and the transistor output capacitance is not available

in the literature. Also, the Fourier expansion of the periodic nonsinusoidal current waveform of the flyback transformer, which is used to calculate the transformer winding loss, is not available in the literature. A deep understanding of the two-switch flyback converter is necessary to lay the platform for solving the problems due to parasitics and HF operation. Since the HF flyback transformer plays a vital role in the converter operation, a good HF transformer design is also necessary.

1.3 Objectives

The objectives of this work are:

1. To present a detailed steady-state analysis and design of hard-switching two-switch flyback PWM DC-DC converter including the parasitic transformer leakage inductance and switch output capacitance, for both CCM and DCM operation modes.

2. To validate the theoretical analysis of the hard-switching two-switch flyback converter by simulation and experiment.

3. To propose a soft-switching ZCT two-switch flyback PWM DC-DC converter.

4. To present the steady-state analysis and design of the proposed soft-switching ZCT two-switch flyback PWM DC-DC converter.

5. To validate the theoretical analysis of the ZCT soft-switching two-switch flyback converter by simulation and experiment.

6. To explore and investigate the HF effects on the winding losses of a transformer conducting periodic nonsinusoidal current.

7. To develop and present general expressions for winding power loss in a two-winding transformer conducting periodic nonsinusoidal current.

8. To derive specific expressions for winding power loss in a two-winding flyback transformer conducting periodic nonsinusoidal current for CCM and DCM operations.

9. To present a step-by-step procedure to design a HF two-winding flyback transformer, using the area product method.

10. To illustrate the theory of winding losses due to harmonics in HF transformers by presenting the case studies of two-winding transformer used in flyback converter for CCM and DCM operations, respectively, for the entire range of converter operating conditions.

1.4   Contents of the Dissertation

This dissertation is organized as follows. In Chapter 2, analysis and design of the hard-switching two-switch flyback PWM DC-DC converter for CCM and DCM operations, respectively, is given along with the simulation and experimental results. Chapter 3 presents the proposed ZCT soft-switching two-switching flyback converter along with the circuit operation, steady-state analysis, design procedure, simulation and experimental results. The theory of winding loss due to harmonics in HF transformers and the detailed design procedures and examples of the HF transformers are presented in Chapters 4 and 5, respectively. Conclusions and contributions follow in Chapter 6.

2 Hard-Switching Two-Switch Flyback PWM DC-DC Converter

2.1 Background

The two-switch flyback PWM DC-DC converter is an extended version of the conventional single-switch flyback converter. An additional switch and two clamping diodes serve as a simple, but an effective way to limit the switch overvoltages, which occur in the conventional single-switch flyback converter. This chapter presents a detailed steady-state analysis of the two-switch flyback converter for both CCM and DCM cases, respectively. The switch output capacitance and the transformer leakage inductance are included in the analysis. Current and voltage waveforms of all the components of the converter are given. Power losses in all the components are determined. A comparison of the power losses of the two-switch and the single-switch flyback converters is given. Design procedures and examples are also given. Simulation and experimental results of the two-switch flyback converter are presented for both CCM and DCM cases.

2.2 Circuit Description

The basic circuit of the two-switch flyback PWM DC-DC converter is shown in Fig. 2.1. In the figure, the two switches S_1 and S_2 are n-channel power MOSFETs whose output capacitances are denoted by C_{O1} and C_{O2}, respectively. The clamping diodes D_1 and D_2 are cross connected across the switches and the primary winding. The rectifier diode and the filter capacitor are denoted by D_3 and C, respectively. The input DC voltage and the load resistance are denoted by V_I and R_L, respectively. Both the switches S_1 and S_2 are turned on or off at the same time by a gate driver. The switching period T_s is given by $1/f_s$, where f_s is the switching frequency. The ratio of switch on-time t_{on} to the total period T_s is defined as the switch duty ratio
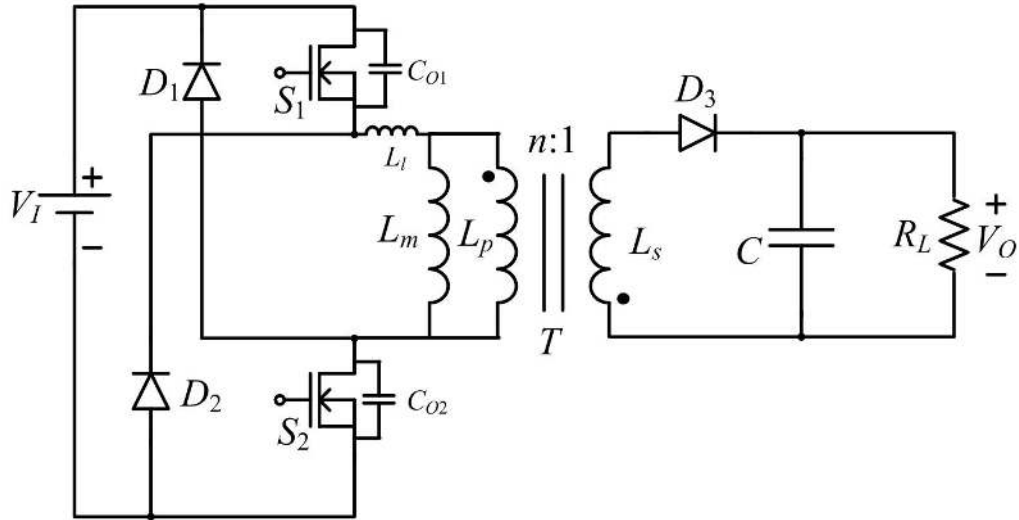
Figure 2.1: Two-switch flyback PWM DC-DC converter.

D. The transformer T is modeled as an ideal transformer with its magnetizing inductance L_m (referred to the primary) and the total leakage inductance L_l. To ease the mathematical analysis, the total transformer leakage inductance is referred to the primary. The transformer primary-to-secondary turns ratio is denoted by n.

2.3   Steady-State Analysis of Two-Switch Flyback Converter for CCM

2.3.1   Assumptions

The steady-state analysis of the two-switch flyback PWM converter of Fig. 2.1 is based on the following assumptions:

1. The power MOSFETs are ideal switches except for their output capacitances.

2. The diodes are ideal switches.

3. The diode capacitances and lead inductances are zero.

4. Passive components are linear, time-invariant, and frequency-independent.

5. The converter is operating in steady-state.

6. The switching period $T_s = 1/f_s$ is much smaller than the time constants of the reactive components.

7. Before the beginning of the switching cycle (time $t = t_0$), the magnetizing inductance current is commutated through the rectifier diode D_3, and all other switches and diodes are OFF.

2.3.2 Principle of Circuit Operation for CCM

The principle of operation of each stage is explained with the aid of equivalent circuits shown in Fig. 2.2 and the voltage and current waveforms of the converter shown in Fig. 2.3.

Stage 1 ($t_0 < t \leq t_1$): At time $t = t_0$, both the switches S_1 and S_2 are turned on by an external driver. The leakage inductance L_l prevents the instantaneous transfer of magnetizing current from the transformer secondary to the primary. Hence, the rectifier diode D_3 remains ON. An equivalent circuit for this stage is shown in Fig. 2.2(a). Since the voltage across the clamping diodes D_1 and D_2 is $-V_I$, the diodes D_1 and D_2 are reverse biased and hence their currents i_{D1} and i_{D2} are zero. The leakage inductance L_l limits the rate of rise of current through the switches S_1 and S_2. The voltage across the magnetizing inductance is $-nV_O$ from which the current through the magnetizing inductance is

$$i_{Lm} = -\frac{nV_O}{L_m}(t - t_0) + i_{Lm}(t_0),\tag{2.1}$$

where $i_{Lm}(t_0)$ is the initial current of the magnetizing inductance at time $t = t_0$. The voltage across the leakage inductance is $V_I + nV_O$. The current through the leakage inductance and the switches S_1 and S_2 are

$$i_{S1} = i_{S2} = i_{Ll} = \frac{V_I + nV_O}{L_m + L_l}(t - t_0) + i_{Lm}(t_0),\tag{2.2}$$

where $i_{Ll}(t_0) = 0$ is the initial value of the current in the leakage inductance at time $t = t_0$. The current through the switches and the leakage inductance rises linearly
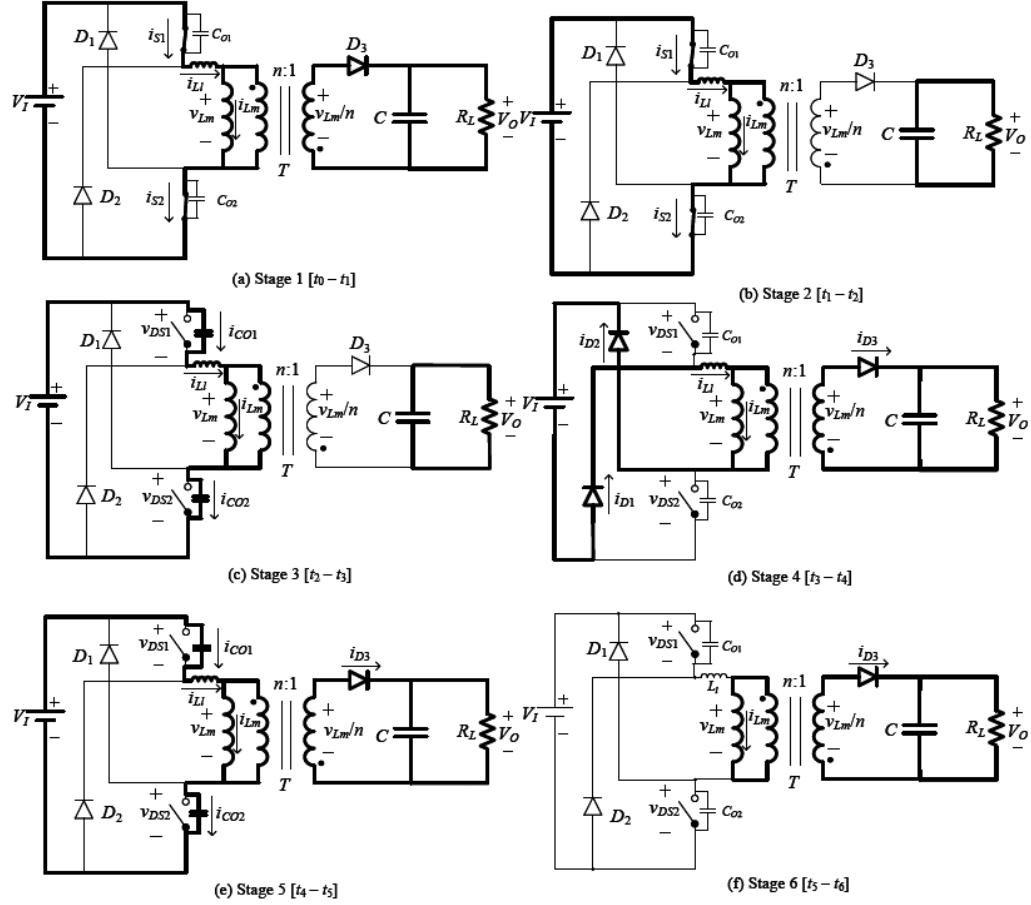
Figure 2.2: Equivalent circuits of the two-switch flyback converter for CCM at different stages of a switching cycle. (a) Stage 1 ($t_0 < t \leq t_1$). (b) Stage 2 ($t_1 < t \leq t_2$). (c) Stage 3 ($t_2 < t \leq t_3$). (d) Stage 4 ($t_3 < t \leq t_4$). (e) Stage 5 ($t_4 < t \leq t_5$). (f) Stage 6 ($t_5 < t \leq t_6$).

with a slope of $(V_I + nV_O)/L_l$. The current through the rectifier diode is

$$i_{D3} = -n(i_{Ll} - i_{Lm}) = -n\frac{V_I L_m + nV_O(L_m + L_l)}{L_m L_l}(t - t_0) + ni_{Lm}(t_0). \qquad (2.3)$$

Assuming $L_l \ll L_m$, the rectifier diode currents fall linearly with a slope of approximately $-n(V_I + nV_O)/L_l$. The voltages across the switches v_{DS1}, v_{DS2} and across the rectifier diode v_{D3} are zero. This stage ends at time $t = t_1$, when the current through the leakage inductance equals the magnetizing inductance current and the rectifier diode current reaches zero. Substituting $i_{D3} = 0$ into (2.3), the time period of the
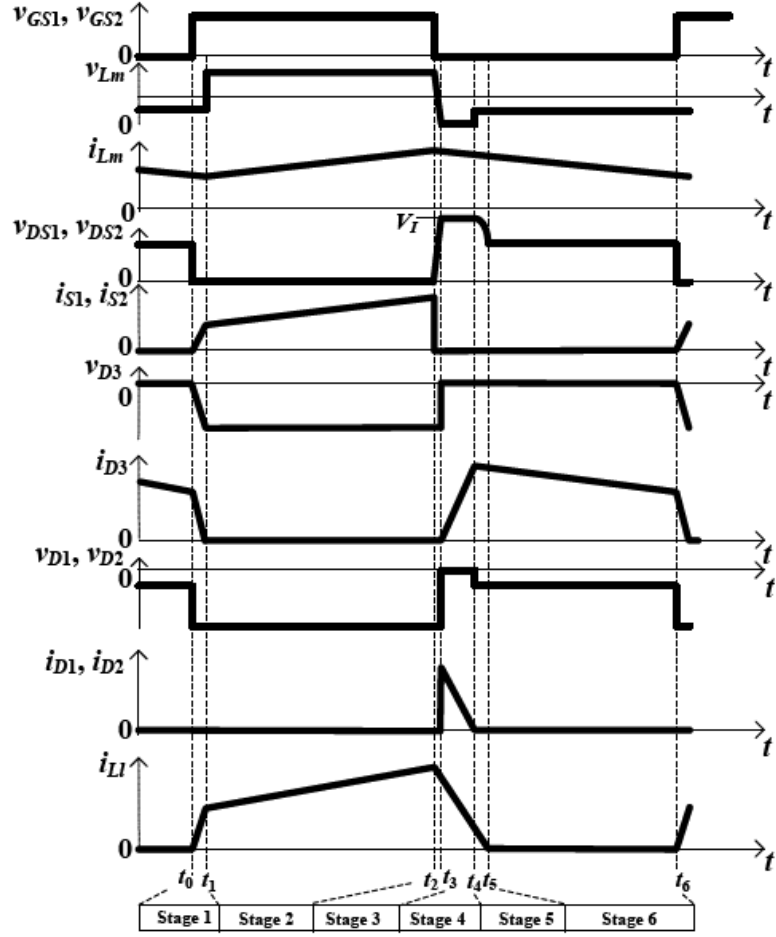
Figure 2.3: Voltage and current waveforms of the two-switch flyback PWM DC-DC converter for CCM.

first stage is obtained as

$$\Delta t_1 = t_1 - t_0 = \frac{L_l}{V_I + nV_O} i_{Lm}(t_0).$$

(2.4)

Stage 2 $(t_1 < t \leq t_2)$: During this stage the switches S_1 and S_2 are ON and all the diodes D_1, D_2 and D_3 are OFF. An ideal equivalent circuit of this stage is shown in Fig. 2.2(b). The current through the switches, leakage inductance, and the magnetizing inductance is

$$i_{S1} = i_{S2} = i_{Ll} = i_{Lm} = \frac{V_I}{L_m + L_l}(t - t_1) + i_{Lm}(t_1),$$

(2.5)

where $i_{Lm}(t_1)$ is the initial current of the magnetizing inductance at $t = t_1$. The current through the magnetizing inductance, leakage inductance, and the switches rises linearly with a slope of $V_I/(L_m + L_l)$. The voltages across the switches v_{S1} and v_{S2} are zero. The peak current of the magnetizing inductance is

$$i_{Lm}(t_2) = \frac{V_I DT}{L_m + L_l} + i_{Lm}(t_1) = \frac{V_I D}{f_s(L_m + L_l)} + i_{Lm}(t_1), \tag{2.6}$$

The peak-to-peak value of the ripple current through the magnetizing inductance is

$$\Delta i_{Lm} = i_{Lm}(t_2) - i_{Lm}(t_1) = \frac{V_I DT}{L_m + L_l} = \frac{V_I D}{f_s(L_m + L_l)}. \tag{2.7}$$

This stage ends at time $t = t_2$, when both the switches are turned off.

Stage 3 $(t_2 < t \leq t_3)$: During this stage, the switches S_1, S_2 and all the diodes D_1, D_2 and D_3 are OFF. An equivalent circuit for this stage is shown in Fig. 2.2(c). The magnetizing current (equal to the leakage current) charges the switch output capacitances C_{O1} and C_{O2} in a resonant manner. The current through C_{O1}, C_{O2}, the leakage inductance, and the magnetizing inductance is

$$i_{CO1} = i_{CO2} = i_{Ll} = i_{Lm} = \frac{V_I}{Z_1} \sin \omega_1(t - t_2) + i_{Lm}(t_2) \cos \omega_1(t - t_2), \tag{2.8}$$

where

$$Z_1 = \sqrt{\frac{(L_m + L_l)(C_{O1} + C_{O2})}{C_{O1}C_{O2}}} \tag{2.9}$$

and

$$\omega_1 = \sqrt{\frac{C_{O1} + C_{O2}}{C_{O1}C_{O2}(L_m + L_l)}}. \tag{2.10}$$

Assuming $C_{O1} = C_{O2} = C_O$, the switch voltages are

$$v_{DS1} = v_{DS2} = v_{CO1} = v_{CO2} = \frac{i_{Lm}(t_2)Z_1}{2} \sin \omega_1(t - t_2) - \frac{V_I}{2} \cos \omega_1(t - t_2). \tag{2.11}$$

This stage ends at time $t = t_3$, when the voltage across each switch equals V_I, thus turning on the clamping diodes D_1 and D_2.

Stage 4 ($t_3 < t \leq t_4$): During this stage, the switches S_1, S_2 are OFF, and all the diodes D_1, D_2, D_3 are ON. An equivalent circuit for this stage is depicted in Fig. 2.2(d). The voltage across each switch is clamped to $V_I + V_F$, where V_F is the forward voltage of the clamping diode. The current through the leakage inductance charges the input voltage source V_I via clamping diodes D_1 and D_2 given by

$$i_{D1} = i_{D2} = i_{Ll} = i_{Lm} = -\frac{V_I - nV_O}{L_l}(t - t_3) + i_{Ll}(t_3), \tag{2.12}$$

where $i_{Ll}(t_3)$ is the initial current of the magnetizing inductance at time t_3. This mode is referred to as regenerative clamping mode. This stage ends at time $t = t_4$, when the rectifier diode current i_{D3} equals the reflected magnetizing current ni_{Lm}, thereby turning off the clamping diodes D_1 and D_2.

Stage 5 ($t_4 < t \leq t_5$): During this stage, the switches S_1, S_2 and the diodes D_1, D_2 are OFF. The diode D_3 is ON. An equivalent circuit for this stage is depicted in Fig. 2.2(e). The resonant current through the leakage inductance L_l and the switch output capacitances C_{O1} and C_{O2} is

$$i_{Ll} = i_{CO1} = i_{CO2} = i_{Ll}(t_4)\cos\omega_2(t - t_4), \tag{2.13}$$

where $i_{Ll}(t_4)$ is the initial current of the leakage inductance at time instant t_4. The voltage across the leakage inductance is

$$v_{Ll} = -i_{Ll}(t_4)Z_2\sin\omega_2(t - t_4), \tag{2.14}$$

where

$$Z_2 = \sqrt{\frac{L_l(C_{O1} + C_{O2})}{C_{O1}C_{O2}}} \tag{2.15}$$

and

$$\omega_2 = \sqrt{\frac{C_{O1} + C_{O2}}{L_lC_{O1}C_{O2}}}. \tag{2.16}$$

The voltages across the switches are

$$v_{DS1} = v_{DS2} = v_{CO1} = v_{CO2} = V_I - i_{Ll}(t_4)Z_2\sin\omega_2(t - t_4). \tag{2.17}$$

This stage ends at time $t = t_5$, when the leakage inductance current i_{Ll} drops to zero.

Stage 6 $(t_5 < t \leq t_6)$: During this stage, the switches S_1, S_2 and the clamping diodes D_1, D_2 are OFF. The rectifier diode D_3 is ON. An equivalent circuit for this stage is depicted in Fig. 2.2(f). This stage is similar to *Stage* 5 except that the resonance between C_{O1}, C_{O2}, and L_l has stopped. The voltage across the magnetizing inductance is $-nV_O$. The current through the magnetizing inductance is

$$i_{Lm} = -\frac{nV_O}{L_m}(t - t_5) + i_{Lm}(t_5),\qquad(2.18)$$

where $i_{Lm}(t_5)$ is the initial current of the magnetizing inductance at $t = t_5$. The rectifier diode current is

$$i_{D3} = -\frac{n^2 V_O}{L_m}(t - t_5) + n i_{Lm}(t_5).\qquad(2.19)$$

Assuming that the switches S_1 and S_2 are identical, the voltages across the switches are

$$v_{DS1} = v_{DS2} = \frac{V_I + nV_O}{2}.\qquad(2.20)$$

Assuming that the clamping diodes D_1 and D_2 are identical, the voltages across the clamping diodes are

$$v_{D1} = v_{D2} = \frac{nV_O - V_I}{2}.\qquad(2.21)$$

The current through the switches i_{S1}, i_{S2}, the current through the clamping diodes i_{D1}, i_{D2}, and the leakage inductance current i_{Ll} are zero. This stage ends at time $t = t_6$, when the main switches S_1 and S_2 are turned on, thus completing one complete switching cycle. In Fig. 2.3, the time duration of *Stages* 1, 3, 4, and 5 are exaggerated for better understanding of the converter operation.

2.4   Design of Two-Switch Flyback Converter for CCM

2.4.1   DC Voltage Transfer Function

Referring to the voltage waveform of the magnetizing inductance in Fig. 2.3 and applying volt-second balance, we have

$$V_I \Delta t_2 = V_I(\Delta t_3 + \Delta t_4) + nV_O(\Delta t_1 + \Delta t_5 + \Delta t_6), \tag{2.22}$$

from which, the DC voltage transfer function of the converter is

$$M_{VDC} \equiv \frac{V_O}{V_I} = \frac{\Delta t_2 - (\Delta t_3 + \Delta t_4)}{n(\Delta t_1 + \Delta t_5 + \Delta t_6)}. \tag{2.23}$$

Assuming that the time duration of *Stages* 1, 3, 4, and 5 are very small in comparison with those of *Stages* 2 and 6, M_{VDC} can be approximated to

$$M_{VDC} \equiv \frac{V_O}{V_I} \approx \frac{\Delta t_2}{n\Delta t_6} = \frac{D}{n(1 - D)}. \tag{2.24}$$

2.4.2   Device Stresses

The selection of components is based on the maximum values of the voltage and current stresses of the switches and the diodes. During the fourth stage, the maximum off-state voltage appearing across S_1 and S_2 is

$$V_{SM1(\text{max})} = V_{SM2(\text{max})} = V_{I(\text{max})}. \tag{2.25}$$

During the sixth stage, the maximum off-state voltage appearing across S_1 and S_2 is

$$V_{SM1(\text{max})} = V_{SM2(\text{max})} = \frac{V_{I(\text{max})} + nV_O}{2} \tag{2.26}$$

During the second stage, the maximum value of the current through the switch is

$$I_{SM1(\text{max})} = I_{SM2(\text{max})} = \frac{I_{O(\text{max})}}{n(1 - D_{\text{max}})} + \frac{\Delta i_{Lm}}{2}, \tag{2.27}$$

where $I_{O(max)}$ is the maximum DC output current. During the second stage, the maximum value of the diode reverse voltage is

$$V_{DM3(\text{max})} = \frac{V_I}{n} + V_O. \tag{2.28}$$

At the end of the fourth stage, the maximum value of the current through the rectifier diode is approximately

$$I_{DM3(\text{max})} = \frac{I_{O(\text{max})}}{1 - D_{\text{max}}} + \frac{n\Delta i_{Lm}}{2}. \tag{2.29}$$

During the first and the second stages, the maximum value of the clamping diode reverse voltage is

$$V_{DM1(\text{max})} = V_{DM2(\text{max})} = V_{I(\text{max})}. \tag{2.30}$$

During the fourth stage, the maximum values of the current through the clamping diodes are

$$I_{DM1(\text{max})} = I_{DM2(\text{max})} = \frac{I_{O(\text{max})}}{n(1 - D_{\text{max}})} + \frac{\Delta i_{Lm}}{2}. \tag{2.31}$$

2.4.3 Design Procedure for CCM

The DC voltage transfer function of the two-switch flyback converter at the boundary between CCM and DCM is given by

$$M_{VDC} = \frac{V_O}{V_I} = \frac{\eta D}{n(1 - D)}, \tag{2.32}$$

from which, the transformer turns ratio is given by

$$n = \frac{\eta D_{\text{max}}}{M_{VDC(\text{max})}(1 - D_{\text{max}})}. \tag{2.33}$$

where D_{max} is the maximum duty cycle at the boundary between CCM and DCM and $M_{VDC(\text{max})} = V_O/V_{I(\text{min})}$. In (2.33), the maximum value of the duty cycle D_{max} is taken as 0.5 and M_{VDC} is calculated considering the desired converter efficiency η to be 90%. The peak voltage and current stresses of the devices on either side of the flyback transformer are influenced by n. The current and voltage stresses are minimal when n is selected such that D is 0.5. Hence, the value of n is calculated at $D_{\text{max}} = 0.5$. Furthermore, if the converter is operated for $D > 0.5$, the leakage inductance is charged for a longer period of time resulting in a longer duration of

the reset period (*Stage* 4), which in turn delays the transfer of energy stored in the magnetizing inductance to the load, thus reducing the converter efficiency.

The minimum value of the magnetizing inductance for CCM operation is given by

$$L_{m(\min)} = \frac{n^2 R_{L\max}(1 - D_{\min})^2}{2f_s}. \tag{2.34}$$

Using (2.25) - (2.31), the power MOSFETs and the diodes are selected. Selection of the output filter capacitor is based on the output voltage ripple specification.

$$C = \frac{D_{\max}V_O}{f_s R_{L\min}V_{cpp}}, \tag{2.35}$$

where V_{cpp} is the peak-to-peak value of the ac component of the voltage across the capacitance, which is approximately

$$V_{cpp} \approx V_r - V_{rcpp}. \tag{2.36}$$

In (2.36), V_r is the peak-to-peak value of the output ripple voltage (usually expressed as a percentage of DC output voltage V_O) and $V_{rcpp} = r_C I_{Cpp}$ is the peak-to-peak value of the voltage across the equivalent series resistance (ESR) r_C of the capacitor. The designed capacitor must be able to withstand the RMS capacitor current given by

$$I_{Crms} \approx I_O\sqrt{\frac{D}{1 - D}}. \tag{2.37}$$

The peak-to-peak value of the capacitor current is

$$I_{Cpp} \approx n\Delta i_{Lm} = \frac{nV_O(1 - D_{\min})}{f_s(L_m + L_l)}. \tag{2.38}$$

2.5 Power Losses and Efficiency of Two-Switch Flyback Converter for CCM

Equations for the power losses in the two-switch flyback converter are obtained by assuming that the time duration of *Stages* 1, 3, and 5 are very small. Using (2.5) and

(2.27), the rms value of the current through the switches is

$$I_{S1,S2(\text{rms})} = \sqrt{\frac{1}{T_s} \int_{t_0}^{t_1} i_{S1,S2} \, dt} = \frac{I_O \sqrt{D}}{n(1-D)}. \tag{2.39}$$

Assuming that the on-resistances of the switches $r_{DS1} = r_{DS2} = r_{DS}$, the total conduction loss in $2r_{DS}$ and primary winding resistance r_{T1} is

$$P_{ST1} = (2r_{DS} + r_{T1})I_{S1,S2(\text{rms})}^2 = (2r_{DS} + r_{T1})\frac{DI_O^2}{n^2(1-D)^2}. \tag{2.40}$$

Assuming that the output capacitances of the switches $C_{O1} = C_{O2} = C_O$ and using (2.25), the switch capacitive turn-off loss is given by

$$P_{SW} = \frac{1}{2} f_s (2C_O) V_{SM}^2 = f_s C_O V_I^2. \tag{2.41}$$

Using (2.19) and (2.29), the rms value of the current through the rectifier diode is

$$I_{D3(\text{rms})} = \sqrt{\frac{1}{T_s} \int_{t_2}^{t_6} i_{D3} \, dt} = \frac{I_O}{\sqrt{1-D}}. \tag{2.42}$$

The total conduction loss in the rectifier diode forward resistance R_{F3} and the secondary winding resistance r_{T2} is

$$P_{DT2} = (R_{F3} + r_{T2})I_{D3(\text{rms})}^2 = \frac{(R_{F3} + r_{T2})I_O^2}{1-D}. \tag{2.43}$$

The average value of the rectifier diode current $I_{D3} = I_O$, from which, the rectifier diode loss associated with the forward voltage of the rectifier diode V_{F3} is

$$P_{VF3} = V_{F3}I_{D3} = V_{F3}I_O. \tag{2.44}$$

Using (2.12) and (2.31), the rms value of the current through the clamping diodes is

$$I_{D1,D2(\text{rms})} = \sqrt{\frac{1}{T_s} \int_{t_3}^{t_4} i_{D1,D2} \, dt} = \frac{I_O}{n(1-D)} \sqrt{\frac{\Delta t_4}{T_s}}. \tag{2.45}$$

Assuming that the forward resistances of the clamping diodes $R_{F1} = R_{F2} = R_F$ and $\Delta t_4 = 10\% T_s$, the total conduction loss in $2R_F$ is

$$P_{RF} = 2R_F I_{D1,D2(\text{rms})}^2 = 2R_F \left(\frac{\Delta t_4}{T_s}\right) \frac{I_O^2}{n^2(1-D)^2} \approx \frac{0.2R_F I_O^2}{n^2(1-D)^2}. \tag{2.46}$$

The average value of the clamping diode current is

$$I_{D1} = I_{D2} = I_D = \frac{1}{T_s} \int_{t_3}^{t_4} i_D \, dt = \frac{I_O}{n(1-D)} \left(\frac{\Delta t_4}{T_s}\right). \tag{2.47}$$

Assuming that the forward voltage of the clamping diodes $V_{F1} = V_{F2} = V_F$ and $\Delta t_4 = 10\% T_s$, the total loss associated with the forward voltages of two clamping diodes together is

$$P_{VF} = 2V_F I_D = \frac{2V_F I_O}{n(1-D)} \left(\frac{\Delta t_4}{T_s}\right) \approx \frac{0.2V_F I_O}{n(1-D)}. \tag{2.48}$$

Using (2.5), (2.18), and (2.27), the rms value of the current through the magnetizing inductance is approximately

$$I_{L(\text{rms})} \approx I_I + \frac{I_O}{n} = \frac{I_O}{n(1-D)}. \tag{2.49}$$

The power loss in the equivalent series resistance (ESR) r_L of the magnetizing inductance is

$$P_{rL} = r_L I_{Lm(\text{rms})}^2 = \frac{r_L I_O^2}{n^2(1-D)^2}. \tag{2.50}$$

The total power loss in the two-switch flyback converter for CCM is

$$P_{LS} = P_{ST1} + P_{SW} + P_{DT2} + P_{VF3} + P_{RF} + P_{VF} + P_{rL}. \tag{2.51}$$

The efficiency of the two-switch flyback converter for CCM is

$$\eta \equiv \frac{P_O}{P_I} = \frac{P_O}{P_O + P_{LS}} = \frac{1}{1 + \frac{P_{LS}}{P_O}}. \tag{2.52}$$

2.6 Simulation and Experimental Results of Two-Switch Flyback Converter for CCM

The hard-switching two-switch flyback converter for CCM is designed for the following specifications:

- Maximum input voltage: $V_{Imax} = 50 \pm 10$ V
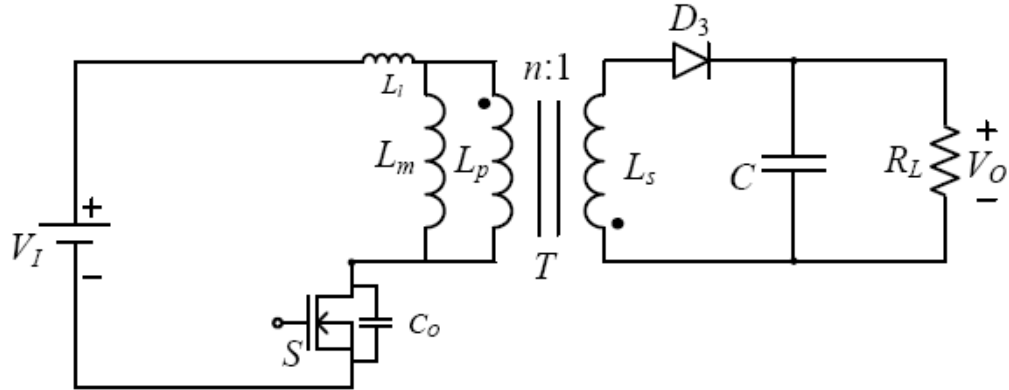
Figure 2.4: Single-switch flyback PWM DC-DC converter without RCD snubber.
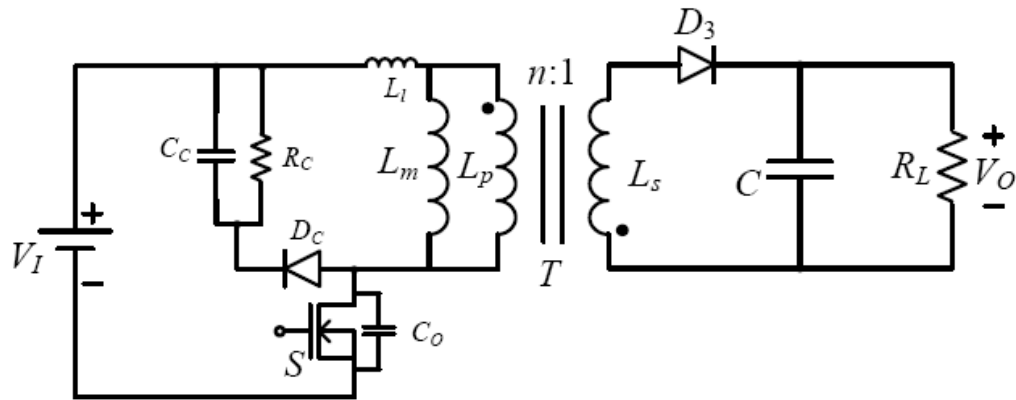
Figure 2.5: Single-switch flyback PWM DC-DC converter with RCD snubber.

- Output voltage: $V_O = 10$ V

- Maximum output power: $P_{Omax} = 30$ W

- Minimum output power: $P_{Omin} = 3$ W

- Switching frequency: $f_s = 100$ kHz

- Output voltage ripple: $V_r/V_O \leq 5\%$

The two-switch flyback converter for CCM is designed using equations (2.25) - (2.35). The components selected for the experiment and their specifications are given

Table 2.1: LIST OF COMPONENTS AND THEIR SPECIFICATIONS FOR TWO-SWITCH
FLYBACK CONVERTER FOR CCM

Parameter	Value	Component
Power MOSFET maximum voltage stress	60 V	IRF510 - 100 V
Power MOSFET maximum current stress	1.99 A	IRF510 - 5 A
Power MOSFET drain-to-source on-resistance	r_{DS}	IRF510 - 0.54 Ω
Power MOSFET drain-to-source capacitance	C_O	IRF510 - 60 pF
Rectifier diode maximum voltage stress	30 V	MBR10100 - 100 V
Rectifier diode maximum current stress	5.97 A	MBR10100 - 10 A
Rectifier diode forward voltage	V_{F3}	MBR10100 - 0.65 V
Rectifier diode forward resistance	R_{F3}	MBR10100 - 20 mΩ
Clamping diode maximum voltage stress	60 V	MBR10100 - 100 V
Clamping diode maximum current stress	1.99 A	MBR10100 - 10 A
Clamping diode forward voltage	V_{F3}	MBR10100 - 0.65 V
Clamping diode forward resistance	R_{F3}	MBR10100 - 20 mΩ
Flyback transformer core	-	Magnetics Pot Core
Transformer core number	-	0P-43622
Primary winding magnetizing inductance	650 μH	641 μH
Secondary winding magnetizing inductance	75.2 μH	71.2 μH
Number of primary winding turns	36	36
Number of secondary winding turns	12.24	12
Primary-to-secondary turns ratio	2.94	3
Primary winding leakage inductance	L_{lp}	14.4 μH
Secondary winding leakage inductance	L_{lS}	2.98 μH
Total leakage inductance (primary)	L_l	14.73 μH
Primary winding resistance	r_{T1}	98 mΩ
Secondary winding resistance	r_{T2}	29.9 mΩ
Magnetizing inductance ESR	r_L	170 mΩ
Length of air gap	0.5 mm	0.5 mm

in Table 2.1. The circuits of the single-switch flyback converters with and without a
resistor-capacitor-diode (RCD) snubber are shown in Figs. 2.4 and 2.5, respectively.
The design specifications of the single-switch flyback converter for CCM is given in
Table 2.2. Saber models of power MOSFETs IRF510 and power diodes MBR10100
were used for simulation. The predicted theoretical waveforms of Fig. 2.3 were in
excellent agreement with the simulation waveforms shown in Fig. 2.6.

Table 2.2: LIST OF COMPONENTS AND THEIR SPECIFICATIONS FOR SINGLE-SWITCH FLYBACK CONVERTER FOR CCM

Parameter	Value	Component
Power MOSFET maximum voltage stress	348 V	IRF840 - 500 V
Power MOSFET maximum current stress	1.99 A	IRF840 - 8 A
Power MOSFET drain-to-source on-resistance	r_{DS}	IRF840 - 0.85 Ω
Power MOSFET drain-to-source capacitance	C_O	IRF840 - 120 pF
Rectifier diode maximum voltage stress	30 V	MBR10100 - 100 V
Rectifier diode maximum current stress	5.97 A	MBR10100 - 10 A
Rectifier diode forward voltage	V_{F3}	MBR10100 - 0.65 V
Rectifier diode forward resistance	R_{F3}	MBR10100 - 20 mΩ
Flyback transformer core	-	Magnetics Pot Core
Transformer core number	-	0P-43622
Primary winding magnetizing inductance	650 μH	641 μH
Secondary winding magnetizing inductance	75.2 μH	71.2 μH
Number of primary winding turns	36	36
Number of secondary winding turns	12.24	12
Primary-to-secondary turns ratio	2.94	3
Primary winding leakage inductance	L_{lp}	14.4 μH
Secondary winding leakage inductance	L_{lS}	2.98 μH
Total leakage inductance (primary)	L_l	14.73 μH
Primary winding resistance	r_{T1}	98 mΩ
Secondary winding resistance	r_{T2}	29.9 mΩ
Magnetizing inductance ESR	r_L	170 mΩ
Length of air gap	0.5 mm	0.5 mm

The theoretical voltage and current waveforms of the two-switch flyback converter shown in Fig. 2.3 are experimentally verified. The experimental voltage and current waveforms of the two-switch flyback converter at full load and maximum and minimum input voltages of 60 V and 40 V are presented in Figs. 2.7 - 2.10. The maximum voltage across the power MOSFET switches is clamped at 60 V for $V_I = 60$ V and at 40 V for $V_I = 40$ V as shown in Figs. 2.7 and 2.9, respectively. The switch currents are shown in Figs. 2.7 and 2.9, and the clamping diode currents along with the output rectifier diode current are shown in Figs. 2.8 and 2.10 for V_I equal to 60 V and 40 V, respectively. The clamping diodes D_1 and D_2 turn off at zero current. Figs. 2.11 - 2.14 show the experimental and theoretical, current and voltage waveforms of the switch
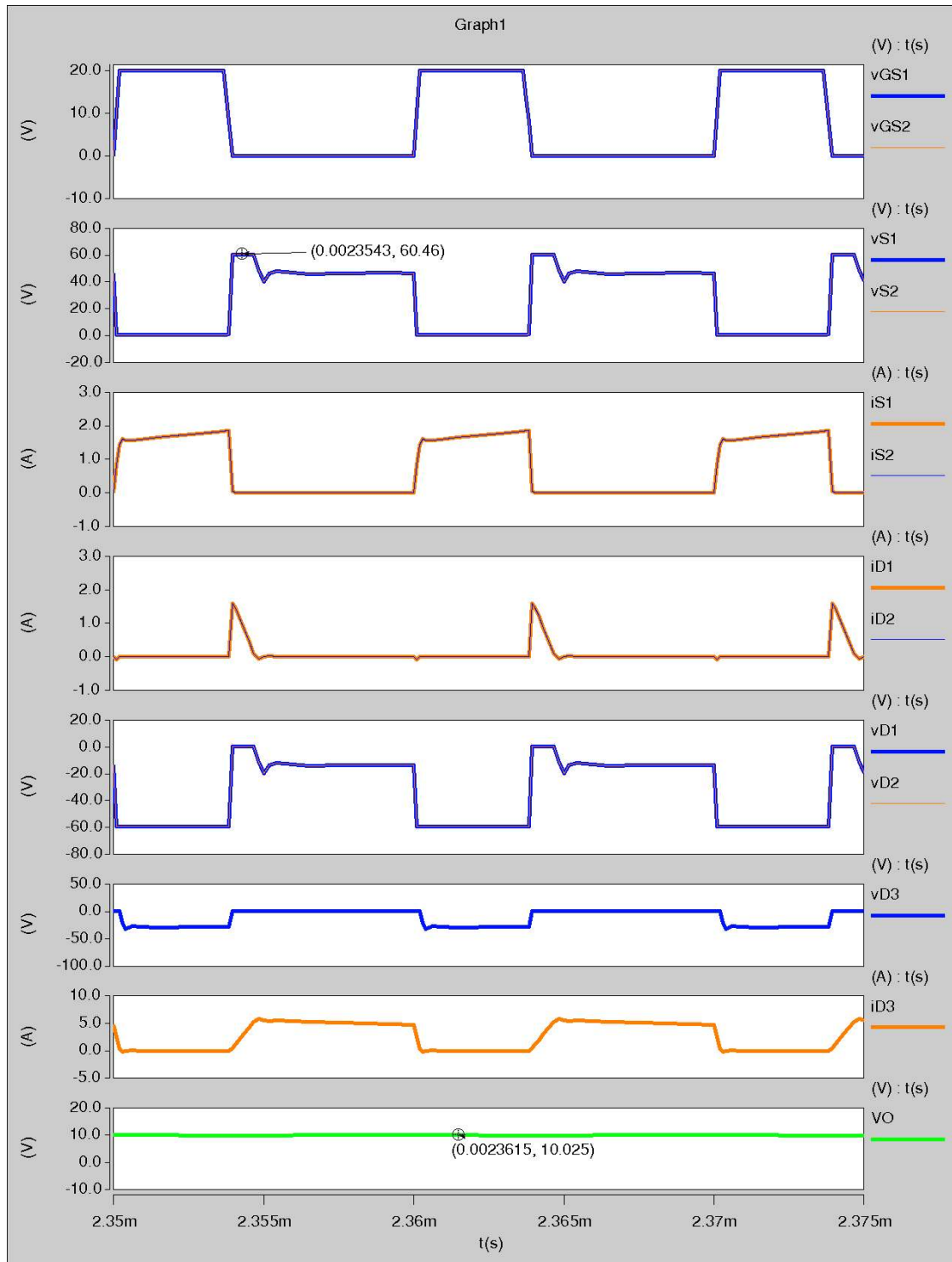
Figure 2.6: Simulation results. Voltage and current waveforms of the hard-switching two-switch flyback PWM DC-DC converter for CCM.
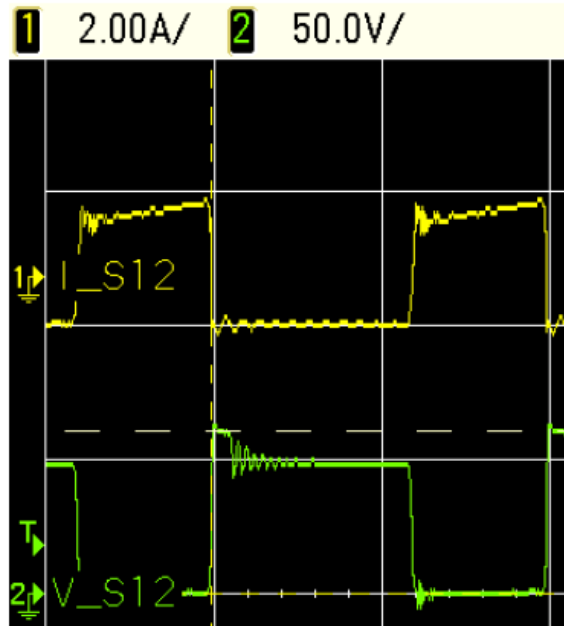
Figure 2.7: Experimental results of the two-switch switch flyback converter at $V_I = 60$ V and $P_O = 30$ W. Top trace: switch current waveforms i_{S1}, i_{S2} (2 A/div.); Bottom trace: switch drain-to-source voltage waveforms v_{DS1}, v_{DS2} (50 V/div.). Horizontal scale: 5 μs/div.

Figure 2.8: Experimental results of the two-switch flyback converter at $V_I = 60$ V and $P_O = 30$ W. Top trace: clamping diode current waveforms i_{D1}, i_{D2} (2 A/div.); Bottom trace: rectifier diode current waveform i_{D3} (10 A/div.). Horizontal scale: 5 μs/div.
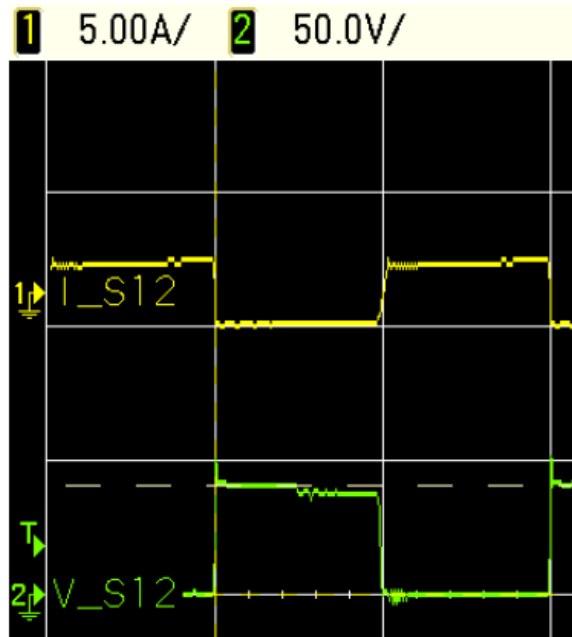
Figure 2.9: Experimental results of the two-switch flyback converter at $V_I = 40$ V and $P_O = 30$ W. Top trace: switch current waveforms i_{S1}, i_{S2} (5 A/div.); Bottom trace: switch drain-to-source voltage waveforms v_{DS1}, v_{DS2} (50 V/div.). Horizontal scale: 5 μs/div.
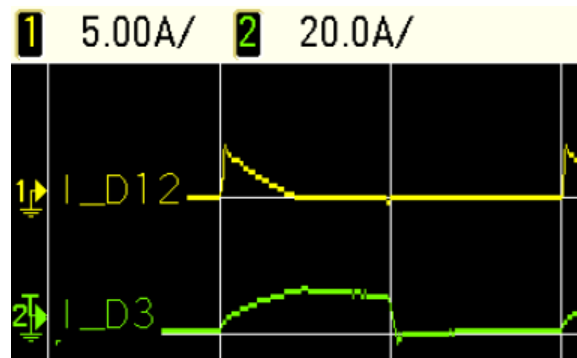
Figure 2.10: Experimental results of the two-switch flyback converter at $V_I = 40$ V and $P_O = 30$ W. Top trace: clamping diode current waveforms i_{D1}, i_{D2} (5 A/div.); Bottom trace: rectifier diode current waveform i_{D3} (20 A/div.). Horizontal scale: 5 μs/div.

in the single-switch flyback converter without and with an RCD clamp circuit. From the experimental voltage waveform of the switch shown in Fig. 2.11, it can be seen that the voltage stress of the switch is unpredictable due to the resonance caused by the transformer leakage inductance and the switch output capacitance. The voltage
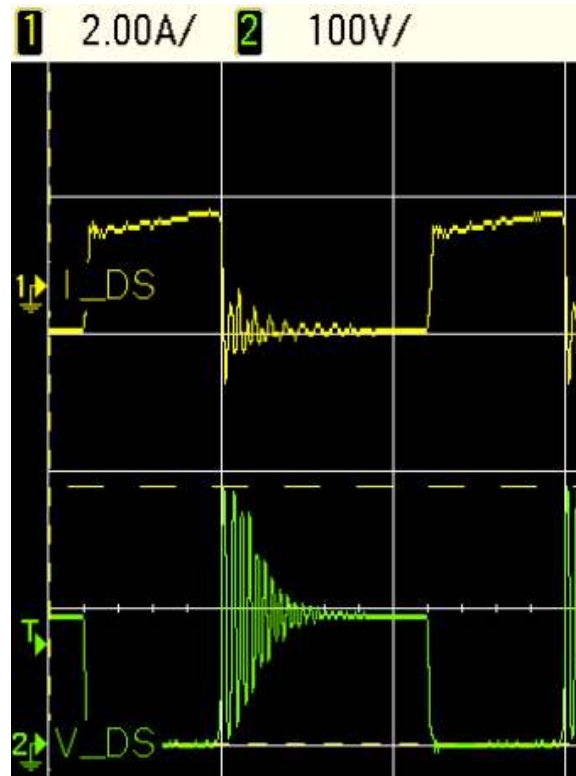
Figure 2.11: Experimental results of the single-switch flyback converter without an RCD clamp at $V_I = 60$ V and $P_O = 30$ W. Top trace: switch current waveforms i_{DS} (2 A/div.); Bottom trace: switch drain-to-source voltage waveforms v_{DS} (100 V/div.). Horizontal scale: 5 μs/div.
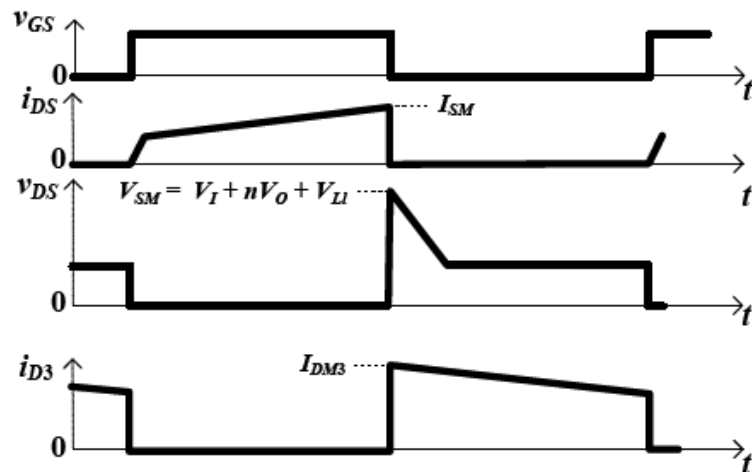
Figure 2.12: Key theoretical waveforms of the single-switch flyback converter without an RCD clamp for CCM.
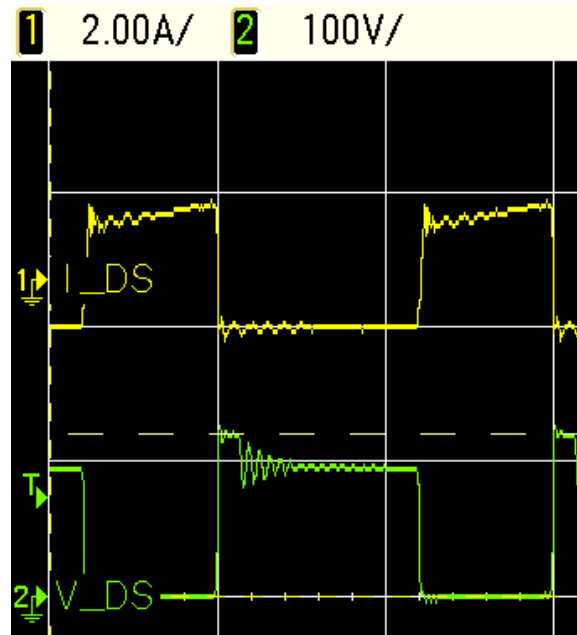
Figure 2.13: Experimental results of the single-switch flyback converter with an RCD clamp at $V_I = 60$ V and $P_O = 30$ W. Top trace: switch current waveforms i_{DS} (2 A/div.); Bottom trace: switch drain-to-source voltage waveforms v_{DS} (100 V/div.). Horizontal scale: 5 μs/div.
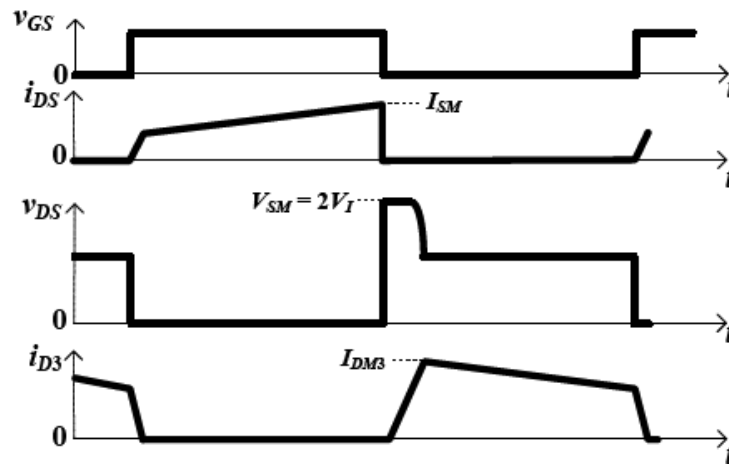
Figure 2.14: Key theoretical waveforms of the single-switch switch flyback converter with an RCD clamp for CCM.

across the switch in the single-switch flyback converter with an RCD passive clamp is clamped to $2V_I = 120$ V as shown in Fig. 2.13 and is in excellent agreement with the theoretical waveforms shown in Fig. 2.14. However, the additional loss in the

Table 2.3: COMPARISON OF POWER LOSSES OF THE TWO-SWITCH AND THE SINGLE-SWITCH FLYBACK CONVERTERS FOR CCM

Parameter	$P_O = 30$ W Loss (W)	$P_O = 10$ W Loss (W)
Two-Switch Flyback Converter		
MOSFET conduction loss $2P_{rDS}$	1.6066	0.1758
MOSFET switching loss $2P_{SW}$	0.0216	0.0216
Rectifier diode loss P_{D3}	2.27	0.6864
Clamping diode loss $2P_{D1D2}$	0.8975	0.1522
Primary winding resistance loss P_{rT1}	0.1458	0.0162
Secondary winding resistance loss P_{rT2}	0.4894	0.0538
Magnetizing inductance ESR loss P_{rL}	0.562	0.0624
Total power loss P_{LS}	5.99	1.168
Converter efficiency η	83.35%	89.95%
Single-Switch Flyback Converter		
MOSFET conduction loss P_{rDS}	1.264	0.1405
MOSFET switching loss P_{SW}	3.63	0.751
Rectifier diode loss P_{D3}	2.27	0.6864
Clamping diode loss	-	-
Primary winding resistance loss P_{rT1}	0.1458	0.0313
Secondary winding resistance loss P_{rT2}	0.4894	0.0538
Magnetizing inductance ESR loss P_{rL}	0.562	0.0624
Total power loss P_{LS}	8.36	1.725
Converter efficiency η	78.2%	85.28%
Single-Switch Flyback Converter with an RCD Clamp		
MOSFET conduction loss P_{rDS}	1.264	0.1405
MOSFET switching loss P_{SW}	0.1107	0.0625
Rectifier diode loss P_{D3}	2.27	0.6864
Clamping diode loss	-	-
Primary winding resistance loss P_{rT1}	0.1458	0.0313
Secondary winding resistance loss P_{rT2}	0.4894	0.0538
Magnetizing inductance ESR loss P_{rL}	0.562	0.0624
RCD clamp circuit loss P_{RCD}	4.707	1.451
Total power loss P_{LS}	9.54	2.487
Converter efficiency η	75.87%	80.08%

clamping circuit reduces the efficiency of the single-switch flyback converter with an RCD clamp. The flyback transformer parameters listed in Tables 2.1 and 2.2 are measured using Hewlett Packard 4275A Multi-Frequency LCR meter. Table 2.3 gives the comparison of losses of the two-switch and the single-switch flyback converters
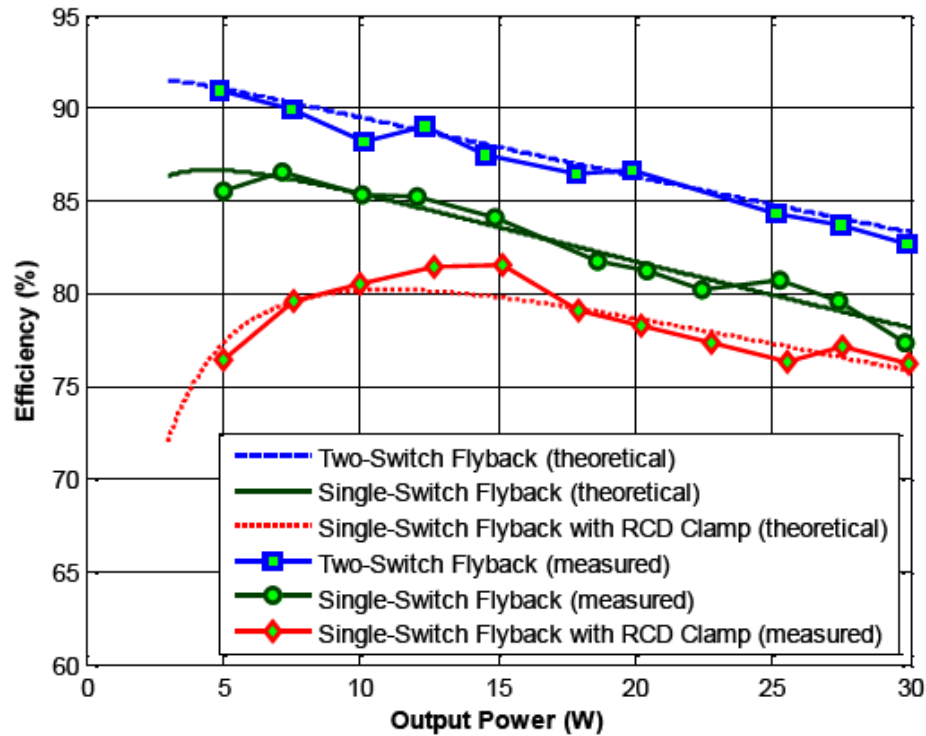
Figure 2.15: Theoretical and experimental efficiencies of the two-switch and the single-switch flyback converters plotted as a function of converter output power for CCM operation.

for full load and light load conditions. From Table 2.2, it is clearly seen that the maximum voltage stress of the power MOSFET in the single-switch flyback converter is predicted to be 348 V. A MOSFET with higher voltage rating (IRF840, 500 V, 0.85 Ω), is used in the single-switch flyback converter as against a MOSFET with lower voltage rating (IRF510, 100 V, 0.54 Ω), which is safely used in the two-switch topology.

Fig. 2.15 compares the efficiencies of the two-switch flyback converter and the single-switch flyback converter (with and without an RCD clamp) versus output power. A plot of theoretical efficiency predicted using the equations (2.40) - (2.52) is shown in Fig. 2.15 and is fairly in good agreement with the measured efficiency of the two-switch flyback converter circuit. The total on-resistance of two power MOSFETs

used in the two-switch topology is slightly larger than that of the on-resistance of the single MOSFET used in the single-switch version, due to which the conduction losses in the two-switch flyback converter is only about 1.25 times than that of the single-switch flyback converter. From Table 2.3, it can be clearly seen that the overall losses in the two-switch flyback converter is lesser than that of the single-switch flyback converter largely due to the reduced switching losses in the two-switch flyback converter.

2.7 Steady-State Analysis of Two-Switch Flyback Converter for DCM

2.7.1 Assumptions

The steady-state analysis of the two-switch flyback PWM converter of Fig. 2.1 is based on the following assumptions:

1. The power MOSFETs are ideal switches except for their output capacitances.

2. The diodes are ideal switches.

3. The diode capacitances and lead inductances are zero.

4. Passive components are linear, time-invariant, and frequency-independent.

5. The converter is operating in steady-state.

6. The switching period $T_s = 1/f_s$ is much smaller than the time constants of reactive components.

2.7.2 Principle of Circuit Operation for DCM

The principle of operation of each stage is explained with the aid of equivalent circuits shown in Fig. 2.16 and the voltage and current waveforms of the converter shown in Fig. 2.17.
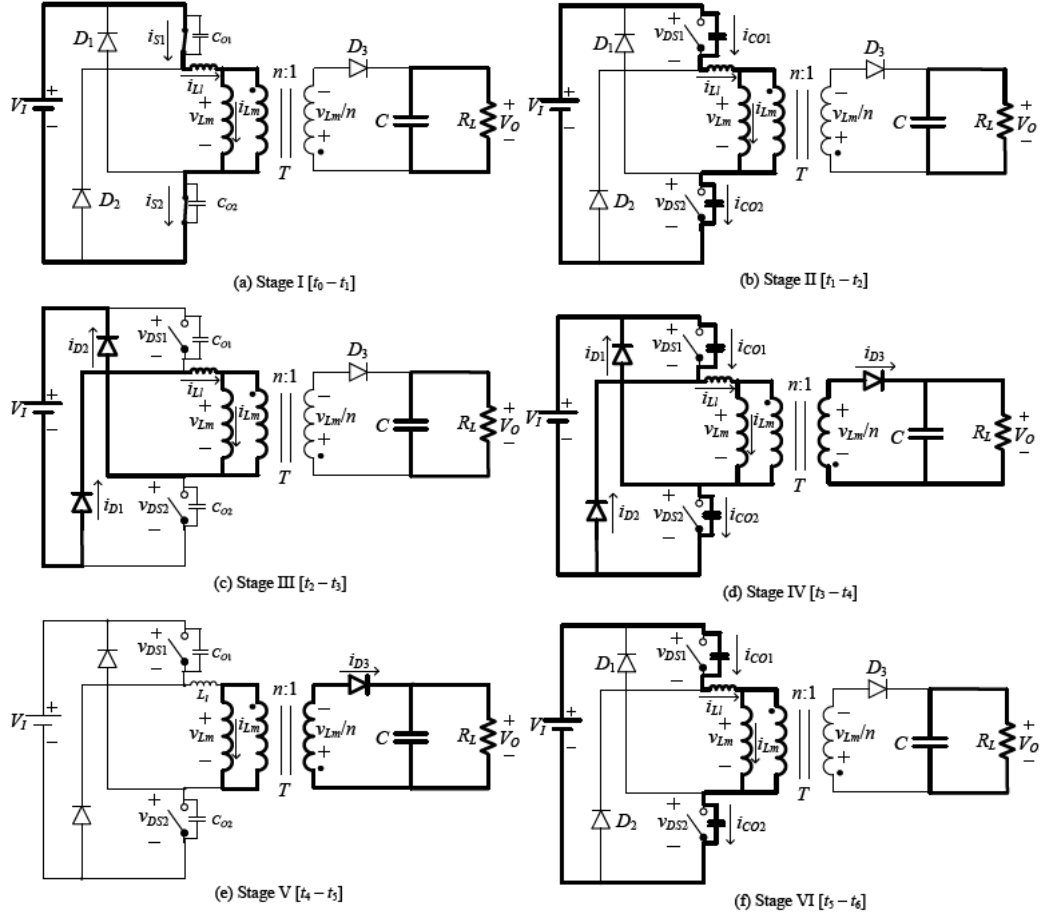
Figure 2.16: Equivalent circuits of the two-switch flyback converter for DCM at different stages of a switching cycle. (a) Stage I ($t_0 < t \le t_1$). (b) Stage II ($t_1 < t \le t_2$). (c) Stage III ($t_2 < t \le t_3$). (d) Stage IV ($t_3 < t \le t_4$). (e) Stage V ($t_4 < t \le t_5$). (f) Stage VI ($t_5 < t \le t_6$).

Stage 1 ($t_0 < t \le t_1$): At time $t = t_0$, both the switches S_1 and S_2 are turned on by a gate driver. An equivalent circuit for this stage is shown in Fig. 2.16(a). Since the clamping diode voltages $v_{D1} = v_{D2} = -V_I$, the diodes D_1 and D_2 are reverse biased and hence their currents i_{D1} and i_{D2} are zero. Assuming $L_l << L_m$, the voltage across the magnetizing inductance is approximately V_I, from which the voltage across the rectifier diode is

$$v_{D3} \approx -\left(\frac{V_I}{n} + V_O\right). \qquad (2.53)$$
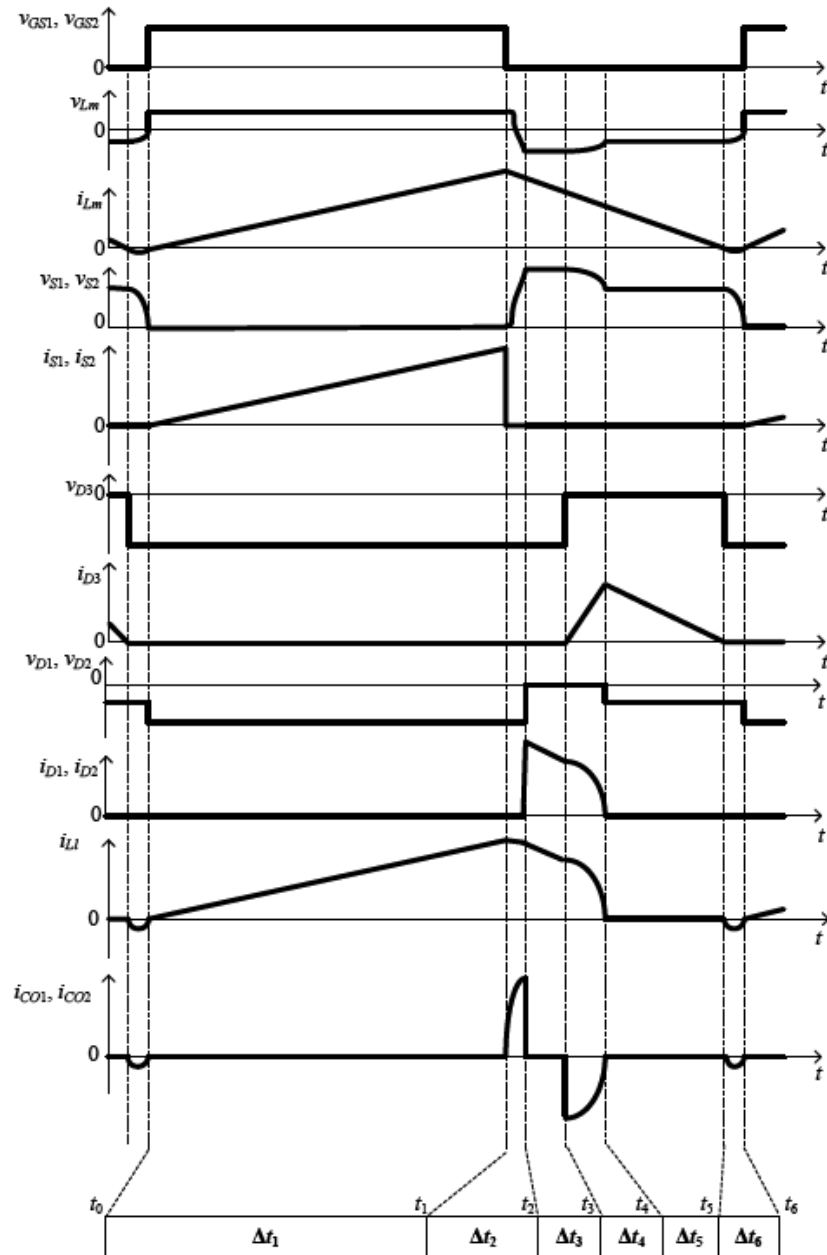
Figure 2.17: Voltage and current waveforms of the two-switch flyback PWM DC-DC converter for DCM.

From (2.53), it follows that the diode D_3 is reverse-biased and hence the rectifier diode current i_{D3} is zero. The switches S_1 and S_2 turn on softly as the leakage inductance L_l limits the rate of rise of current. The current through the switches,

leakage inductance, and the magnetizing inductance is

$$i_{S1} = i_{S2} = i_{Ll} = i_{Lm} = \frac{V_I}{L_m + L_l}(t - t_0) + i_{Lm}(t_0), \tag{2.54}$$

where $i_{Lm}(t_0) = 0$. The peak current of the magnetizing inductance is

$$i_{Lm}(t_1) = \frac{V_I D T}{L_m + L_l} = \frac{V_I D}{f_s(L_m + L_l)} \tag{2.55}$$

The current through the magnetizing inductance, leakage inductance, and the switches rises linearly with a slope of $V_I/(L_m + L_l)$. The peak-to-peak value of the ripple current through the magnetizing inductance is $\Delta i_{Lm} = i_{Lm}(t_1)$. The voltages across the switches v_{S1} and v_{S2} are zero. This stage ends at time $t = t_1$, when both the switches are turned off by the gate driver.

Stage 2 ($t_1 < t \le t_2$): During this stage, the switches S_1, S_2 and all the diodes D_1, D_2, D_3 are OFF. An equivalent circuit for this stage is shown in Fig. 2.16(b). The magnetizing current (equal to the leakage current) charges the switch output capacitors C_{O1} and C_{O2} in a resonant manner. The current through C_{O1}, C_{O2}, the leakage inductance, and the magnetizing inductance is

$$i_{CO1} = i_{CO2} = i_{Ll} = i_{Lm} = \frac{V_I}{Z_1}\sin\omega_1(t - t_1) + \Delta i_{Lm}\cos\omega_1(t - t_1), \tag{2.56}$$

where

$$Z_1 = \sqrt{\frac{(L_m + L_l)(C_{O1} + C_{O2})}{C_{O1}C_{O2}}} \tag{2.57}$$

and

$$\omega_1 = \sqrt{\frac{C_{O1} + C_{O2}}{C_{O1}C_{O2}(L_m + L_l)}}. \tag{2.58}$$

Assuming $C_{O1} = C_{O2} = C_O$, the switch voltages are

$$v_{S1} = v_{S2} = v_{CO1} = v_{CO2} = \frac{\Delta i_{Lm}Z_1}{2}\sin\omega_1(t - t_1) - \frac{V_I}{2}\cos\omega_1(t - t_1). \tag{2.59}$$

This stage ends at time $t = t_2$, when the voltage across each switch equals V_I, thus turning on the clamping diodes D_1 and D_2.

Stage 3 ($t_2 < t \le t_3$): During this stage, the switches S_1, S_2 are OFF, the diodes D_1, D_2, are ON, and D_3 is OFF. An equivalent circuit for this stage is depicted in Fig. 2.16(c). The voltage across each switch is clamped to $V_I + V_F$, where V_F is the forward voltage of the clamping diode. The current through the magnetizing and leakage inductances charges the input voltage source V_I via clamping diodes D_1 and D_2 given by

$$i_{Ll} = i_{Lm} = -\frac{V_I}{L_m + L_l}(t - t_2) - i_{Lm}(t_2), \tag{2.60}$$

where $i_{Lm}(t_2)$ is the initial current of the magnetizing inductance at time t_2. This mode is referred to as regenerative clamping mode. This stage ends at time $t = t_3$, when the voltage across the magnetizing inductance equals $-nV_O$ thereby forward biasing the rectifier diode D_3.

Stage 4 ($t_3 < t \le t_4$): During this stage, the switches S_1, S_2 are OFF and all the diodes D_1, D_2, D_3 are ON. An equivalent circuit for this stage is depicted in Fig. 2.16(d). The primary winding is clamped to the reflected output voltage of $-nV_O$. The resonant current through the leakage inductance L_l and the switch output capacitances C_{O1} and C_{O2} is

$$i_{Ll} = i_{CO1} = i_{CO2} = i_{Ll}(t_3) \cos \omega_2(t - t_3), \tag{2.61}$$

where $i_{Ll}(t_3)$ is the initial current of the leakage inductance at time instant t_3. The voltage across the leakage inductance is

$$v_{Ll} = -i_{Ll}(t_3)Z_2 \sin \omega_2(t - t_3), \tag{2.62}$$

where

$$Z_2 = \sqrt{\frac{L_l(C_{O1} + C_{O2})}{C_{O1}C_{O2}}} \tag{2.63}$$

and

$$\omega_2 = \sqrt{\frac{C_{O1} + C_{O2}}{L_l C_{O1} C_{O2}}}. \tag{2.64}$$

The voltages across the switches are

$$v_{S1} = v_{S2} = v_{CO1} = v_{CO2} = V_I - i_{Ll}(t_3)Z_2 \sin \omega_2(t - t_3).$$ (2.65)

This stage ends at time $t = t_4$, when the leakage inductance current i_{Ll} drops to zero and the rectifier diode current i_{D3} equals the reflected magnetizing inductance current ni_{Lm}, thereby turning off the clamping diodes D_1 and D_2.

Stage 5 $(t_4 < t \leq t_5)$: During this stage, the switches S_1, S_2, the clamping diodes D_1, D_2 are OFF, and the rectifier diode D_3 is ON. An equivalent circuit for this stage is depicted in Fig. 2.16(e). The voltage across the magnetizing inductance is $-nV_O$. The current through the magnetizing inductance is

$$i_{Lm} = -\frac{nV_O}{L_m}(t - t_4) + i_{Lm}(t_4),$$ (2.66)

where $i_{Lm}(t_4)$ is the initial current of the magnetizing inductance at $t = t_4$. The rectifier diode current is

$$i_{D3} = -\frac{n^2 V_O}{L_m}(t - t_4) + ni_{Lm}(t_4).$$ (2.67)

Assuming that the switches S_1 and S_2 are identical, the voltages across the switches are

$$v_{S1} = v_{S2} = \frac{V_I + nV_O}{2}.$$ (2.68)

Assuming that the clamping diodes D_1 and D_2 are identical, the voltages across the clamping diodes are

$$v_{D1} = v_{D2} = \frac{nV_O - V_I}{2}.$$ (2.69)

The current through the switches i_{S1}, i_{S2}, the current through the clamping diodes i_{D1}, i_{D2}, and the leakage inductance current i_{Ll} are zero. This stage ends at time $t = t_5$, when the rectifier diode current i_{D3} reaches zero.

Stage 6 $(t_5 < t \leq t_6)$: During this stage, the switches S_1 and S_2 are OFF and all the diodes D_1, D_2 and D_3 are OFF. An equivalent circuit for this stage is shown in

Fig. 2.16(f). The resonant current through the magnetizing and leakage inductances discharge the switch output capacitances C_{O1} and C_{O2}. The resonant current through C_{O1}, C_{O2}, the leakage inductance, and the magnetizing inductance is

$$i_{CO1} = i_{CO2} = i_{Ll} = i_{Lm} = -\frac{nV_O}{2Z_3} \sin \omega_3(t - t_5), \tag{2.70}$$

where

$$Z_3 = \sqrt{\frac{(L_m + L_l)(C_{O1} + C_{O2})}{C_{O1}C_{O2}}} \tag{2.71}$$

and

$$\omega_3 = \sqrt{\frac{C_{O1} + C_{O2}}{C_{O1}C_{O2}(L_m + L_l)}}. \tag{2.72}$$

Assuming $C_{O1} = C_{O2} = C_O$, the switch voltages are

$$v_{S1} = v_{S2} = v_{CO1} = v_{CO2} = \frac{V_I}{2} + \frac{nV_O}{2} \cos \omega_3(t - t_5). \tag{2.73}$$

From (2.73), it can be seen that the voltages across the switches can reach a minimum of $(V_I - nV_O)/2$ at $t = t_6$, where

$$t_6 = t_5 + \frac{\pi}{\omega_3}. \tag{2.74}$$

The switch capacitive turn-on loss is given as

$$P_{SWon} = \frac{1}{2}f_s C_O V_{CO}^2, \tag{2.75}$$

where $V_{CO} = v_{CO1}(t_6) = v_{CO2}(t_6)$. The range of V_{CO} is

$$\frac{V_I - nV_O}{2} \leq V_{CO} \leq \frac{V_I + nV_O}{2}. \tag{2.76}$$

In Fig. 2.17, the time duration of *Stages* 2 and 6 are exaggerated for better understanding of the converter operation.

2.8 Design of Two-Switch Flyback Converter for DCM

2.8.1 DC Voltage Transfer Function

Referring to the voltage waveform of the magnetizing inductance in Fig. 2.17 and applying volt-second balance, we have

$$V_I \Delta t_1 = V_I(\Delta t_2 + \Delta t_3 + \Delta t_4) + nV_O(\Delta t_5 + \Delta t_6), \tag{2.77}$$

from which the DC voltage transfer function of the converter is

$$M_{VDC} \equiv \frac{V_O}{V_I} = \frac{\Delta t_1 - (\Delta t_2 + \Delta t_3 + \Delta t_4)}{n(\Delta t_5 + \Delta t_6)}. \tag{2.78}$$

Assuming that the time duration of *Stages* 2, 3, 4, and 6 are very small in comparison with those of *Stages* 1 and 5, M_{VDC} can be approximated to

$$M_{VDC} \equiv \frac{V_O}{V_I} \approx \frac{\Delta t_1}{n\Delta t_5} = \frac{D}{nD_1}, \tag{2.79}$$

where D_1 is the ratio of $(\Delta t_2 + \Delta t_3 + \Delta t_4 + \Delta t_5)/T \approx \Delta t_5/T$. In order to find D_1, consider the DC output current I_O given by

$$I_O = \frac{1}{T}\int_0^T i_{D3}\ dt = \frac{1}{T}\int_{DT}^{(D+D_1)T} i_{D3}\ dt = \frac{nD_1\Delta i_{Lm}}{2} = \frac{nDD_1V_I}{2f_s(L_m + L_l)} = \frac{V_O}{R_L}, \tag{2.80}$$

resulting in

$$M_{VDC} = \frac{V_O}{V_I} = \frac{nDD_1R_L}{2f_s(L_m + L_l)}. \tag{2.81}$$

Equating the right hand sides of (2.79) and (2.81), we have

$$D_1 = \sqrt{\frac{2f_s(L_m + L_l)I_O}{n^2V_O}}. \tag{2.82}$$

Substituting (2.82) into (2.79) yields

$$M_{VDC} \approx D\sqrt{\frac{R_L}{2f_s(L_m + L_l)}}. \tag{2.83}$$

2.8.2 Device Stresses

The selection of components is based on the maximum values of the voltage and current stresses of the switches and the diodes. During the third stage, the maximum off-state voltage appearing across S_1 and S_2 is

$$V_{SM1(\text{max})} = V_{SM2(\text{max})} = V_{I(\text{max})}. \tag{2.84}$$

During the fifth stage, the maximum off-state voltage appearing across S_1 and S_2 is

$$V_{SM1(\text{max})} = V_{SM2(\text{max})} = \frac{V_{I(\text{max})} + nV_O}{2} \tag{2.85}$$

During the first stage, the maximum value of the current through the switches is

$$I_{SM1(\text{max})} = I_{SM2(\text{max})} = \Delta i_{Lm} = \frac{DV_I}{f_s(L_m + L_l)} = \frac{DV_O}{f_s(L_m + L_l)M_{VDC}} = \sqrt{\frac{2P_{O(\text{max})}}{f_s(L_m + L_l)}}, \tag{2.86}$$

where $P_{O(max)}$ is the maximum DC output power. During the first stage, the maximum value of the diode reverse voltage is

$$V_{DM3(\text{max})} = \frac{V_I}{n} + V_O. \tag{2.87}$$

At the end of the fourth stage, the maximum value of the current through the rectifier diode is approximately

$$I_{DM3(\text{max})} \approx n\Delta i_{Lm} = \sqrt{\frac{2P_{O(\text{max})}}{f_s(L_m + L_l)}}. \tag{2.88}$$

During the first and the second stage, the maximum values of the clamping diode reverse voltage are

$$V_{DM1(\text{max})} = V_{DM2(\text{max})} = V_{I(\text{max})}. \tag{2.89}$$

During the third stage, the maximum values of the current through the clamping diodes are

$$I_{DM1(\text{max})} = I_{DM2(\text{max})} = \Delta i_{Lm} = \sqrt{\frac{2P_{O(\text{max})}}{f_s(L_m + L_l)}}. \tag{2.90}$$
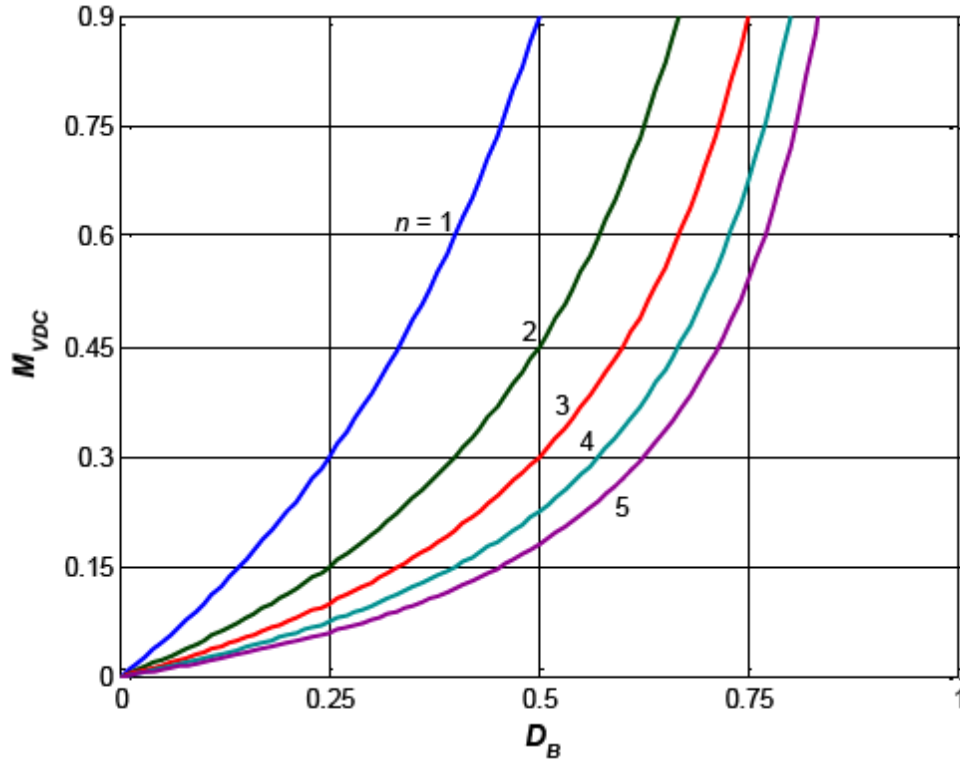
Figure 2.18: Plot of DC voltage transfer function of the two-switch flyback converter at the boundary between CCM and DCM versus duty ratio D_B for different values of transformer primary-to-secondary turns ratio n for $\eta = 0.9$.

2.8.3 Design Procedure for DCM

The DC voltage transfer function of the two-switch flyback converter at the boundary between CCM and DCM is given by

$$M_{VDC} = \frac{V_O}{V_I} = \frac{\eta D_B}{n(1 - D_B)}, \tag{2.91}$$

from which, the transformer turns ratio is given by

$$n = \frac{\eta D_{B\max}}{M_{VDC}(1 - D_{B\max})}, \tag{2.92}$$

where D_B is the duty cycle at the boundary between CCM and DCM and $M_{VDC(\max)} = V_O/V_{I(\min)}$. In (2.92), the maximum value of the duty cycle $D_{B\max}$ is taken as 0.5. Fig. 2.18 shows a plot of DC voltage transfer function M_{VDC} versus duty ratio D_B for

various values of transformer turns ratio n. In (2.91), M_{VDC} is calculated considering the desired converter efficiency η to be 90%. The peak voltage and current stresses of the devices on either side of the flyback transformer are influenced by n. In DCM operation at the boundary, the current and voltage stresses are minimal when n is such that D is 0.5. Hence, the value of n is calculated at $D_{B\max} = 0.5$. From Fig. 2.18, it can be seen that $n \approx 2.6$ for $M_{VDC} = 0.33$, $D_B = 0.5$, and $\eta = 0.9$.

Since the current waveforms of the switches in the two-switch flyback converter are similar to the switch current of the single-switch flyback converter, the usual method to determine the value of the magnetizing inductance for DCM operation can be used. The maximum value of the magnetizing inductance for DCM operation is given by

$$L_{m(\max)} = \frac{n^2 V_O (1 - D_{B\max})^2}{2 f_s I_{O\max}}. \tag{2.93}$$

Using (2.84) - (2.90), the power MOSFETs and the diodes are selected. Selection of the output filter capacitor is based on the output voltage ripple specification.

$$C = \frac{D_{\max} V_O}{f_s R_{L\min} V_{cpp}}, \tag{2.94}$$

where V_{cpp} is the peak-to-peak value of the ac component of the voltage across the capacitance, which is approximately

$$V_{cpp} \approx V_r - V_{rcpp}. \tag{2.95}$$

In (2.95), V_r is the peak-to-peak value of the output ripple voltage (usually expressed as a percentage of DC output voltage V_O) and $V_{rcpp} = r_C I_{Cpp}$ is the peak-to-peak value of the voltage across the equivalent series resistance (ESR) r_C of the capacitor. The designed capacitor must be able to withstand the rms capacitor current given by

$$I_{Crms} \approx I_{D3rms} - I_O = n\Delta i_{Lm} \sqrt{\frac{D_1}{3}} - I_O. \tag{2.96}$$

The peak-to-peak value of the capacitor current is

$$I_{Cpp} \approx I_{D3} = n\Delta i_{Lm} = \frac{n V_O D_1}{f_s (L_m + L_l)}. \tag{2.97}$$

2.9 Power Loss and Efficiency of Two-Switch Flyback Converter for DCM

Equations for the power losses in the two-switch flyback converter for DCM are obtained by assuming that the time duration of *Stages* 2, 4, and 6 are very small. Using (2.54) and (2.86), the rms value of the current through the switches is

$$I_{S1,S2(\text{rms})} = \sqrt{\frac{1}{T_s} \int_{t_0}^{t_1} i_{S1,S2} \, dt} = \Delta i_{Lm}\sqrt{\frac{D}{3}}. \tag{2.98}$$

Assuming that the on-resistances of the switches $r_{DS1} = r_{DS2} = r_{DS}$, the total conduction loss in $2r_{DS}$ and primary winding resistance r_{T1} is

$$P_{ST1} = (2r_{DS} + r_{T1})I_{S1,S2(\text{rms})}^2 = \frac{(2r_{DS} + r_{T1})D}{3}\Delta i_{Lm}^2. \tag{2.99}$$

Assuming that the output capacitances of the switches $C_{O1} = C_{O2} = C_O$ and using (2.84), the switch capacitive turn-off loss is given by

$$P_{SWoff} = \frac{1}{2}f_s(2C_O)V_{SM}^2 = f_s C_O V_I^2. \tag{2.100}$$

The switch capacitive turn-on loss is given in (2.75). Using (2.67) and (2.88), the rms value of the current through the rectifier diode is

$$I_{D3(\text{rms})} = \sqrt{\frac{1}{T_s} \int_{t_3}^{t_5} i_{D3} \, dt} = n\Delta i_{Lm}\sqrt{\frac{D_1}{3}}. \tag{2.101}$$

The total conduction loss in the rectifier diode forward resistance R_{F3} and the secondary winding resistance r_{T2} is

$$P_{DT2} = (R_{F3} + r_{T2})I_{D3(\text{rms})}^2 = \frac{(R_{F3} + r_{T2})D_1 n^2}{3}\Delta i_{Lm}^2. \tag{2.102}$$

The average value of the rectifier diode current $I_{D3} = I_O$, from which, the rectifier diode loss associated with the forward voltage of the rectifier diode V_{F3} is

$$P_{VF3} = V_{F3}I_{D3} = V_{F3}I_O. \tag{2.103}$$

Using (2.60) and (2.90), the rms value of the current through the clamping diodes is

$$I_{D1,D2(\text{rms})} = \sqrt{\frac{1}{T_s} \int_{t_2}^{t_3} i_{D1,D2} \, dt} = \Delta i_{Lm} \sqrt{\frac{\Delta t_3}{T_s}}. \tag{2.104}$$

Assuming that the forward resistances of the clamping diodes $R_{F1} = R_{F2} = R_F$ and $\Delta t_3 = 10\% T_s$, the total conduction loss in $2R_F$ is

$$P_{RF} = 2R_F I_{D1,D2(\text{rms})}^2 \approx 0.2 R_F \Delta i_{Lm}^2. \tag{2.105}$$

The average value of the clamping diode current is

$$I_{D1} = I_{D2} = I_D = \frac{1}{T_s} \int_{t_2}^{t_3} i_D \, dt = \frac{I_O}{n(1-D)} \left(\frac{\Delta t_3}{T_s} \right). \tag{2.106}$$

Assuming that the forward voltage of the clamping diodes $V_{F1} = V_{F2} = V_F$ and $\Delta t_3 = 10\% T_s$, the total loss associated with the forward voltages of two clamping diodes together is

$$P_{VF} = 2V_F I_D = \frac{2V_F I_O}{n(1-D)} \left(\frac{\Delta t_3}{T_s} \right) \approx \frac{0.2 V_F I_O}{n(1-D)}. \tag{2.107}$$

Using (2.54), (2.66), and (2.86), the rms value of the current through the magnetizing inductance is approximately

$$I_{L(\text{rms})} = \sqrt{\frac{1}{T_s} \int_{t_0}^{t_5} i_{Lm} \, dt} = \Delta i_{Lm} \sqrt{\frac{D+D_1}{3}}. \tag{2.108}$$

The power loss in the equivalent series resistance (ESR) r_L of the magnetizing inductance is

$$P_{rL} = r_L I_{Lm(\text{rms})}^2 = \frac{r_L (D+D_1)}{3} \Delta i_{Lm}^2. \tag{2.109}$$

The total power loss in the two-switch flyback converter for DCM is

$$P_{LS} = P_{ST1} + P_{SWon} + P_{SWoff} + P_{DT2} + P_{VF3} + P_{RF} + P_{VF} + P_{rL}. \tag{2.110}$$

The efficiency of the two-switch flyback converter for DCM is

$$\eta \equiv \frac{P_O}{P_I} = \frac{P_O}{P_O + P_{LS}} = \frac{1}{1 + \frac{P_{LS}}{P_O}}. \tag{2.111}$$

Table 2.4: LIST OF COMPONENTS AND THEIR SPECIFICATIONS FOR TWO-SWITCH FLYBACK CONVERTER FOR DCM

Parameter	Value	Component
Power MOSFET maximum voltage stress	60 V	IRF510 - 100 V
Power MOSFET maximum current stress	2.65 A	IRF510 - 5 A
Power MOSFET drain-to-source on-resistance	r_{DS}	IRF510 - 0.54 Ω
Power MOSFET drain-to-source capacitance	C_O	IRF510 - 60 pF
Rectifier diode maximum voltage stress	44 V	MBR10100 - 100 V
Rectifier diode maximum current stress	6.81 A	MBR10100 - 10 A
Rectifier diode forward voltage	V_{F3}	MBR10100 - 0.65 V
Rectifier diode forward resistance	R_{F3}	MBR10100 - 20 mΩ
Clamping diode maximum voltage stress	60 V	MBR10100 - 100 V
Clamping diode maximum current stress	2.65 A	MBR10100 - 10 A
Clamping diode forward voltage	V_{F3}	MBR10100 - 0.65 V
Clamping diode forward resistance	R_{F3}	MBR10100 - 20 mΩ
Flyback transformer core	-	Magnetics Pot Core
Transformer core number	-	0P-42616
Primary winding magnetizing inductance	110 μH	100 μH
Secondary winding magnetizing inductance	18.25 μH	15 μH
Number of primary winding turns	17	18
Number of secondary winding turns	7	7
Primary-to-secondary turns ratio	2.45	2.57
Primary winding leakage inductance	L_{lp}	1.81 μH
Secondary winding leakage inductance	L_{lS}	2.37 μH
Total leakage inductance (primary)	L_l	2.16 μH
Primary winding resistance	r_{T1}	28 mΩ
Secondary winding resistance	r_{T2}	10.8 mΩ
Magnetizing inductance ESR	r_L	73 mΩ
Length of air gap	0.326 mm	0.35 mm

2.10 Simulation and Experimental Results of Two-Switch Flyback Converter for DCM

The hard-switching two-switch flyback converter for DCM is designed for the following specifications:

- Maximum input voltage: $V_{Imax} = 60$ V

- Output voltage: $V_O = 20$ V

- Maximum output power: $P_{Omax} = 30$ W

Table 2.5: LIST OF COMPONENTS AND THEIR SPECIFICATIONS FOR SINGLE-SWITCH FLYBACK CONVERTER FOR DCM

Parameter	Value	Component
Power MOSFET maximum voltage stress	465 V	IRF840 - 500 V
Power MOSFET maximum current stress	2.65 A	IRF840 - 8 A
Power MOSFET drain-to-source on-resistance	r_{DS}	IRF840 - 0.85 Ω
Power MOSFET drain-to-source capacitance	C_O	IRF840 - 120 pF
Rectifier diode maximum voltage stress	44 V	MBR10100 - 100 V
Rectifier diode maximum current stress	6.81 A	MBR10100 - 10 A
Rectifier diode forward voltage	V_{F3}	MBR10100 - 0.65 V
Rectifier diode forward resistance	R_{F3}	MBR10100 - 20 mΩ
Flyback transformer core	-	Magnetics Pot Core
Transformer core number	-	0P-42616
Primary winding magnetizing inductance	110 μH	100 μH
Secondary winding magnetizing inductance	18.25 μH	15 μH
Number of primary winding turns	17	18
Number of secondary winding turns	7	7
Primary-to-secondary turns ratio	2.45	2.57
Primary winding leakage inductance	L_{lp}	1.81 μH
Secondary winding leakage inductance	L_{lS}	2.37 μH
Total leakage inductance (primary)	L_l	2.16 μH
Primary winding resistance	r_{T1}	28 mΩ
Secondary winding resistance	r_{T2}	10.8 mΩ
Magnetizing inductance ESR	r_L	73 mΩ
Length of air gap	0.326 mm	0.35 mm

- Switching frequency: $f_s = 100$ kHz

- Output voltage ripple: $V_r/V_O \leq 5\%$

The two-switch flyback converter for DCM is designed using equations (2.84) - (2.94). The components selected for the experiment and their specifications are given in Table 2.4. The design specifications of the single-switch flyback converter for DCM is given in Table 2.5. Saber models of power MOSFETs IRF510 and power diodes MBR10100 were used for simulation. The predicted theoretical waveforms of Fig. 2.17 were in excellent agreement with the simulation waveforms shown in Fig. 2.19.
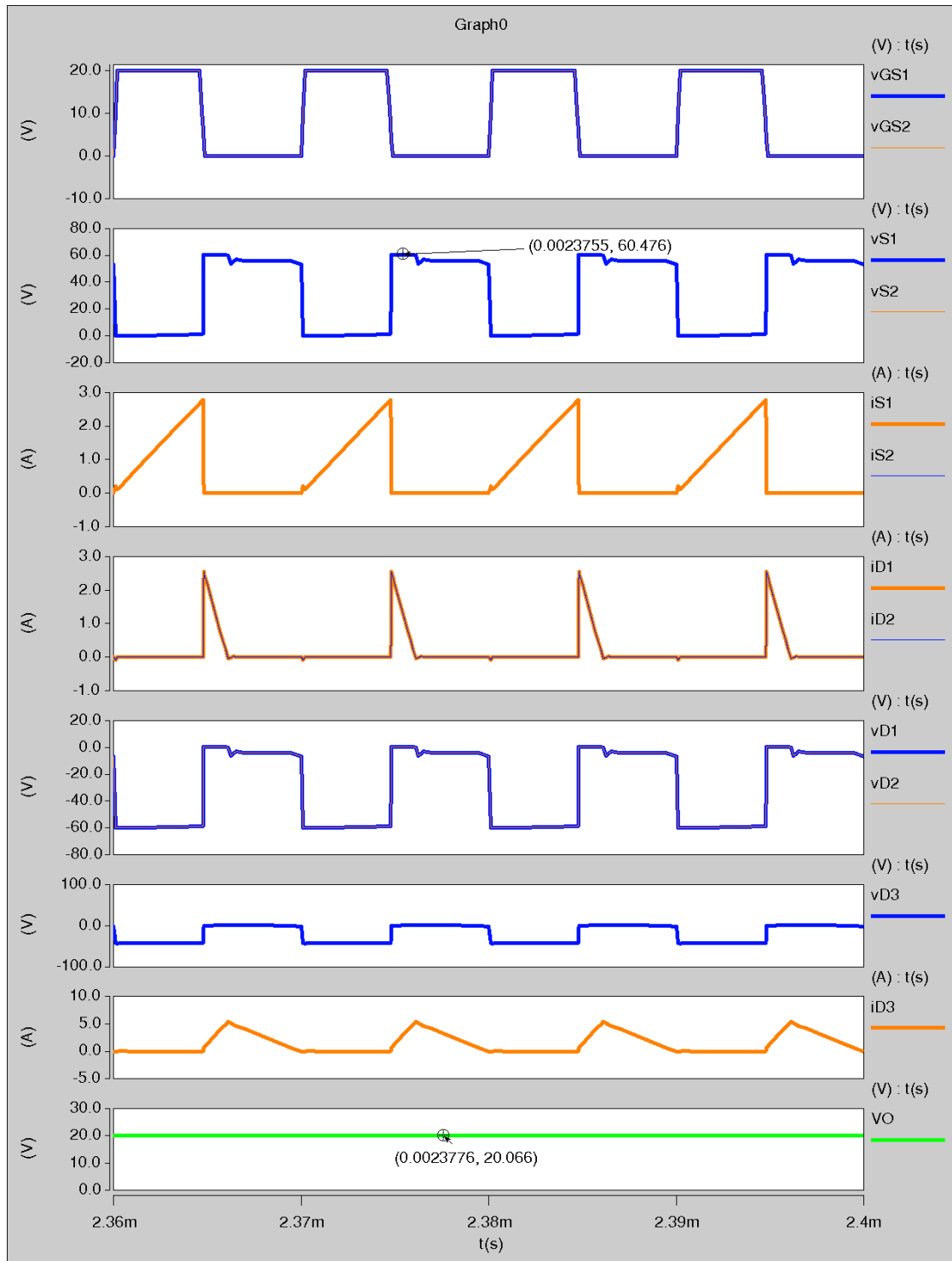
Figure 2.19: Simulation results. Voltage and current waveforms of the hard-switching two-switch flyback PWM DC-DC converter in DCM.
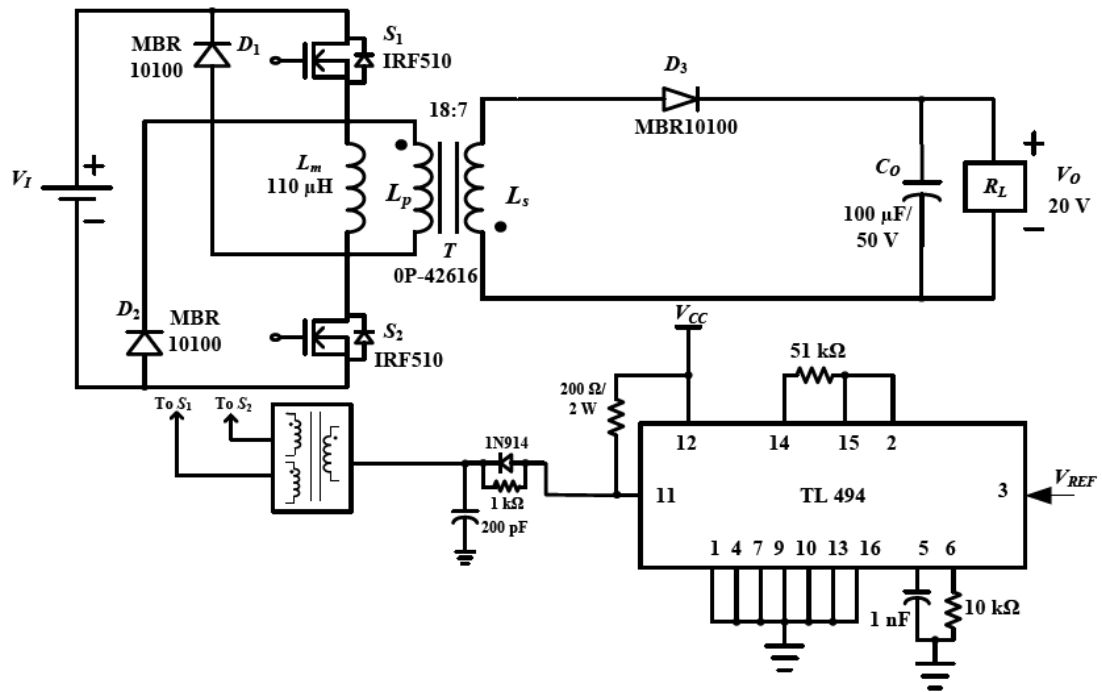
Figure 2.20: Experimental circuit of the two-switch flyback converter for DCM.
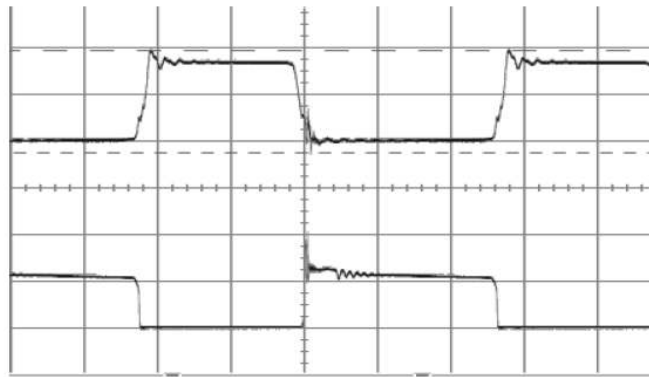
Figure 2.21: Experimental results of the two-switch flyback converter for DCM at P_O = 30 W. Top trace: switch gate-to-source voltage waveforms v_{GS1}, v_{GS2} (10 V/div.) Bottom trace: switch drain-to-source voltage waveforms v_{DS1}, v_{DS2} (50 V/div.). Horizontal scale: 2 μs/div.

The complete schematic of the experimental setup of the two-switch flyback converter is shown in Fig. 2.20. The theoretical voltage and current waveforms of the converter shown in Fig. 2.17 are experimentally verified. The experimental voltage
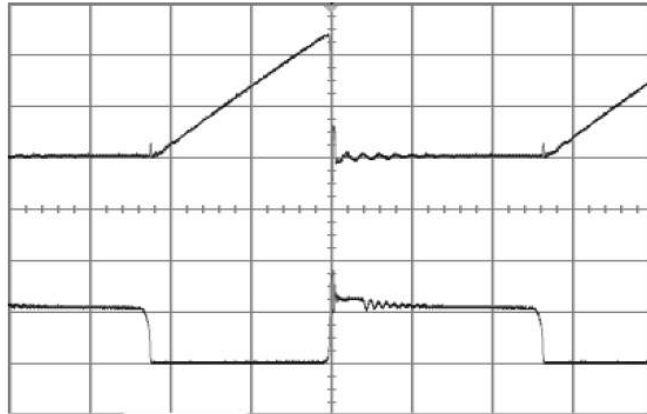
Figure 2.22: Experimental results of the two-switch flyback converter for DCM at $P_O = 30$ W. Top trace: switch current waveforms i_{S1}, i_{S2} (1 A/div.); Bottom trace: switch drain-to-source voltage waveforms v_{S1}, v_{S2} (50 V/div.). Horizontal scale: 2 μs/div.
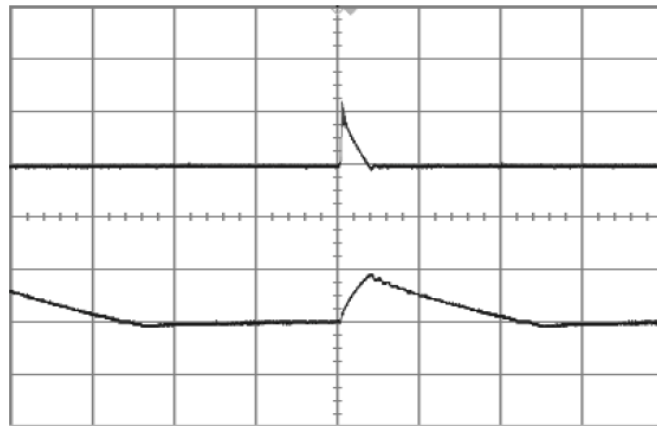
Figure 2.23: Experimental results of the two-switch flyback converter for DCM at $P_O = 30$ W. Top trace: clamping diode current waveforms i_{D1}, i_{D2} (2 A/div.); Bottom trace: rectifier diode current waveform i_{D3} (5 A/div.). Horizontal scale: 2 μs/div.

and current waveforms of the converter at full and light load are presented in Figs. 2.21 - 2.25. The maximum voltage across the power MOSFET switches is measured to be 62.5 V as shown in Figs. 2.21 and 2.24. The switch currents are shown in Figs. 2.22 and 2.24, and the clamping diode currents along with the output rectifier diode current are shown in Figs. 2.23 and 2.25. The rectifier diode D_3 for DCM operation turns off at zero current. The clamping diodes D_1 and D_2 also turn off at zero cur-
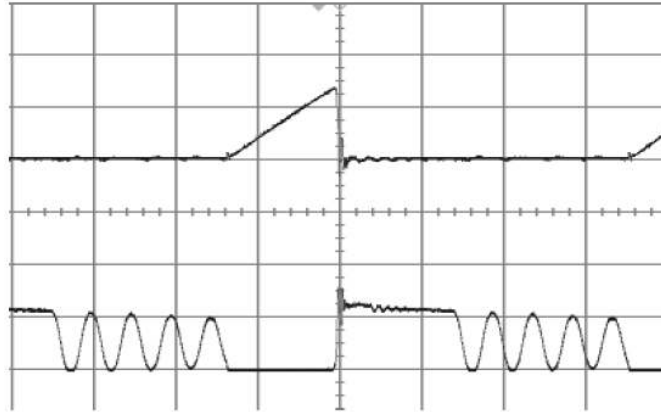
Figure 2.24: Experimental results of the two-switch flyback converter for DCM at $P_O = 8$ W. Top trace: switch current waveforms i_{S1}, i_{S2} (2 A/div.); Bottom trace: switch drain-to-source voltage waveforms v_{S1}, v_{S2} (50 V/div.). Horizontal scale: 2 μs/div.
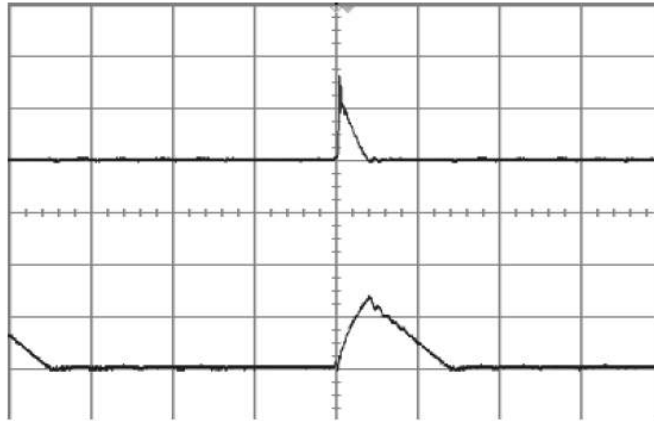
Figure 2.25: Experimental results of the two-switch flyback converter for DCM at $P_O = 8$ W. Top trace: clamping diode current waveforms i_{D1}, i_{D2} (1 A/div.); Bottom trace: rectifier diode current waveform i_{D3} (2 A/div.). Horizontal scale: 2 μs/div.

rent. Therefore, the reverse recovery effects in the diodes are considerably reduced. During light loading conditions, the magnetizing inductor current reaches zero much before the end of the switching period, leading to oscillations between the transistor output capacitance and the transformer leakage inductance as seen in Fig. 2.24. The frequency of the oscillations is given by (2.72). The flyback transformer parameters listed in Table 2.4 are measured using Hewlett Packard 4275A Multi-Frequency LCR
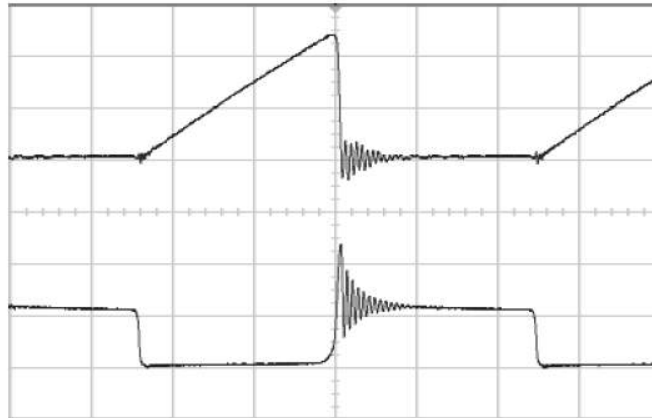
Figure 2.26: Experimental results of the single-switch flyback converter for DCM at $P_O = 30$ W. Top trace: switch current waveform i_S (1 A/div.); Bottom trace: switch drain-to-source voltage waveform v_S (50 V/div.). Horizontal scale: 2 μs/div.

Table 2.6: COMPARISON OF POWER LOSSES OF THE TWO-SWITCH AND THE SINGLE-SWITCH FLYBACK CONVERTERS FOR DCM

	$P_O = 30$ W	$P_O = 10$ W
Parameter	Loss (W)	Loss (W)
Two-Switch Flyback Converter		
MOSFET conduction loss $2P_{rDS}$	1.1316	1.2078
MOSFET switching loss $2P_{SW}$	0.0217	0.0217
Rectifier diode loss P_{D3}	1.1231	0.4144
Clamping diode loss $2P_{D1D2}$	0.138	0.046
Primary winding resistance loss P_{rT1}	0.0293	0.0313
Secondary winding resistance loss P_{rT2}	0.08	0.0483
Magnetizing inductance ESR loss P_{rL}	0.1584	0.1311
Total power loss P_{LS}	2.68	1.9
Converter efficiency η	91.79%	84.03%
Single-Switch Flyback Converter		
MOSFET conduction loss P_{rDS}	0.8906	0.9513
MOSFET switching loss P_{SW}	1.3028	1.3473
Rectifier diode loss P_{D3}	1.1231	0.4144
Clamping diode loss	-	-
Primary winding resistance loss P_{rT1}	0.0293	0.0313
Secondary winding resistance loss P_{rT2}	0.08	0.0483
Magnetizing inductance ESR loss P_{rL}	0.1584	0.1311
Total power loss P_{LS}	3.58	2.92
Converter efficiency η	89.33%	77.39%
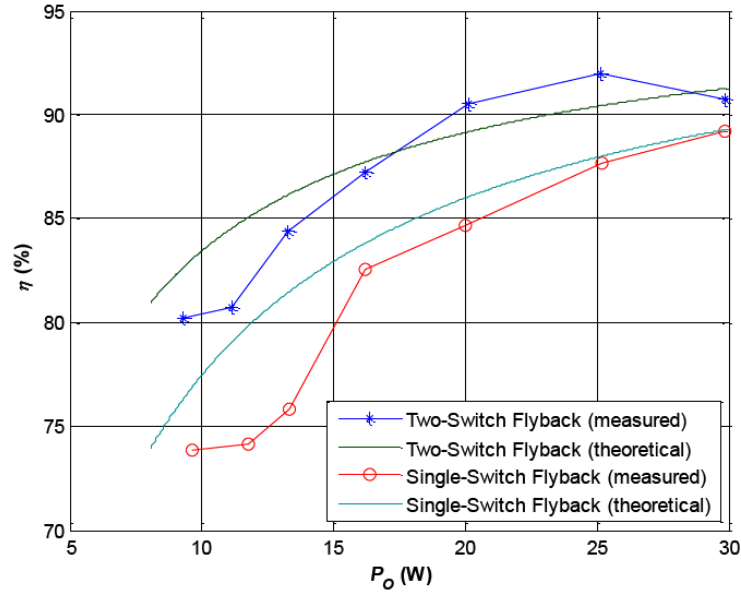
Figure 2.27: Theoretical and experimental efficiencies of the two-switch and the single-switch flyback converters plotted as a function of converter output power for DCM operation.

meter. Table 2.6 gives the comparison of losses of the two-switch and the single-switch flyback converters for full load and light load conditions, respectively. From Table 2.5, it is clearly seen that the maximum voltage stress of the power MOSFET in the single-switch flyback converter is predicted to be 465 V. A MOSFET with higher voltage rating (IRF840, 500 V, 0.85 Ω) is used in the single-switch flyback converter as against a MOSFET with lower voltage rating (IRF510, 100 V, 0.54 Ω), which is safely used in a two-switch topology.

Fig. 2.26 shows the current and voltage waveforms of the power MOSFET used in a single-switch flyback converter for DCM operated at full load. The maximum voltage measured was 125 V which is about 3.5 times lesser than the theoretically predicted value. This difference can be attributed to the effect of stray capacitances and lead inductances in the circuit. Hence, it is difficult to predict the voltage oscillations in the single-switch flyback converter, whereas, in the two-switch flyback converter, the clamping of the switch overvoltage is clearly achieved. Fig. 2.27 compares the

efficiencies of the two-switch flyback converter and the single-switch flyback converter versus the output power for DCM operation. A plot of theoretical efficiency predicted using the equations (2.99) - (2.111) is shown in Fig. 2.27 and is fairly in good agreement with the measured efficiency of the two-switch flyback converter circuit. The total on-resistance of two power MOSFETs used in the two-switch topology is slightly larger than that of the on-resistance of the single MOSFET used in the single-switch version due to which the conduction losses in the two-switch flyback converter is about 1.25 times than that of the single-switch flyback converter. From Table 2.6, it can be clearly seen that the overall losses in the two-switch flyback converter is lesser than that of the single-switch flyback converter largely due to the reduced switching losses in the two-switch flyback converter.

3 Proposed Soft-Switching Two-Switch Flyback PWM DC-DC Converter

3.1 Background

This chapter proposes a soft-switching two-switch flyback PWM DC-DC converter, namely, zero-current transition (ZCT) two-switch flyback PWM DC-DC converter. The auxiliary circuit (active clamp circuit) consisting of an active switch and a clamp capacitor is connected on the secondary side of the transformer of the hard-switching two-switch flyback converter, which results in a soft-switching ZCT two-switch flyback converter. The clamping diodes in the primary side of the classical two-switch flyback topology clamp the peak voltage across each main switch to the DC input voltage. The auxiliary circuit on the secondary side provides zero-current (ZC) switching condition for all the semiconductor devices in the converter. The circuit description, principle of circuit operation, steady-state analysis, and design procedure of the proposed ZCT two-switch flyback converter are presented. Current and voltage waveforms of all the components of the converters are derived. Saber Sketch simulation and experimental results are presented.

3.2 Proposed ZCT Two-Switch Flyback DC-DC Converter

3.2.1 Circuit Description

The circuit of the proposed ZCT two-switch flyback DC-DC converter is shown in Fig. 3.1. The two main switches S_1 and S_2, secondary rectifier diode D_3, and the flyback transformer T form a part of the power circuit responsible for the power transfer from the input source to the load. The clamping diodes D_1 and D_2 on the primary side of the transformer are responsible for the main switch voltage clamping, and the auxiliary circuit consisting of switch S_a and a capacitor C_a on the secondary side of the transformer are responsible for ZCT operation. The output filter capacitor
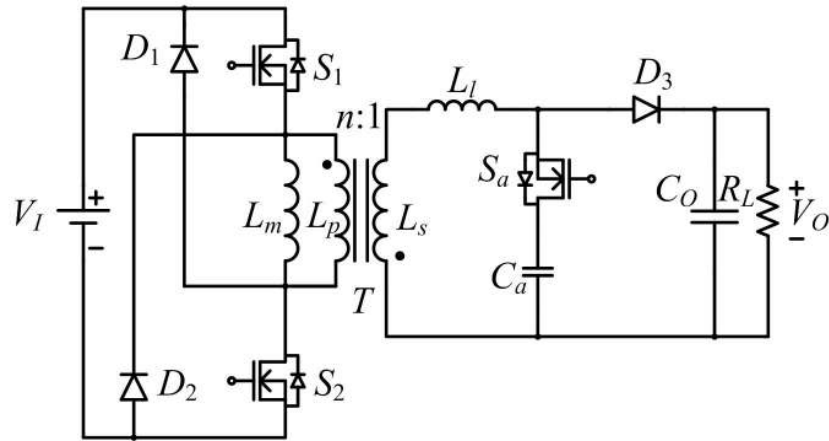
Figure 3.1: ZCT two-switch flyback PWM DC-DC converter.

and the load resistor are denoted by and C_O and R_L, respectively. The input DC voltage and the output voltage are denoted by V_I and V_O, respectively. Both the switches S_1 and S_2 are turned on or off at the same time by an external driver. The auxiliary switch S_a is turned on for a brief period of time before the main switches are turned off and is turned off along with the main switches. The switching period T_s is given by $1/f_s$, where f_s is the switching frequency. The ratio of on-time of main switches t_{on} to total period T_s is defined as the switch duty ratio D. The circuit operation is mainly categorized into six stages. In Fig. 3.1, the transformer T is modeled as an ideal transformer with its magnetizing inductance L_m referred to the primary and the total leakage inductance L_l referred to the secondary.

3.2.2 Assumptions

The steady-state analysis of the ZCT two-switch flyback PWM converter of Fig. 3.1 is based on the following assumptions:

1. The power MOSFETs are ideal switches except for their output capacitances.

2. The diodes are ideal switches.

3. The diode capacitances and lead inductances are zero.

4. The transformer leakage inductance L_l is far lesser than the transformer magnetizing inductance L_m.

5. The magnetizing inductance L_m is large enough to maintain a constant magnetizing inductance current I_{Lm}.

6. Passive components are linear, time-invariant, and frequency-independent.

7. The input and output DC voltages are constant and ripple-free.

8. The converter is operating in steady-state.

9. The switching period $T_s = 1/f_s$ is much smaller than the time constants of reactive components.

10. Before the beginning of switching cycle (time $t = t_0$), the voltage across the auxiliary capacitor $v_{Ca} = V_O$, the magnetizing inductor current is commutated through the rectifier diode D_3, and all other switches and diodes are OFF.

3.2.3 Circuit Operation and Steady-State Analysis

The principle of operation of each stage is explained with the aid of equivalent circuits shown in Fig. 3.2 and the voltage and current waveforms of the ZCT two-switch flyback converter shown in Fig. 3.3.

Stage 1 $(t_0 < t \leq t_1)$: At time $t = t_0$, both the switches S_1 and S_2 are turned on by an external driver. The leakage inductance L_l prevents the instantaneous transfer of magnetizing current from transformer secondary to the primary. Hence, the rectifier diode remains in on-state. An equivalent circuit for this stage is shown in Fig. 3.2(a). The clamping diodes D_1 and D_2 are reverse biased and hence their currents i_{D1} and i_{D2} are zero. Since $v_{Ca} = V_O$, the body diode of S_a is OFF. The leakage inductance L_l limits the rate of rise of current through the switches. The voltage across the leakage
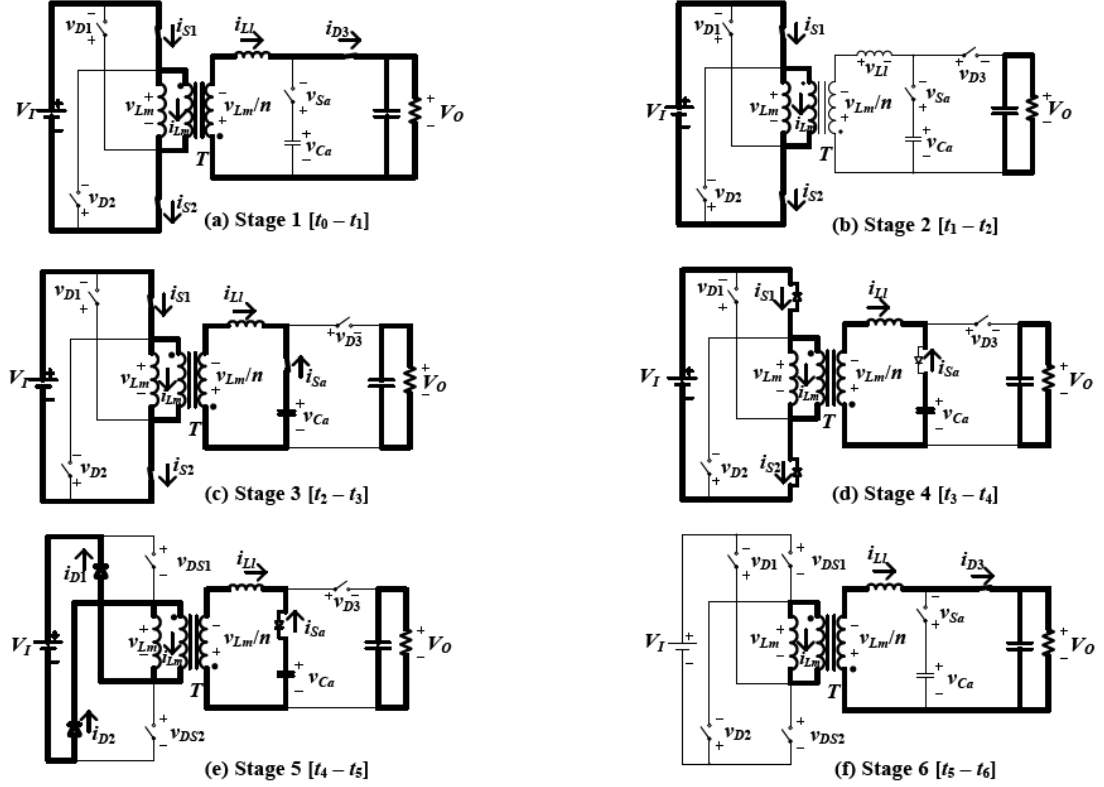
Figure 3.2: Equivalent circuits of the ZCT two-switch flyback converter at different stages of a switching cycle. (a) Stage 1 ($t_0 < t \le t_1$). (b) Stage 2 ($t_1 < t \le t_2$). (c) Stage 3 ($t_2 < t \le t_3$). (d) Stage 4 ($t_3 < t \le t_4$). (e) Stage 5 ($t_4 < t \le t_5$). (f) Stage 6 ($t_5 < t \le t_6$).

inductance is $-(V_I/n + V_O)$. The current through the leakage inductance and the rectifier diode D_3 falls from nI_{Lm} to zero given by

$$i_{Ll} = i_{D3} = nI_{Lm} - \frac{V_I + nV_O}{nL_l}(t - t_0).$$ (3.1)

This stage ends at time $t = t_1$ when the current through the main switches i_{S1}, i_{S2} reaches I_{Lm} and the rectifier diode D_3 turns off with zero current. The duration of this time interval is

$$\Delta t_1 = t_1 - t_0 = \frac{n^2 I_{Lm} L_l}{V_I + nV_O}.$$ (3.2)

Stage 2 ($t_1 < t \le t_2$): During this stage the switches S_1, S_2 are ON and all the diodes D_1, D_2, D_3, and the auxiliary switch S_a are OFF. An equivalent circuit for
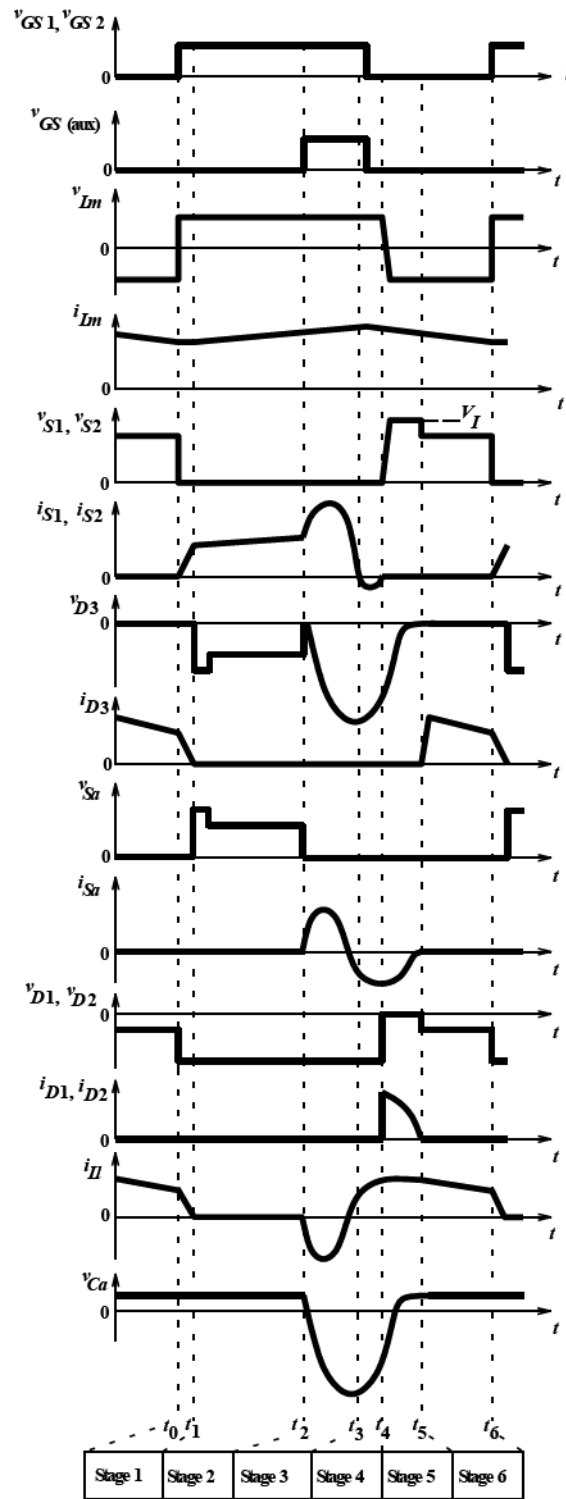
Figure 3.3: Voltage and current waveforms of the ZCT two-switch flyback PWM DC-DC converter.

this stage is shown in Fig. 3.2(b). The voltage across the magnetizing inductance is V_I. The magnetizing inductance is linearly charged by the input voltage source. The switch current i_{S1}, i_{S2} equals I_{Lm}. This stage ends at time $t = t_2$, when the auxiliary switch S_a is turned on by an external driver. The control signal to S_a must be applied at $DT_s(3\pi/2\omega_o)$, where ω_o is given in *Stage 3*.

Stage 3 $(t_2 < t \leq t_3)$: During this stage, the switches S_1, S_2, and S_a are ON and all the diodes D_1, D_2, and D_3 are OFF. An equivalent circuit for this stage is depicted in Fig. 3.2(c). The auxiliary switch S_a turns on softly. The transformer leakage inductance L_l and the clamp capacitor C_a begin to resonate. The voltage across C_a begins to decrease in a resonant manner. The resonant currents i_{Ll}, i_{S1}, i_{S2}, and the resonant voltage v_{Ca} are given as

$$i_{Ll} = -\frac{V_I + nV_O}{nZ_o} \sin\omega_o(t - t_2), \tag{3.3}$$

$$i_{S1} = i_{S2} = I_{Lm} - \frac{i_{Ll}}{n} = I_{Lm} + \frac{V_I + nV_O}{n^2 Z_o} \sin\omega_o(t - t_2), \tag{3.4}$$

$$v_{Ca} = \left(\frac{V_I}{n} + V_O\right)\cos\omega_o(t - t_2) - \frac{V_I}{n}, \tag{3.5}$$

where the resonant frequency ω_o is given by

$$\omega_o = \frac{1}{\sqrt{L_l C_a}}, \tag{3.6}$$

and the characteristic impedance Z_o is

$$Z_o = \sqrt{\frac{L_l}{C_a}}. \tag{3.7}$$

When the currents i_{S1}, i_{S2} reach I_{Lm}, the current through L_l reaches zero and the voltage across C_a is $-(2V_I/n + V_O)$. The transformer leakage inductance L_l and the clamp capacitor C_a continue to resonate with the exception that the leakage current i_{Ll} reverses and flows through the body diode of switch S_a. The capacitor C_a begins

to charge from $-(2V_I/n + V_O)$. The resonant currents i_{Ll}, i_{S1}, i_{S2}, and the resonant voltage v_{Ca} are given as

$$i_{Ll} = \frac{V_I + nV_O}{nZ_o} \sin \omega_o(t - t_2), \tag{3.8}$$

$$i_{S1} = i_{S2} = I_{Lm} - \frac{i_{Ll}}{n} = I_{Lm} - \frac{V_I + nV_O}{n^2 Z_o} \sin \omega_o(t - t_2), \tag{3.9}$$

and

$$v_{Ca} = -\left(\frac{V_I}{n} + V_O\right) \cos \omega_o(t - t_2) - \frac{V_I}{n}. \tag{3.10}$$

This stage ends at time $t = t_3$ when the current through L_l reaches nI_{Lm} thus forcing the currents in the main switches to zero. Assuming that the time duration for which i_{Ll} reverses and flows through the body diode of the switch S_a is $\pi/2\omega_o$, the condition for the main switch currents i_{S1}, i_{S2} to reach zero is established as

$$i_{Lm} \leq \frac{V_I + nV_O}{n^2 Z_o}, \tag{3.11}$$

and the capacitor voltage v_{Ca} is found as $-V_I/n$.

Stage 4 $(t_3 < t \leq t_4)$: An equivalent circuit for this stage is depicted in Fig. 3.2(d). The transformer leakage inductance L_l and the clamp capacitor C_a continue to resonate as in *Stage* 3 with the exception that the main switch currents i_{S1}, i_{S2} reverses and flows through the body diodes of switches S_1 and S_2, respectively. Since the body diodes of all the switches are conducting, this interval is the best time to turn off the main switches S_1, S_2 and the auxiliary switch S_a to achieve zero current condition. The resonant currents i_{Ll}, i_{S1}, i_{S2}, and the resonant voltage v_{Ca} are given as

$$i_{Ll} = nI_{Lm} + \frac{V_I + nV_O}{nZ_o} \sin \omega_o(t - t_3), \tag{3.12}$$

$$i_{S1} = i_{S2} = I_{Lm} - \frac{i_{Ll}}{n} = -\frac{V_I + nV_O}{n^2 Z_o} \sin \omega_o(t - t_3), \tag{3.13}$$

and

$$v_{Ca} = -\left(\frac{V_I}{n} + V_O\right)\cos\omega_o(t - t_3) - \frac{V_I}{n}. \tag{3.14}$$

This stage ends at time $t = t_4$ when the body diodes of S_1 and S_2 are naturally turned off.

Stage 5 ($t_4 < t \leq t_5$): During this stage, the switches S_1, S_2, S_a and the rectifier diode D_3 are OFF. An equivalent circuit for this stage is depicted in Fig. 3.2(e). The resonance between L_l and C_a continue as in *Stage 4* with the exception that leakage current i_{Ll} commutates through the clamping diodes D_1, and D_2 due to which the voltage across the main switches v_{S1} and v_{S2} is clamped to the input voltage V_I. The voltage across the clamp capacitor v_{Ca} continues to build towards V_O. The resonant currents i_{Ll}, i_{D1}, i_{D2}, and the resonant voltage v_{Ca} are given as

$$i_{Ll} = nI_{Lm} - \frac{V_I + nV_O}{nZ_o}\sin\omega_o(t - t_4), \tag{3.15}$$

$$i_{D1} = i_{D2} = I_{Lm} - \frac{i_{Ll}}{n} = \frac{V_I + nV_O}{n^2 Z_o}\sin\omega_o(t - t_4), \tag{3.16}$$

and

$$v_{Ca} = -\left(\frac{V_I}{n} + V_O\right)\cos\omega_o(t - t_4) - \frac{V_I}{n}. \tag{3.17}$$

This stage ends at time $t = t_5$ when the voltage across the clamp capacitor v_{Ca} reaches V_O turning off the body diode of S_a, the current through D_1 and D_2 reach zero, and i_{Ll} equals I_{Lm}. The duration of this time interval is

$$\Delta t_5 = t_5 - t_4 = \frac{\pi}{\omega_o}. \tag{3.18}$$

Stage 6 ($t_5 < t \leq t_6$): During this stage, the switches S_1, S_2, S_a and the diodes D_1, D_2, are OFF. An equivalent circuit for this stage is depicted in Fig. 3.2(f). The auxiliary circuit is completely removed thus forcing the commutation of magnetizing inductance current I_{Lm} to the output via rectifier diode D_3. The leakage inductance

current i_{Ll} equals I_{Lm}. This stage ends at time $t = t_6$, when both the main switches S_1 and S_2 are turned on by an external driver completing one full switching cycle.

3.3 Design of ZCT Two-Switch Flyback Converter

3.3.1 DC Voltage Transfer Function

Referring to the voltage waveform of the magnetizing inductance in Fig. 3.3 and applying volt-second balance, we have

$$V_I(\Delta t_1 + \Delta t_2 + \Delta t_3 + \Delta t_4) = nV_O(\Delta t_5 + \Delta t_6). \tag{3.19}$$

Assuming that the time duration of *Stages* 1 and 4 are very small in comparison with those of *Stages* 2, 3, 5, and 6, the DC voltage transfer function is approximately

$$M_{VDC} \equiv \frac{V_O}{V_I} = \frac{(\Delta t_1 + \Delta t_2 + \Delta t_3 + \Delta t_4)}{n(\Delta t_5 + \Delta t_6)} = \frac{D}{n(1 - D)}. \tag{3.20}$$

The DC current transfer function is given by

$$M_{IDC} \equiv \frac{I_O}{I_I} = \frac{n(1 - D)}{D}. \tag{3.21}$$

3.3.2 Device Stresses

The selection of components is based on the maximum values of the voltage and current stresses of the switches and the diodes. During *Stage* 5, the maximum off-state voltage appearing across S_1 and S_2 is given by

$$V_{SM1(\text{max})} = V_{SM2(\text{max})} = V_{I(\text{max})}. \tag{3.22}$$

During *Stage* 3, the maximum value of the current through the main switches is

$$I_{SM1(\text{max})} = I_{SM2(\text{max})} \cong I_{Lm} + \frac{V_I + nV_O}{n^2 Z_O} = \frac{DP_{O(\text{max})}}{nV_O(1 - D)} + \frac{V_O}{nDZ_O}, \tag{3.23}$$

where $I_{Lm} = I_I$. During *Stage* 3, the maximum value of the diode reverse voltage is

$$V_{DM3(\text{max})} \cong \frac{2V_I}{n} + 2V_O = \frac{2V_O}{D}. \tag{3.24}$$

However, at the beginning of *Stage* 2, the output capacitance of the auxiliary switch $C_{o(aux)}$ and the leakage inductance L_l resonate due to which the rectifier diode peak reverse voltage is approximately

$$V_{DM3(\mathrm{max})} \cong \frac{V_I}{n} + V_O + I_{DM3(t1)}Z = \frac{V_O}{D} + I_{DM3(t1)}Z. \qquad (3.25)$$

where

$$Z = \sqrt{\frac{L_l}{C_{O(aux)}}}. \qquad (3.26)$$

In practice, since i_{D3} is very small just before the rectifier diode turns off, $I_{DM3(t_1)}$ can be taken as 10% of I_O. During *Stage* 6, the maximum value of the current through the rectifier diode is

$$I_{DM3(\mathrm{max})} \cong \frac{I_O}{1-D} = \frac{P_{O(\mathrm{max})}}{V_O(1-D)}. \qquad (3.27)$$

During *Stages* 1 through 4, the maximum values of the clamping diode reverse voltage are

$$V_{DM1(\mathrm{max})} = V_{DM2(\mathrm{max})} = V_{I(\mathrm{max})}. \qquad (3.28)$$

During *Stage* 5, the maximum value of the current through the clamping diodes is

$$I_{DM1(\mathrm{max})} = I_{DM2(\mathrm{max})} \cong \frac{V_I + nV_O}{n^2 Z_o} = \frac{V_O}{nDZ_O}. \qquad (3.29)$$

Using (3.25), the maximum off-state voltage appearing across S_a is given by

$$V_{SMa(\mathrm{max})} \cong \frac{V_I}{n} + V_O + I_{DM3(t1)}Z = \frac{V_O}{D} + I_{DM3(t1)}Z. \qquad (3.30)$$

During *Stage* 3, the maximum value of the current through the auxiliary switch is

$$I_{SMa(\mathrm{max})} \cong \frac{V_I + nV_O}{nZ_o} = \frac{V_O}{DZ_O}. \qquad (3.31)$$

3.3.3   Design Procedure

From the design specifications, find the maximum value of M_{VDC}

$$M_{VDC(\mathrm{max})} = \frac{V_O}{V_{I(min)}}. \qquad (3.32)$$

Rearranging (3.32), the transformer turns ratio is given by

$$n = \frac{D_{\max}}{M_{VDC(\max)}(1 - D_{\max})}.$$ (3.33)

Since the current waveform of the magnetizing inductance is similar to that of the single-switch flyback converter, the usual method to determine the value of the magnetizing inductance can be used.

$$L_{m(\min)} = \frac{n^2 R_{L\max}(1 - D_{\min})^2}{2f_s}.$$ (3.34)

Using (3.33) and (3.34), the flyback transformer can be designed and hence the value of leakage inductance L_l can be obtained. In order to achieve ZC switching of the main switches, the inequality (3.11) must be satisfied. Using (3.11) and (3.7), the value of clamp capacitor can be estimated as

$$C_a \geq \frac{n^4 L_l I_{Lm}^2}{(V_I + nV_O)^2} = \frac{D^4 L_l P_{O(\max)}^2}{V_O^4(1 - D)^2}.$$ (3.35)

Using (3.24) or (3.25), the maximum voltage stress of the clamping capacitor can be found. Selection of the output filter capacitor is based on the output voltage ripple specifications.

$$C = \frac{D_{\max} V_O}{f_s R_{L\min} V_{cpp}},$$ (3.36)

where V_{cpp} is the peak-to-peak value of the ac component of the voltage across the capacitance, which is approximately

$$V_{cpp} \approx V_r - V_{rcpp}.$$ (3.37)

In (3.37), V_r is the peak-to-peak value of the output ripple voltage and V_{rcpp} is the peak-to-peak value of the voltage across the equivalent series resistance (ESR) r_C of the capacitor.
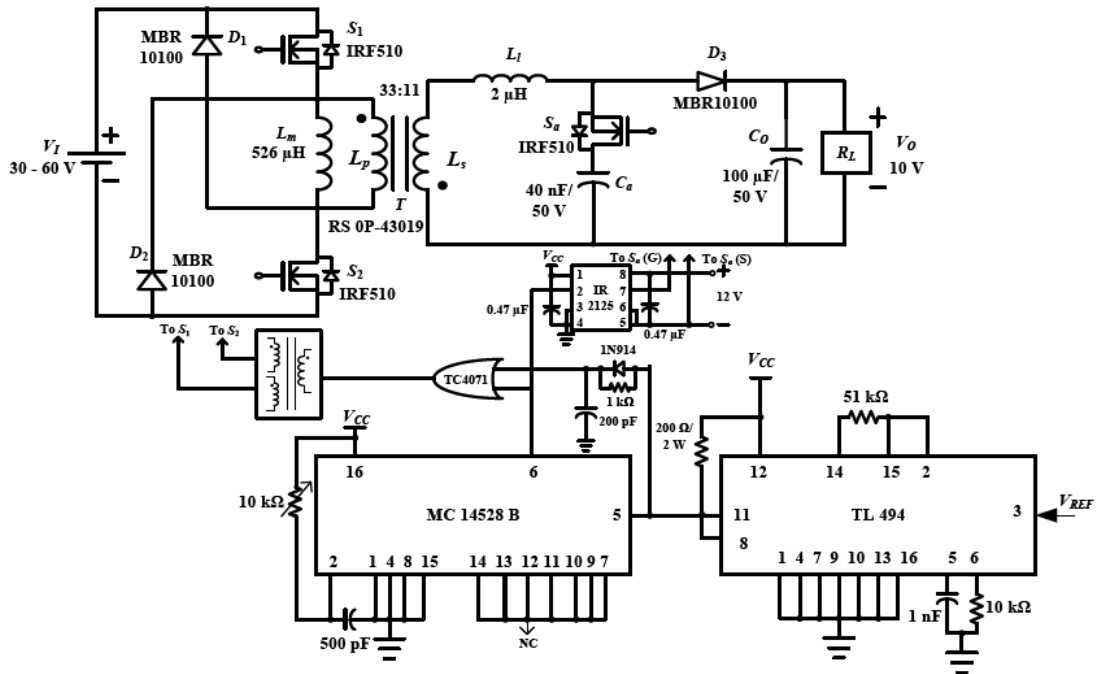
Figure 3.4: Experimental setup of the ZCT two-switch flyback converter.
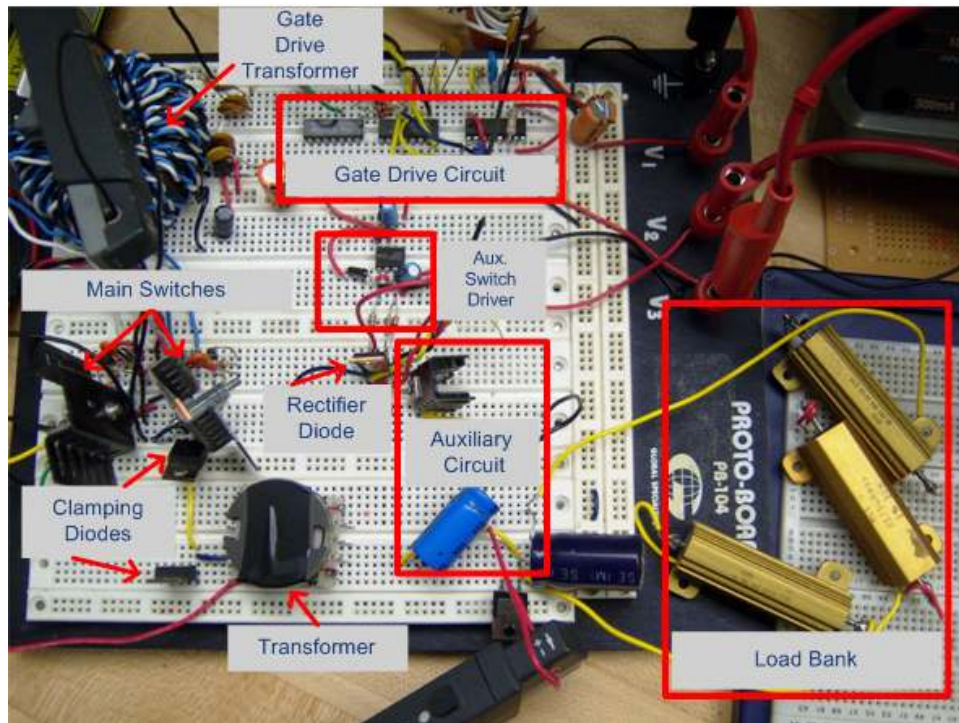
Figure 3.5: Photograph of the experimental circuit of the ZCT two-switch flyback converter.
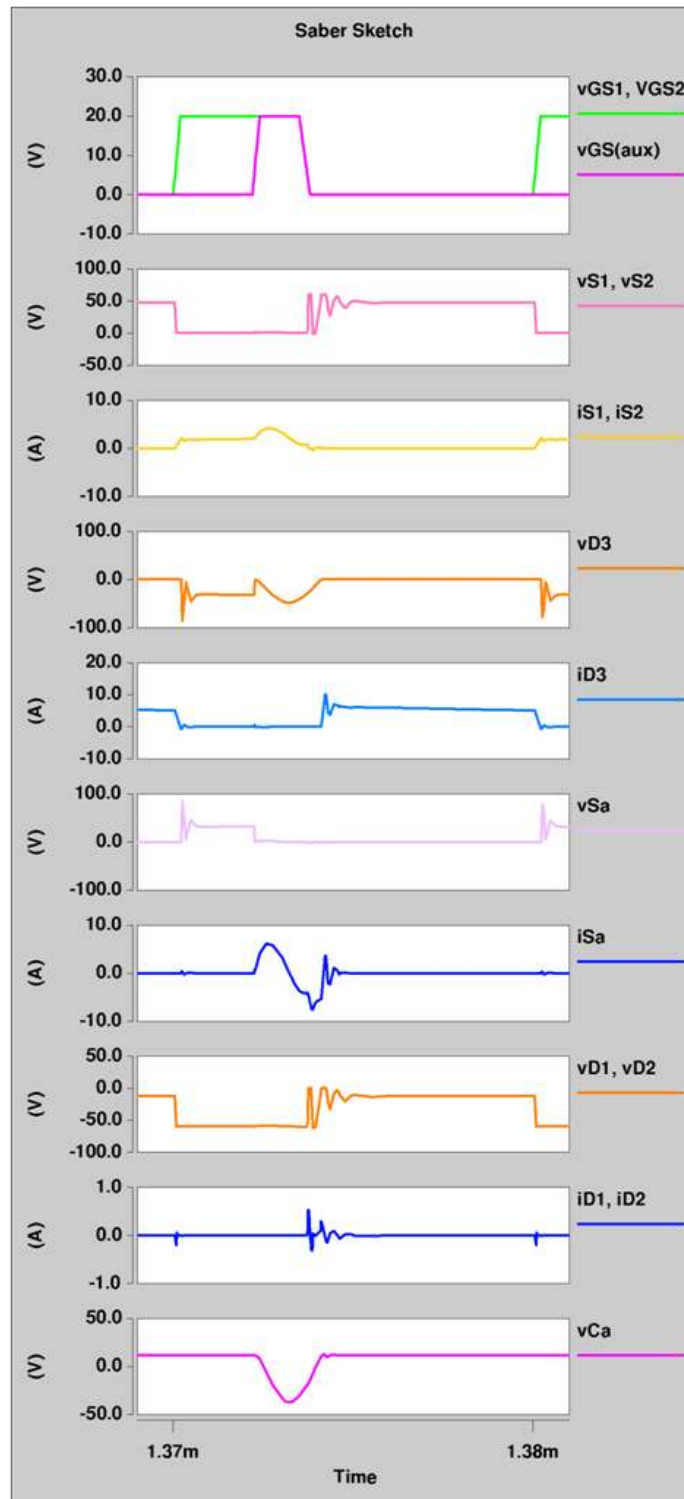
Figure 3.6: Simulation results. Voltage and current waveforms of the soft-switching ZCT two-switch flyback PWM DC-DC converter.
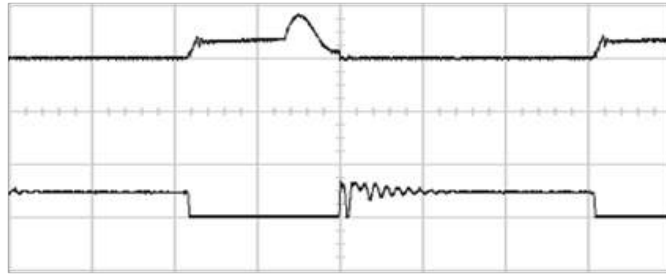
Figure 3.7: Experimental results. Top trace: main switch current waveforms i_{S1} and i_{S2} (5 A/div.); Bottom trace: main switch drain-to-source voltage waveforms v_{S1} and v_{S2} (100 V/div.). Horizontal scale: 2 μs/div.
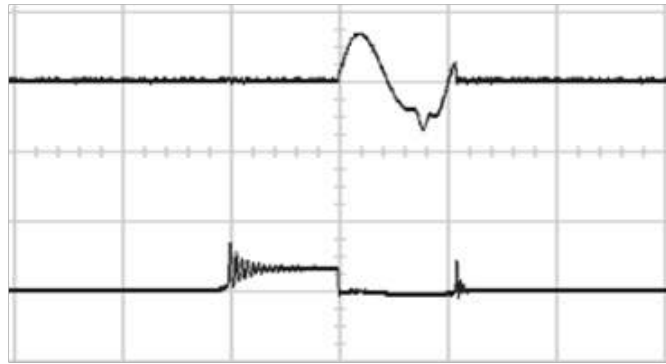
Figure 3.8: Experimental results. Top trace: auxiliary switch current waveform i_{Sa} (10 A/div.); Bottom trace: auxiliary switch drain-to-source voltage waveform v_{Sa} (100 V/div.). Horizontal scale: 2 μs/div.
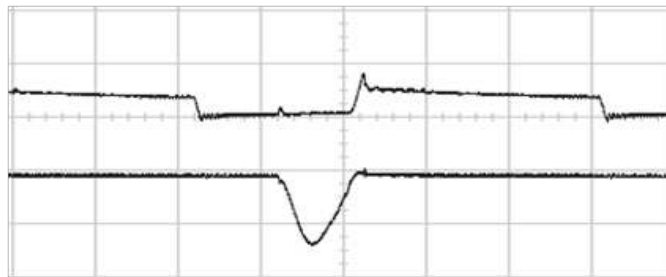
Figure 3.9: Experimental results. Top trace: rectifier diode current waveform i_{D3} (10 A/div.); Bottom trace: auxiliary capacitor voltage waveform v_{Ca} (100 V/div.). Horizontal scale: 2 μs/div.

3.4 Simulation and Experimental Results of ZCT Two-Switch Flyback Converter

The soft-switching ZCT two-switch flyback converter is designed for the following specifications:
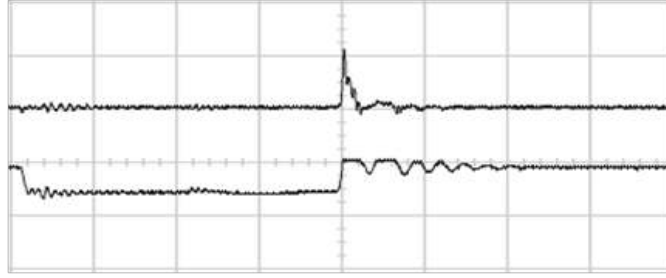
Figure 3.10: Experimental results. Top trace: clamping diode current waveforms i_{D1} and i_{D2} (0.5 A/div.); Bottom trace: clamping diode voltage waveforms v_{D1} and v_{D2} (100 V/div.). Horizontal scale: 1 μs/div.

- Input voltage: $V_I = 45 \pm 15$ V

- Output voltage: $V_O = 10$ V

- Maximum output power: $P_{Omax} = 30$ W

- Minimum output power: $P_{Omin} = 3$ W

- Switching frequency: $f_s = 100$ kHz

- Output voltage ripple: $V_r/V_O \leq 5\%$

The ZCT two-switch flyback converter is designed using equations (3.22) to (3.36). The detailed circuit of the ZCT two-switch flyback converter used for the experiment is shown in Fig. 3.4 and the photograph of the experimental circuit of the ZCT two-switch flyback converter is shown in Fig. 3.5. Saber models of IRF510 and MBR10100 are used for simulation study. The theoretical voltage and current waveforms of the converter shown in Fig. 3.3 are verified by Saber Sketch simulation results shown in Fig. 3.6, and experimental results shown in Figs. 3.7 - 3.10 for $V_I = 60$ V. From Figs. 3.6 - 3.10, it can be clearly seen that the simulation and experimental results are in excellent agreement with each other and also with the theoretical waveforms of Fig. 3.3. The current and voltage waveforms of the main switches and the auxiliary switch are presented in Figs. 3.7 and 3.8, respectively, from which, the soft turn-on and

turn-off of the main switches and the auxiliary switch can be confirmed. The current waveform of the rectifier diode, the voltage waveform of the auxiliary capacitor, and the current and voltage waveforms of the clamping diodes are presented in Figs. 3.9 and 3.10, respectively. It should be noted that the rectifier diode and also the clamping diodes are softly commutated. Therefore, the switching losses of the proposed ZCT two-switch flyback converter are significantly reduced. The maximum voltage across the power MOSFET switches is clamped to the DC input voltage of $V_I = 60$ V. The main drawback of this circuit is the higher voltage stress of the auxiliary switch and the rectifier diode.

4 Harmonic Winding Loss in High-Frequency Transformers

4.1 Background

High-frequency transformers used in PWM converters conduct nonsinusoidal currents, which give rise to additional winding losses due to harmonics. This chapter presents expressions for winding power losses in a two-winding transformer subject to nonsinusoidal excitation operated in continuous conduction mode (CCM) and discontinuous conduction mode (DCM). Dowell's equation is used to determine the winding resistances due to eddy currents as a function of frequency. Fourier series of the primary and secondary current waveforms in isolated DC-DC power converters and the primary and secondary winding resistances are used to determine the primary and secondary winding power losses at various harmonics, respectively. The harmonic primary and secondary winding loss factors F_{Rph} and F_{Rsh} are introduced.

4.2 Dowell's Equation

Consider a winding with multiple layers N_l as shown in Fig. 4.1. Each layer of the winding consists of a single turn of a rectangular foil whose width, thickness, and length are denoted by b, h, and l, respectively. The winding ac resistance for the winding shown in Fig. 4.1 is given by Dowell's equation [25] under the following assumptions:

1. The winding consists of straight conductors parallel to each other and parallel to the center post of the core.

2. The curvature, edge, and end effects of the conductors are neglected.

3. The core material has high permeability ($\mu_{rc} = \infty$) and the winding layers fill the entire width b of the bobbin due to which the alternating magnetic flux
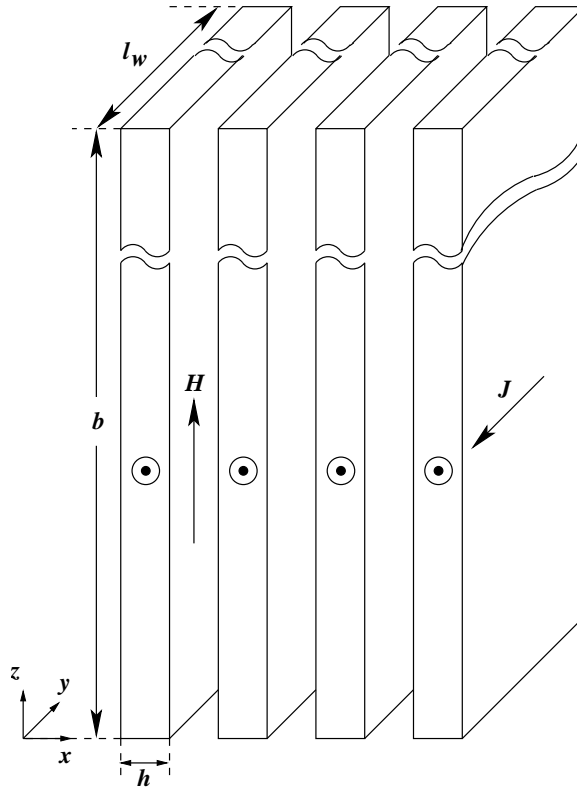
Figure 4.1: Multilayer winding made up of straight, parallel foil conductors.

density $B(t)$ is parallel everywhere to the foil winding (z-direction).

4. The sinusoidal current flows through the winding conductor.

5. The end effects are neglected because $h \ll b$ and $h \ll l$.

6. The capacitive effects are neglected.

Using a one-dimensional solution, the impedance Z of a multilayer foil rectangular conductor winding of N_l layers is given by [25]

$$Z = \frac{\rho_{wf} l_{wf} \gamma h}{h b_{wf}} \left[\coth\left(\gamma h\right) + \frac{2(N_l^2 - 1)}{3} \tanh\left(\frac{\gamma h}{2}\right) \right]$$

$$= R_{wdc}(1 + j) \left(\frac{h}{\delta_w}\right) \left\{ \coth\left[(1 + j)\left(\frac{h}{\delta_w}\right)\right] + \frac{2(N_l^2 - 1)}{3} \tanh\left[(1 + j)\left(\frac{h}{\delta_w}\right)\right] \right\}$$

$$= R_w + j\omega L, \tag{4.1}$$

where R_{wdc} is the DC winding resistance. The normalized winding impedance of a multilayer foil conductor winding can be expressed as

$$\frac{Z}{R_{wdc}} = \left(\frac{h}{\delta_w}\right)\left[\frac{\sinh\left(\frac{2h}{\delta_w}\right) + \sin\left(\frac{2h}{\delta_w}\right)}{\cosh\left(\frac{2h}{\delta_w}\right) - \cos\left(\frac{2h}{\delta_w}\right)} + j\frac{\sinh\left(\frac{2h}{\delta_w}\right) - \sin\left(\frac{2h}{\delta_w}\right)}{\cosh\left(\frac{2h}{\delta_w}\right) - \cos\left(\frac{2h}{\delta_w}\right)}\right]$$

$$+\frac{2(N_l^2 - 1)}{3}\left(\frac{h}{\delta_w}\right)\left[\frac{\sinh\left(\frac{h}{\delta_w}\right) - \sin\left(\frac{h}{\delta_w}\right)}{\cosh\left(\frac{h}{\delta_w}\right) + \cos\left(\frac{h}{\delta_w}\right)} + j\frac{\sinh\left(\frac{h}{\delta_w}\right) + \sin\left(\frac{h}{\delta_w}\right)}{\cosh\left(\frac{h}{\delta_w}\right) + \cos\left(\frac{h}{\delta_w}\right)}\right]. \tag{4.2}$$

The winding ac resistance caused by both skin and proximity effects for a wide foil winding with a single turn per layer is [25]

$$R_w = Re\{Z\} = R_{wdc}A\left\{\frac{\sinh(2A) + \sin(2A)}{\cosh(2A) - \cos(2A)} + \left[\frac{2(N_l^2 - 1)}{3}\right]\frac{\sinh(A) - \sin(A)}{\cosh(A) + \cos(A)}\right\}$$

$$= F_{Rh}R_{wdc}, \tag{4.3}$$

where the skin and proximity effect factor is the winding ac-to-dc resistance ratio

$$F_R = \frac{R_w}{R_{wdc}} = F_S + F_P = A\left\{\frac{\sinh(2A) + \sin(2A)}{\cosh(2A) - \cos(2A)} + \left[\frac{2(N_l^2 - 1)}{3}\right]\frac{\sinh(A) - \sin(A)}{\cosh(A) + \cos(A)}\right\}.$$
$$\tag{4.4}$$

In (4.4), the first term represents the winding ac resistance due to *skin effect* F_S and the second term the winding ac resistance due to *proximity effect* F_P. The DC winding resistance is

$$R_{wdc} = \frac{\rho_{wf}l_w}{A_w} = \frac{\rho_{wf}l_w}{hb_{wf}} = \frac{\rho_{wf}l_T N_l}{hb_{wf}}, \tag{4.5}$$

where l_T is the mean-turn length. The foil thickness normalized with respect to the foil skin depth is

$$A = \frac{h}{\delta_{wf}} = h\sqrt{\frac{\pi\mu f_s}{\rho_{wf}}}. \tag{4.6}$$

The factor F_R depends upon the ratio h/δ_{wf} and N_l. Fig. 4.2 shows the normalized ac winding resistance F_R versus d/δ_w at $d/p = 0.8$ and different number of layers N_l for a round wire.
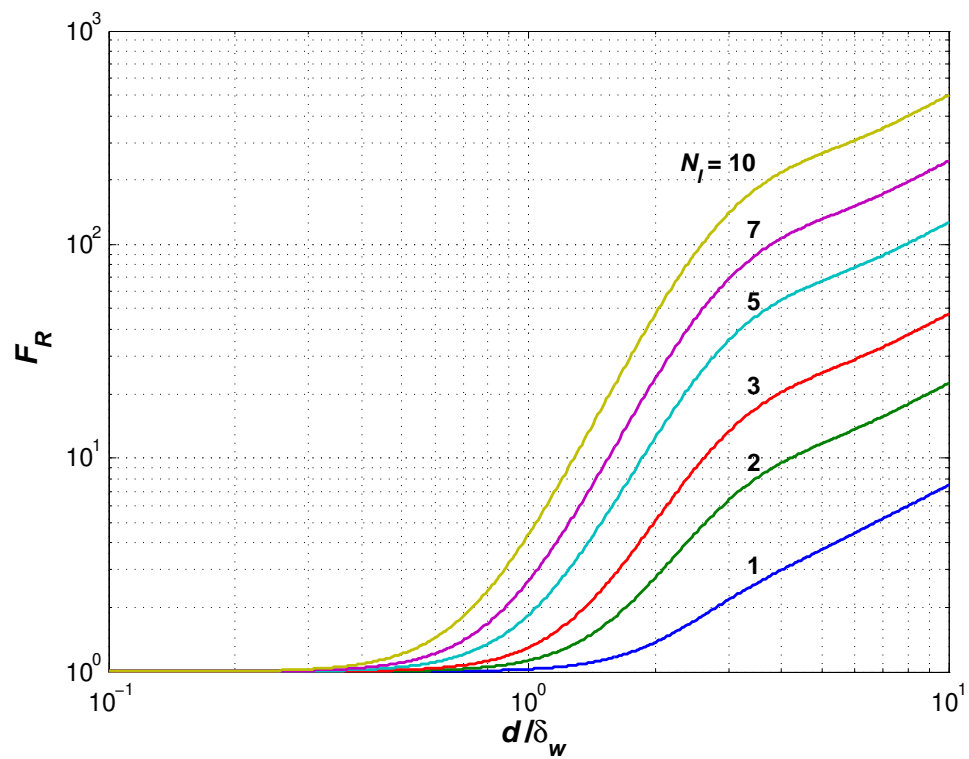
Figure 4.2: Normalized ac winding resistance F_R versus d/δ_w at $d/p = 0.8$ and different number of layers N_l for a round wire.
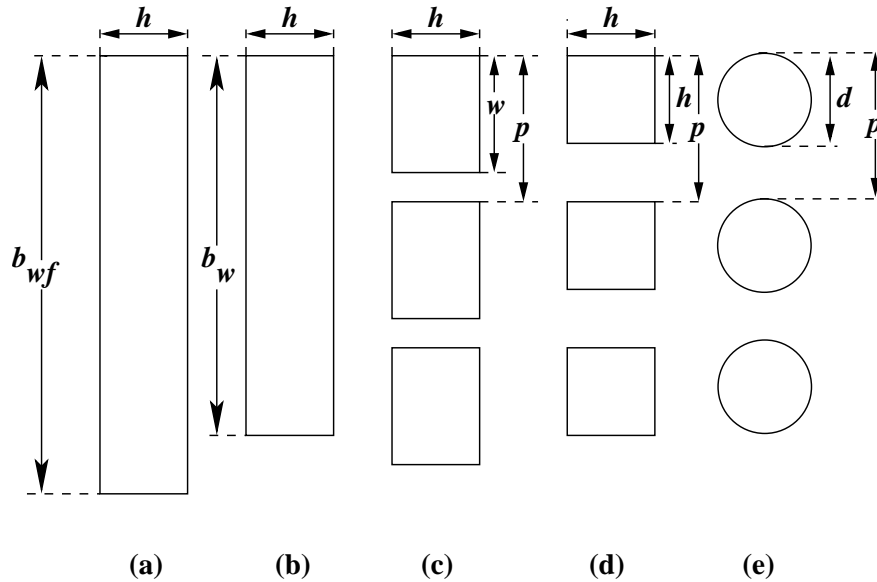
Figure 4.3: Transformations of a foil winding to rectangular, square, and round wire windings. (a) Wide foil winding. (b) Narrow foil winding. (c) Rectangular winding conductor. (d) Square winding conductor. (e) Round winding wire.

4.3 Transformation of Foil Conductor to Rectangular, Square, and Round Conductors

Dowell's equation for the winding with a single wide foil per layer given in previous section can be extended to other winding conductor shapes, such as rectangular, square, and round winding conductors. Fig. 4.3 shows the transformation of foil winding into various shapes of winding conductors. The transformation is carried out by appropriately adjusting the resistivity and a layer fill factor or by using a square-to-round conversion. A porosity factor (i.e., a layer fill factor) can be introduced when converting one sheet of a foil conductor into several equivalent conductors to ensure that the dc resistance of the windings remains unchanged. A sheet of a foil shown in Fig. 4.3(a) first replaced by a narrow sheet of a foil is depicted in Fig. 4.3(b). Next the narrow sheet of foil is replaced by several rectangular conductors, as shown in Fig. 4.3(c). Then the rectangular conductors are replaced with square conductors depicted in Fig. 4.3(d). Finally, square conductors are replaced by round conductors

depicted in Fig. 4.3(e).

The procedure for transforming a rectangular winding conductor is as follows. Consider two foil windings with a single turn per layer. Both the foil windings have the same length l_w and thickness h. However, the widths and the resistivities of the foils are different. The wider foil has a width (or the winding breadth) b_{wf} and resistivity ρ_{wf}. The narrower foil has a width $b_w < b_{wf}$ and resistivity $\rho_w < \rho_{wf}$. Consequently, the narrow conductor skin depth δ_w is lower than the wide conductor skin depth δ_{wf}, i.e., $\delta_w < \delta_{wf}$. The resistivities are such that the dc resistances of both windings remain the same. The DC resistance of the foil winding is given by

$$R_{dcf} = \frac{\rho_{wf} l_w}{h b_{wf}} \tag{4.7}$$

and the dc resistance of the narrow foil winding is

$$R_{dc} = \frac{\rho_w l_w}{h b_w}. \tag{4.8}$$

The skin depth of the foil winding is given by

$$\delta_{wf} = \sqrt{\frac{\rho_{wf}}{\pi f_s \mu}} \tag{4.9}$$

and the skin depth of the narrow foil winding is

$$\delta_w = \sqrt{\frac{\rho_w}{\pi f_s \mu}}. \tag{4.10}$$

The narrow foil is cut into rectangular conductors of width w and stretched so that each layer has N_{tl} turns. The width of each conductor is

$$w = \frac{b_w}{N_{tl}} \tag{4.11}$$

and the distance between the centers of two adjacent conductors, called the winding pitch, is defined by

$$p = \frac{b_{wf}}{N_{tl}}. \tag{4.12}$$

As mentioned, the DC resistances of both the narrower and wider foils are the same $R_{dc} = R_{dcf}$

$$\frac{\rho_w l_w}{h b_w} = \frac{\rho_{wf} l_w}{h b_{wf}},\tag{4.13}$$

which gives the ratio of two resistivities

$$\frac{\rho_w}{\rho_{wf}} = \frac{b_w}{b_{wf}} = \frac{w N_{tl}}{p N_{tl}} = \frac{w}{p} = \eta_p,\tag{4.14}$$

where the layer *porosity factor*, *spacing factor*, or *fill factor* is defined as

$$\eta_p = \frac{w}{p}.\tag{4.15}$$

Using (4.9), (4.10), and (4.14), the ratio of the skin depths is given by

$$\frac{\delta_w}{\delta_{wf}} = \sqrt{\frac{\rho_w}{\rho_{wf}}} = \sqrt{\frac{w}{p}} = \sqrt{\eta_p}.\tag{4.16}$$

For a rectangular winding conductor, A is given by

$$A = A_r = \frac{h}{\delta_{wf}} = \frac{h}{\delta_w}\sqrt{\frac{h}{p}} = \frac{h}{\delta_w}\sqrt{\eta_p}.\tag{4.17}$$

For a square wire winding, $w = h$. Hence, (4.17) becomes

$$A = A_s = \frac{h}{\delta_w}\sqrt{\frac{w}{p}} = \frac{h}{\delta_w}\sqrt{\frac{h}{p}} = \frac{h}{\delta_w}\sqrt{\eta_p}.\tag{4.18}$$

The cross-sectional area of the square wire is

$$S_s = h^2\tag{4.19}$$

and the cross-sectional area of the round wire is

$$S_o = \pi\left(\frac{d}{2}\right)^2.\tag{4.20}$$

Equating (4.19) and (4.20) leads to

$$h^2 = \pi\left(\frac{d}{2}\right)^2.\tag{4.21}$$

Yielding the relationship between h and the effective round wire diameter d

$$d = \frac{2h}{\sqrt{\pi}} \approx 1.128h \tag{4.22}$$

from which the effective square conductor height is

$$h = \frac{d\sqrt{\pi}}{2} \approx 0.8662d. \tag{4.23}$$

Note that if the square and round wire areas are the same, the DC resistances of both the windings are the same. Substitution of (4.23) into (4.18) yields

$$A = A_o = \frac{h}{\delta_w}\sqrt{\frac{h}{p}} = \left(\frac{\pi}{4}\right)^{\frac{3}{4}} \frac{d^{\frac{3}{2}}}{\delta_w p^{\frac{1}{2}}} = \left(\frac{\pi}{4}\right)^{\frac{3}{4}} \frac{d}{\delta_w}\sqrt{\frac{d}{p}} = \left(\frac{\pi}{4}\right)^{\frac{3}{4}} \frac{d}{\delta_w}\sqrt{\eta_p}. \tag{4.24}$$

4.4 General Expression for Winding Power Loss in High-Frequency Transformer

In isolated PWM DC-DC converters, the transformer winding current i_L contains a DC component, a fundamental component, and many harmonics. If we know the DC component and the amplitudes or rms values of the of the winding current along with the winding DC and ac resistances due to skin and proximity effects at the frequencies of harmonics nf_s (where n is the harmonic number and f_s is the converter switching frequency), the winding power loss for each harmonic and the total winding power loss can be determined. The transformer winding current waveform can be expanded into a Fourier series

$$i_L = I_L + \sum_{n=1}^{\infty} I_{mn} \cos\left(n\omega t + \phi_n\right)$$

$$= I_L + \sqrt{2}\sum_{n=1}^{\infty} I_n \cos\left(n\omega t + \phi_n\right), \tag{4.25}$$

where I_L is the DC component of the winding current, I_{mn} is the amplitude of the nth harmonic, and $I_n = I_{mn}/\sqrt{2}$ is the rms value of the nth harmonic of the winding current.

4.4.1 Transformer Harmonic Winding Power Loss

The total winding power loss due to the DC current and all harmonics of the winding current is

$$
\begin{aligned}
P_w &= R_{wdc}I_L^2 + \sum_{n=1}^{\infty} R_{wn}I_n^2 \\
&= R_{wdc}I_L^2 + R_{w1}I_1^2 + R_{w2}I_2^2 + R_{w3}I_3^2 + \text{........} \\
&= R_{wdc}I_L^2 \left[1 + \left(\frac{R_{w1}}{R_{wdc}}\right)\left(\frac{I_1}{I_L}\right)^2 + \left(\frac{R_{w2}}{R_{wdc}}\right)\left(\frac{I_2}{I_L}\right)^2 + \left(\frac{R_{w3}}{R_{wdc}}\right)\left(\frac{I_3}{I_L}\right)^2 + \text{.......} \right] \\
&= R_{wdc}I_L^2 \left[1 + \sum_{n=1}^{\infty} \left(\frac{R_{wn}}{R_{wdc}}\right)\left(\frac{I_n}{I_L}\right)^2 \right] = R_{wdc}I_L^2 \left[1 + \sum_{n=1}^{\infty} F_{Rn}\left(\frac{I_n}{I_L}\right)^2 \right] \\
&= F_{Rh}P_{wdc}, \quad\quad\quad\quad\quad\quad\quad\quad\quad\quad\quad\quad\quad\quad (4.26)
\end{aligned}
$$

where R_{wdc} is the winding DC resistance and R_{w1}, R_{w2}, R_{w3}, ..., R_{wn} are the winding resistances at frequencies f_1, f_2, f_3, ..., f_n, respectively. The DC power loss in a winding is $P_{wdc} = R_{wdc}I_L^2$. The *ac resistance factor* at the fundamental frequency or the nth harmonic is given by

$$
F_{Rn} = \frac{R_{wn}}{R_{wdc}} = F_S + F_P
$$

$$
= A\sqrt{n} \left\{ \frac{\sinh(2A\sqrt{n}) + \sin(2A\sqrt{n})}{\cosh(2A\sqrt{n}) - \cos(2A\sqrt{n})} + \left[\frac{2(N_l^2 - 1)}{3}\right] \frac{\sinh(A\sqrt{n}) - \sin(A\sqrt{n})}{\cosh(A\sqrt{n}) + \cos(A\sqrt{n})} \right\},
$$
$$
(4.27)
$$

where N_l is the number of layers of the winding and A is the winding conductor thickness normalized to conductor skin depth at the fundamental frequency equal to the switching frequency f_s. The factor F_{Rn} takes into account both the *skin* and *proximity effects* in the winding. The equation for F_{Rn} is obtained by Dowell's one-dimensional solution for multilayer foil windings given by (4.4) and is extended to rectangular, square, and round conductors using (4.17), (4.18), (4.24), respectively.

4.4.2 Harmonic Winding Power Loss Factor F_{Rh}

The *harmonic winding power loss factor* is defined as the total winding DC and ac power loss (of all harmonics) normalized with respect to the winding DC power loss given by

$$F_{Rh} = \frac{P_w}{P_{wdc}} = 1 + \sum_{n=1}^{\infty} F_{Rn} \left(\frac{I_n}{I_L}\right)^2.$$
(4.28)

The ratio of I_n to I_L is waveform dependent which can be obtained using Fourier analysis applied to a specific current waveform. The factor F_{Rh} also depends upon the number of harmonics n, the normalized winding conductor thickness A, and the number of layers of the winding N_l.

4.5 Transformer Winding Loss for Flyback DC-DC Converter in CCM

In transformers used in isolated PWM DC-DC power converters in CCM, the current waveforms of the primary and secondary windings are pulsating. Therefore, the amplitudes of the harmonics are high, causing high losses. This situation is different in nonisolated PWM converters in CCM because the current waveform of the inductor is nearly constant and the amplitudes of harmonics are low.

4.5.1 Primary Winding Power Loss for CCM

Assume that the primary winding current for CCM is a rectangular wave with a duty ratio D as shown in Fig. 4.4(a). The primary winding current is given by

$$i_p = \left\{ \begin{array}{ll} I_{pmax}, & \text{for} \qquad 0 < t \leq DT \\ 0, & \text{for} \qquad DT < t \leq T \end{array} \right\}.$$
(4.29)

The Fourier series of the current waveform of the primary winding is

$$i_p = I_{pdc} \left[1 + 2 \sum_{n=1}^{\infty} \frac{\sin(n\pi D)}{n\pi D} \cos(n\omega_s t) \right].$$
(4.30)

The power loss in the primary winding for CCM is

$$P_{wp} = P_{wpdc} \left\{ 1 + 2 \sum_{n=1}^{\infty} F_{Rpn} \left[\frac{\sin(n\pi D)}{n\pi D} \right]^2 \right\} = P_{wpdc} F_{Rph},$$
(4.31)
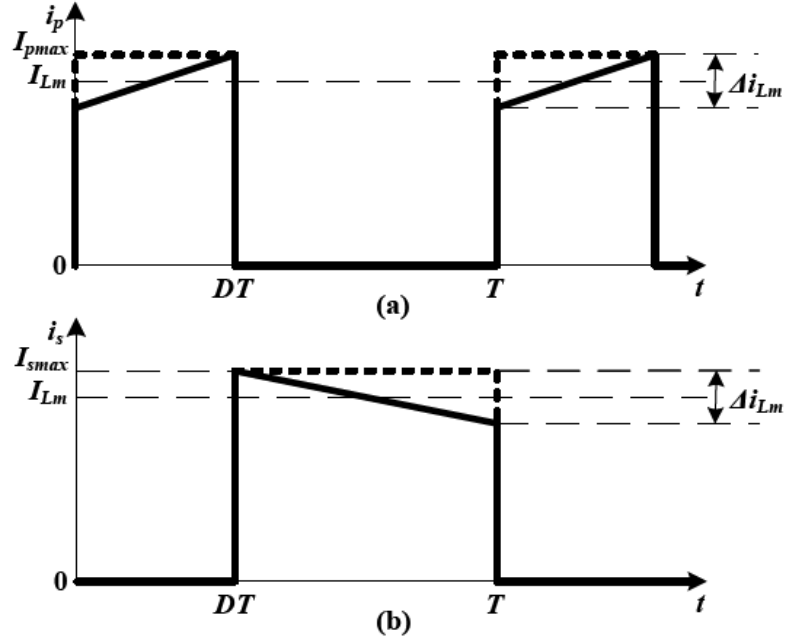
Figure 4.4: Two-winding flyback transformer current waveforms for CCM. (a) Primary current i_p. (b) Secondary current i_s.

where $P_{wpdc} = R_{wpdc}I_{pdc}^2$ and the normalized primary winding resistance at the fundamental frequency and harmonic frequencies are

$$F_{Rpn} = \frac{R_{wpn}}{R_{wpdc}} = F_S + F_P$$

$$= A\sqrt{n} \left\{ \frac{\sinh(2A\sqrt{n}) + \sin(2A\sqrt{n})}{\cosh(2A\sqrt{n}) - \cos(2A\sqrt{n})} + \left[\frac{2(N_l^2 - 1)}{3} \right] \frac{\sinh(A\sqrt{n}) - \sin(A\sqrt{n})}{\cosh(A\sqrt{n}) + \cos(A\sqrt{n})} \right\}.$$

$$(4.32)$$

The primary winding ac power loss normalized with respect to the primary winding DC power loss is

$$F_{Rph} = \frac{P_{wp}}{P_{wpdc}} = 1 + 2\sum_{n=1}^{\infty} F_{Rpn} \left[\frac{\sin(n\pi D)}{n\pi D} \right]^2.$$

$$(4.33)$$

4.5.2 Secondary Winding Power Loss for CCM

Assume that the secondary winding current for CCM is a rectangular wave as shown in Fig. 4.4(b). The secondary winding current is given by

$$i_s = \left\{ \begin{array}{lll} I_{smax}, & \text{for} & (1-D)T < t \le T \\ 0, & \text{for} & 0 < t \le DT \end{array} \right\}. \tag{4.34}$$

The Fourier series of the current waveform of the secondary winding is

$$i_s = I_{sdc} \left\{ 1 + 2 \sum_{n=1}^{\infty} \frac{\sin\left[n\pi(1-D)\right]}{n\pi(1-D)} \cos\left(n\omega_s t\right) \right\}. \tag{4.35}$$

The power loss in the secondary winding for CCM is

$$P_{ws} = P_{wsdc} \left\langle 1 + 2 \sum_{n=1}^{\infty} F_{Rsn} \left\{ \frac{\sin\left[n\pi(1-D)\right]}{n\pi(1-D)} \right\}^2 \right\rangle = P_{wsdc} F_{Rsh}, \tag{4.36}$$

where $P_{wsdc} = R_{wsdc} I_{sdc}^2$. The secondary winding ac power loss normalized with respect to the secondary winding DC power loss is

$$F_{Rsh} = \frac{P_{ws}}{P_{wsdc}} = 1 + 2 \sum_{n=1}^{\infty} F_{Rsn} \left\{ \frac{\sin\left[n\pi(1-D)\right]}{n\pi(1-D)} \right\}^2 \tag{4.37}$$

In (4.37), $F_{Rsn} = F_{Rpn}$ can be computed using (4.32) and using (4.17), (4.18), and (4.24) for rectangular, square or round secondary winding wire, respectively.

4.6 Transformer Winding Loss for Flyback DC-DC Converter in DCM

4.6.1 Primary Winding Power Loss for DCM

The current waveform of the primary winding for DCM is shown in Fig. 4.5(a) and is given by

$$i_p = \left\{ \begin{array}{lll} \frac{I_{pmax}}{DT} t, & \text{for} & 0 < t \le DT \\ 0, & \text{for} & DT < t \le T \end{array} \right\}. \tag{4.38}$$

The DC component of the primary winding current for DCM is

$$I_{pdc} = \frac{1}{T} \int_0^T i_p \, dt = \frac{I_{pmax}}{DT^2} \int_0^{DT} t \, dt = \frac{DI_{pmax}}{2}. \tag{4.39}$$
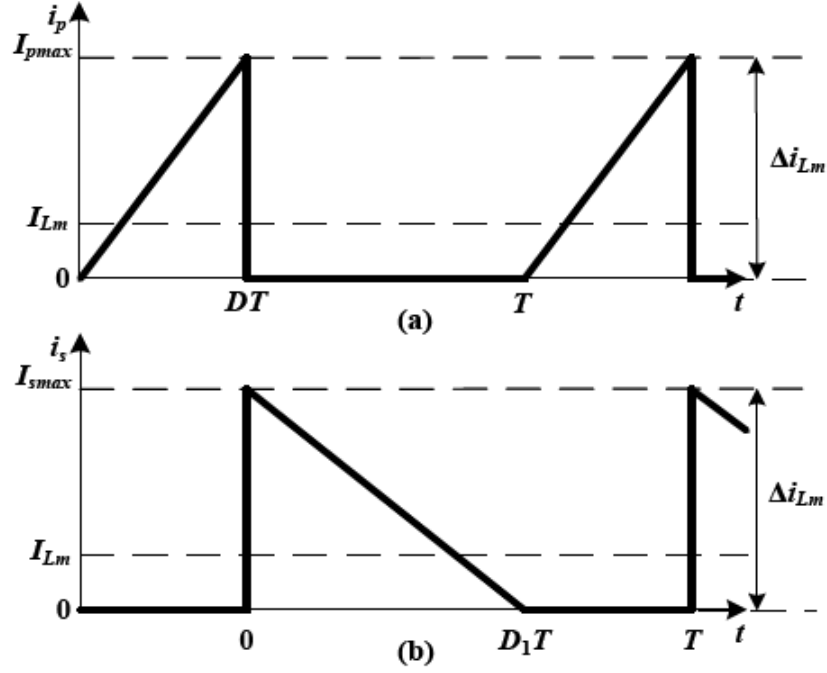
Figure 4.5: Two-winding flyback transformer current waveforms for DCM. (a) Primary current i_p. (b) Secondary current i_s.

The Fourier series coefficients are

$$a_n = \frac{2}{T} \int_0^T i_p \cos(n\omega t) \ dt = \frac{2I_{pmax}}{DT^2} \int_0^{DT} t \cos(n\omega t) \ dt$$

$$= \frac{I_{pmax}}{2\pi^2 n^2 D^2} \left[\cos(2\pi nD) - 1 + 2\pi nD \sin(2\pi nD)\right]. \tag{4.40}$$

and

$$b_n = \frac{2}{T} \int_0^T i_p \sin(n\omega t) \ dt = \frac{2I_{pmax}}{DT^2} \int_0^{DT} t \sin(n\omega t) \ dt$$

$$= \frac{I_{pmax}}{2\pi^2 n^2 D^2} \left[\sin(2\pi nD) - 2\pi nD \cos(2\pi nD)\right]. \tag{4.41}$$

which gives the amplitudes of the fundamental component and the harmonics of the primary winding current as

$$I_{pn} = \sqrt{a_n^2 + b_n^2} = \frac{I_{pmax}}{2\pi^2 n^2 D} \sqrt{2\left[1 + 2\pi^2 n^2 D^2 - 2\pi n \sin(2\pi nD) - \cos(2\pi nD)\right]}$$

$$= \frac{I_{pdc}}{\pi^2 n^2 D^2} \sqrt{2\left[1 + 2\pi^2 n^2 D^2 - 2\pi n \sin(2\pi nD) - \cos(2\pi nD)\right]}. \tag{4.42}$$

The power loss in the primary winding is

$$P_{wp} = R_{wpdc}I_{pdc}^2 \left[1 + \frac{1}{2} \sum_{n=1}^{\infty} \left(\frac{R_{wpn}}{R_{wpdc}} \right) \left(\frac{I_{pn}}{I_{pdc}} \right)^2 \right] = P_{wpdc} \left[1 + \frac{1}{2} \sum_{n=1}^{\infty} F_{Rpn} \left(\frac{I_{pn}}{I_{pdc}} \right)^2 \right]$$

$$= P_{wpdc} \left\{ 1 + \frac{1}{\pi^4 D^4} \sum_{n=1}^{\infty} \frac{F_{Rpn}}{n^4} \left[1 + 2\pi^2 n^2 D^2 - \cos\left(2\pi nD\right) - 2\pi nD \sin\left(2\pi nD\right) \right] \right\}$$

$$= P_{wpdc} F_{Rph}. \tag{4.43}$$

The primary winding ac power loss normalized with respect to the primary winding DC power loss is

$$F_{Rph} = \frac{P_{wp}}{P_{wpdc}} = 1 + \frac{1}{2} \sum_{n=1}^{\infty} F_{Rpn} \left(\frac{I_{pn}}{I_{pdc}} \right)^2$$

$$= 1 + \frac{1}{\pi^4 D^4} \sum_{n=1}^{\infty} \frac{F_{Rpn}}{n^4} \left[1 + 2\pi^2 n^2 D^2 - \cos\left(2\pi nD\right) - 2\pi nD \sin\left(2\pi nD\right) \right]. \tag{4.44}$$

4.6.2 Secondary Winding Power Loss for DCM

The current waveform of the secondary winding for DCM is shown in Fig. 4.5(b) and is given by

$$i_s = \left\{ \begin{array}{lll} -\frac{I_{smax}}{D_1 T} t + I_{smax}, & \text{for} & 0 < t \le D_1 T \\ 0, & \text{for} & D_1 T < t \le T \end{array} \right\}. \tag{4.45}$$

The DC component of the secondary winding current for DCM is

$$I_{sdc} = \frac{1}{T} \int_0^T i_s \, dt = \frac{I_{smax}}{T} \int_0^{D_1 T} \left(1 - \frac{t}{D_1 T} \right) \, dt = \frac{D I_{smax}}{2}. \tag{4.46}$$

The Fourier series coefficients are

$$a_n = \frac{2}{T} \int_0^T i_s \cos\left(n\omega t\right) \, dt = \frac{2 I_{smax}}{T} \int_0^{D_1 T} \left(1 - \frac{t}{D_1 T} \right) \cos\left(n\omega t\right) \, dt$$

$$= \frac{I_{smax}}{2\pi^2 n^2 D^2} \left[1 - \cos\left(2\pi nD_1\right) \right]. \tag{4.47}$$

and

$$b_n = \frac{2}{T} \int_0^T i_s \sin\left(n\omega t\right) \, dt = \frac{2 I_{smax}}{T} \int_0^{D_1 T} \left(1 - \frac{t}{D_1 T} \right) \sin\left(n\omega t\right) \, dt$$

$$= \frac{I_{smax}}{2\pi^2 n^2 D_1} \left[2\pi nD_1 - \sin\left(2\pi nD_1\right) \right]. \tag{4.48}$$

yielding the amplitudes of the fundamental component and the harmonics of the secondary winding current as

$$I_{sn} = \sqrt{a_n^2 + b_n^2} = \frac{I_{smax}}{2\pi^2 n^2 D_1} \sqrt{2\left\{1 - \cos\left(2\pi n D_1\right) + 2\pi n D_1\left[\pi n D_1 - \sin\left(2\pi n D_1\right)\right]\right\}}$$

$$= \frac{I_{sdc}}{\pi^2 n^2 D_1^2} \sqrt{2\left\{1 - \cos\left(2\pi n D_1\right) + 2\pi n D_1\left[\pi n D_1 - \sin\left(2\pi n D_1\right)\right]\right\}}. \qquad (4.49)$$

The power loss in the secondary winding is

$$P_{ws} = R_{wsdc}I_{sdc}^2\left[1 + \frac{1}{2}\sum_{n=1}^{\infty}\left(\frac{R_{wsn}}{R_{wsdc}}\right)\left(\frac{I_{sn}}{I_{sdc}}\right)^2\right] = P_{wsdc}\left[1 + \frac{1}{2}\sum_{n=1}^{\infty}F_{Rsn}\left(\frac{I_{sn}}{I_{sdc}}\right)^2\right]$$

$$= P_{wsdc}\left\langle 1 + \frac{1}{\pi^4 D_1^4}\sum_{n=1}^{\infty}\frac{F_{Rsn}}{n^4}\left\{1 - \cos\left(2\pi n D_1\right) + 2\pi n D_1\left[\pi n D_1 - \sin\left(2\pi n D_1\right)\right]\right\}\right\rangle$$

$$= P_{wsdc}F_{Rsh}. \qquad (4.50)$$

The relationship between D and D_1 is converter dependent. The secondary winding ac power loss normalized with respect to the secondary winding DC power loss is

$$F_{Rsh} = \frac{P_{ws}}{P_{wsdc}} = 1 + \frac{1}{2}\sum_{n=1}^{\infty}F_{Rsn}\left(\frac{I_{sn}}{I_{sdc}}\right)^2$$

$$= 1 + \frac{1}{\pi^4 D_1^4}\sum_{n=1}^{\infty}\frac{F_{Rsn}}{n^4}\left\{1 - \cos\left(2\pi n D_1\right) + 2\pi n D_1\left[\pi n D_1 - \sin\left(2\pi n D_1\right)\right]\right\}. \qquad (4.51)$$

5 Design of High-Frequency Flyback Transformer

5.1 Background

The transformer in a flyback converter is the most important component of the converter. It provides DC isolation, ac coupling, and voltage or current level change. Additionally, the flyback transformer also stores magnetic energy required for power conversion. In this chapter, the derivation of core area product A_p for transformers subject to square wave voltages is presented. Step-by-step procedures to design a high-frequency two-winding transformer for off-line flyback converter for both CCM and DCM cases are given.

5.2 Area Product Method

The magnetic flux linkage λ due to magnetic flux ϕ linking N_p turns of the primary winding of the transformer is given by

$$\lambda = N_p\phi = N_p A_c B = L_p i_p, \tag{5.1}$$

where A_c is the core cross-sectional area in m^2 and B is the magnetic flux density in T. For the peak values, this equation becomes

$$\lambda_{pk} = N_p\phi_{pk} = N_p A_c B_{pk} = L_p I_{pmax}. \tag{5.2}$$

The maximum current density of the primary winding wire is

$$J_m = \frac{I_{pmax}}{A_{wp}}, \tag{5.3}$$

where A_{wp} is the primary winding bare wire cross-sectional area in m^2. The core window area limited by the maximum current density in the winding wire is given by

$$W_a = \frac{N_p A_{wp} + N_s A_{ws}}{K_u}, \tag{5.4}$$

where N_s is the number of turns of the secondary winding and A_{ws} is the secondary winding bare wire cross-sectional area in m^2. Assuming the winding allocation is such that $N_p A_{wp} = N_s A_{ws}$, the window area is

$$W_a = \frac{2 N_p A_{wp}}{K_u},$$ (5.5)

where the window utilization factor is defined as

$$K_u = \frac{A_{Cu}}{W_a} = \frac{2 N_p A_{wp}}{W_a},$$ (5.6)

where A_{Cu} is the total copper area in the window in m^2. The maximum energy stored in the magnetic field of the transformer is

$$W_m = \frac{1}{2} L_m I_{Lm(\text{max})}^2,$$ (5.7)

where L_m and I_{Lm} are the transformer magnetizing inductance and magnetizing current, respectively. Assuming that $L_p \approx L_m$ and $I_{pmax} \approx I_{Lm(\text{max})}$ (where L_p and I_p are the transformer primary inductance and primary peak current, respectively), and using (5.2), (5.3), and (5.5), the *area product* of the core is defined as

$$A_p = W_a A_c = \frac{2 L_p I_{pmax}^2}{K_u J_m B_{pk}} = \frac{4 W_m}{K_u J_m B_{pk}}.$$ (5.8)

The transformer core area product gives a measure of energy handling capability of a core and can be used to select a suitable core for a specific application using the manufacturer's datasheets. The value of A_p can be decreased by increasing the values of K_u, J_m, and $B_{pk} < B_s$, where B_s is the core saturation flux density.

5.3 Design of Flyback Transformer for CCM

The following specifications are given for the flyback PWM DC-DC converter for CCM operation:

- Input DC voltage range: $V_{Imin} \le V_I \le V_{Imax}$ (V)

- Output DC voltage: V_O (V)

- Output current range: $I_{Omin} \leq I_O \leq I_{Omax}$ (A)

- Switching frequency: f_s (kHz)

The steps to design a two-winding flyback transformer for CCM operation are as follows. The maximum and minimum output power are

$$P_{Omax} = V_O I_{Omax} \text{ (W)} \tag{5.9}$$

and

$$P_{Omin} = V_O I_{Omin} \text{ (W)}. \tag{5.10}$$

The minimum and maximum load resistances are

$$R_{Lmin} = \frac{V_O}{I_{Omax}} \text{ } (\Omega) \tag{5.11}$$

and

$$R_{Lmax} = \frac{V_O}{I_{Omin}} \text{ } (\Omega). \tag{5.12}$$

The minimum and maximum DC voltage transfer functions are

$$M_{VDCmin} = \frac{V_O}{V_{Imax}} \tag{5.13}$$

and

$$M_{VDCmax} = \frac{V_O}{V_{Imin}}. \tag{5.14}$$

The transformer primary-to-secondary turns ratio is

$$n_T = \frac{\eta_{conv} D_{max}}{(1 - D_{max}) M_{VDCmax}}. \tag{5.15}$$

In (5.15), the values of converter efficiency η_{conv} and maximum duty cycle D_{max} are obtained from the converter specifications. The minimum duty cycle is

$$D_{min} = \frac{n_T M_{VDCmin}}{n_T M_{VDCmin} + \eta_{conv}}. \tag{5.16}$$

The minimum magnetizing inductance required for CCM operation of the converter is

$$L_{pmin} \approx L_{m(min)} = \frac{n_T^2 R_{Lmax}(1 - D_{min})^2}{2f_s} \; (\mu\text{H}). \tag{5.17}$$

Pick $L_p > L_{pmin}$. The inductance of the secondary winding is

$$L_s = \frac{L_p}{n_T^2} \; (\mu\text{H}). \tag{5.18}$$

The maximum peak-to-peak value of the magnetizing current and the primary current ripple is

$$\Delta i_{Lp(max)} = \Delta i_{Lm(max)} = \frac{n_T V_O(1 - D_{min})}{f_s L_p} \; (\text{A}). \tag{5.19}$$

The minimum peak-to-peak value of the magnetizing current and the primary current ripple is

$$\Delta i_{Lp(min)} = \Delta i_{Lm(min)} = \frac{n_T V_O(1 - D_{max})}{f_s L_p} \; (\text{A}). \tag{5.20}$$

The maximum DC input current is

$$I_{Imax} = \frac{M_{VDCmax} I_{Omax}}{\eta_{conv}} \; (\text{A}). \tag{5.21}$$

The maximum peak value of the primary winding current is

$$I_{pmax} = \frac{I_{Omax}}{n_T(1 - D_{max})} + \frac{\Delta i_{Lp(max)}}{2} \; (\text{A}). \tag{5.22}$$

The maximum rms value of the primary winding current is

$$I_{prms(max)} = \frac{I_{Omax}\sqrt{D_{max}}}{n_T(1 - D_{max})} \; (\text{A}). \tag{5.23}$$

The maximum energy stored in the magnetic field of the transformer is

$$W_m = \frac{1}{2}L_m I_{Lm(max)}^2 = \frac{1}{2}L_p I_{Lpmax}^2 \; (\text{mJ}). \tag{5.24}$$

Using (5.8) and (5.24), the core area product is

$$A_p = W_a A_c = \frac{2L_p I_{pmax}^2}{K_u J_m B_{pk}} = \frac{4W_m}{K_u J_m B_{pk}} \; (\text{cm}^4). \tag{5.25}$$

Since the saturation flux density B_s decreases as the temperature increases, the high temperature B-H characteristics should be considered in the design. The typical range of values of the saturation flux density for ferrites at high temperatures is $B_s = 0.3$ to 0.35 T. The typical values of the core window utilization factor K_u for inductors and transformers are 0.3 and 0.4, respectively. The typical value of K_u for a toroidal core is 0.25. The typical range of the maximum value of the current density J_m for power converter applications is 0.1 to 5 A/mm^2. In calculating A_p using (5.25), the typical values of K_u, J_m, and B_{pk} are assumed. Using the core manufacturer's datasheets, a specific core whose A_p is very close to the value calculated in (5.25) is chosen and the following details of the core are obtained:

- Selected core: Core Number

- Core area product: A_p (cm^4)

- Core cross-sectional area: A_c (cm^2)

- Core window area: $W_a = A_p/A_c$ (cm^2)

- Mean magnetic path length (MPL): l_c (cm)

- Mean length of single turn (MLT): l_T (cm)

- Core volume: V_c (cm^3)

- Core surface area: A_t (cm^2)

- Core permeability: μ_{rc}

- Core saturation flux density: B_s (T)

- Core power loss density coefficients: k, a, b

The skin depth of copper wire is

$$\delta_w = \sqrt{\frac{\rho_{Cu(20°C)}}{\pi f_s \mu_0}} \ (\text{mm}),$$

(5.26)

where $\rho_{Cu(20°C)} = 1.72 \times 10^{-8}$ Ωm is the resistivity of copper at 20°C and $\mu_0 = 4\pi \times 10^{-7}$ H/m is the magnetic constant or the permeability of free space. To avoid skin effect, the winding wire is made up of multiple strands. The diameter of a bare strand is

$$d_{is} = 2\delta_w \ (\text{mm}).$$

(5.27)

Based on the bare strand diameter, a suitable AWG copper wire is chosen and the following details of the selected wire are obtained:

- Selected wire: Wire Number

- Diameter of the bare strand: d_{is} (mm)

- Diameter of the insulated strand: d_{os} (mm)

- Cross-sectional area of the bare strand: A_{wsi} (mm^2)

- Cross-sectional area of the insulated strand: A_{wso} (mm^2)

- DC resistance of the strand per unit length: R_{wdcs}/l_w (Ω/m)

The cross-sectional area of the primary winding wire is

$$A_{wp} = \frac{I_{pmax}}{J_m} \ (\text{mm}^2).$$

(5.28)

The number of strands in the primary winding wire is

$$S_p = \frac{A_{wp}}{A_{wsi}}.$$

(5.29)

The core window area allocated for the primary winding is

$$W_{ap} = \frac{W_a}{2} \ (\text{cm}^2).$$

(5.30)

The number of turns of the primary winding is

$$N_p = \frac{K_u W_{ap}}{S_p A_{wso}}. \tag{5.31}$$

The number of turns of the secondary winding is

$$N_s = \frac{N_p}{n_T}. \tag{5.32}$$

The length of the air gap is

$$l_g = \frac{\mu_0 A_c N_p^2}{L_p} - \frac{l_c}{\mu_{rc}} \quad \text{(mm)}. \tag{5.33}$$

The maximum peak value of the magnetic flux density is

$$B_{pk} = \frac{\mu_0 N_p I_{pmax}}{l_g + \frac{l_c}{\mu_{rc}}} \quad \text{(T)}. \tag{5.34}$$

The maximum peak value of the ac component of the flux density is

$$B_{m(max)} = \frac{\mu_0 N_p}{l_g + \frac{l_c}{\mu_{rc}}} \left[\frac{\Delta i_{Lp(max)}}{2}\right] \quad \text{(T)}. \tag{5.35}$$

The minimum peak value of the ac component of the flux density at full power is

$$B_{m(min)} = \frac{\mu_0 N_p}{l_g + \frac{l_c}{\mu_{rc}}} \left[\frac{\Delta i_{Lp(min)}}{2}\right] \quad \text{(T)}. \tag{5.36}$$

The core power loss density is

$$P_v = k(f_s \text{ in kHz})^a (10 B_m)^b \qquad \text{(mW/cm}^3). \tag{5.37}$$

The minimum core power loss density at full power is

$$P_{vmin} = k(f_s \text{ in kHz})^a (10 B_{m(min)})^b \qquad \text{(mW/cm}^3). \tag{5.38}$$

The core loss is

$$P_C = V_c P_v \quad \text{(mW)}. \tag{5.39}$$

The minimum core loss at full power is

$$P_{Cmin} = V_c P_{vmin} \quad \text{(mW)}. \tag{5.40}$$

The total length of the primary winding wire is

$$l_{wp} = N_p l_T \text{ (cm)}. \tag{5.41}$$

The DC and low-frequency resistance of each strand of the primary winding wire is

$$R_{wpdcs} = \left(\frac{R_{wdcs}}{l_w}\right) l_{wp} \text{ (Ω)}. \tag{5.42}$$

Hence, the DC and low-frequency resistance of the primary winding wire is

$$R_{wpdc} = \frac{R_{wpdcs}}{S_p} \text{ (Ω)}. \tag{5.43}$$

The DC and low-frequency power loss in the primary winding is

$$P_{wpdc} = R_{wpdc} I_{Imax}^2 \text{ (W)}. \tag{5.44}$$

Using (4.33), the harmonic primary winding loss factor F_{Rph} for CCM is calculated, from which, the primary winding power loss is obtained as

$$P_{wp} = F_{Rph} P_{wpdc} \text{ (W)}. \tag{5.45}$$

The maximum current through the secondary winding is

$$I_{smax} = \frac{I_{Omax}}{1 - D_{max}} + \frac{n \Delta i_{Lp(max)}}{2} \text{ (A)}. \tag{5.46}$$

The maximum rms value of the secondary winding current is

$$I_{srms(max)} = \frac{I_{Omax}}{\sqrt{1 - D_{max}}} \text{ (A)}. \tag{5.47}$$

The cross-sectional area of the secondary winding wire is

$$A_{ws} = \frac{I_{smax}}{J_m} \text{ (mm}^2). \tag{5.48}$$

The number of strands in the secondary winding wire is

$$S_s = \frac{A_{ws}}{A_{wsi}}. \tag{5.49}$$

The total length of the secondary winding wire is

$$l_{ws} = N_s l_T \text{ (cm)}. \tag{5.50}$$

The DC and low-frequency resistance of each strand of the secondary winding wire is

$$R_{wsdcs} = \left(\frac{R_{wdcs}}{l_w}\right) l_{ws} \text{ (Ω)}. \tag{5.51}$$

Hence, the DC and low-frequency resistance of the primary winding wire is

$$R_{wsdc} = \frac{R_{wsdcs}}{S_s} \text{ (Ω)}. \tag{5.52}$$

The DC and low-frequency power loss in the secondary winding is

$$P_{wsdc} = R_{wsdc} I_{Omax}^2 \text{ (W)}. \tag{5.53}$$

Using (4.37), the harmonic secondary winding loss factor F_{Rsh} for CCM is calculated, from which, the secondary winding power loss is obtained as

$$P_{ws} = F_{Rsh} P_{wsdc} \text{ (W)}. \tag{5.54}$$

The DC and low-frequency power loss in both primary and secondary windings is

$$P_{wdc} = P_{wpdc} + P_{wsdc} \text{ (W)}. \tag{5.55}$$

The total power loss in both primary and secondary windings is

$$P_w = P_{wp} + P_{ws} \text{ (W)}. \tag{5.56}$$

Sum of the core loss and the winding resistance loss in the transformer is

$$P_{cw} = P_C + P_w \text{ (W)}. \tag{5.57}$$

The efficiency of the transformer at full power is

$$\eta_t = \frac{P_O}{P_O + P_{cw}}. \tag{5.58}$$

The surface power loss density is

$$\psi = \frac{P_{cw}}{A_t} \ (\text{W/cm}^2).$$ (5.59)

The temperature rise of the transformer is

$$\Delta T = 450\psi^{0.826} \ (^\circ\text{C}).$$ (5.60)

The core window utilization factor recalculated is

$$K_u = \frac{(N_p S_p + N_s S_s) A_{wso}}{W_a}.$$ (5.61)

5.4 Characteristics of High-Frequency Flyback Transformer for CCM

The theory of winding losses due to harmonics will be illustrated by the case study of the transformer used in the flyback converter operating in CCM. The following specifications of the flyback converter are used: DC input voltage $V_I = 50 \pm 10$ V, DC output voltage $V_O = 24$ V, maximum output power $P_{O\text{max}} = 30$ W, minimum output power $P_{O\text{min}} = 5$ W, and switching frequency $f_s = 100$ kHz. Using (5.9) - (5.61) the parameters of the flyback transformer are calculated and listed in Tables 5.1 and 5.2.

In this section, the computed characteristics of the designed transformer are presented for a wide range of operating conditions of the flyback converter in CCM i.e., over the entire range of the load current and the DC input voltage. Plot of primary winding harmonic loss factor F_{Rph} as a function of input voltage is shown in Fig. 5.1, using (4.32), (4.24), and (4.33) for $N_l = 2$, $d/\delta_{w1} = 1.9378$, $d/p = 0.8$, and $n = 100$. Plot of secondary winding harmonic loss factor F_{Rsh} as a function of input voltage is shown in Fig. 5.2, using (4.32), (4.24), and (4.37) for $N_l = 2$, $d/\delta_{w1} = 1.9378$, $d/p = 0.8$, and $n = 100$. The values of F_{Rph} and F_{Rsh} were calculated with $n = 100$ for all
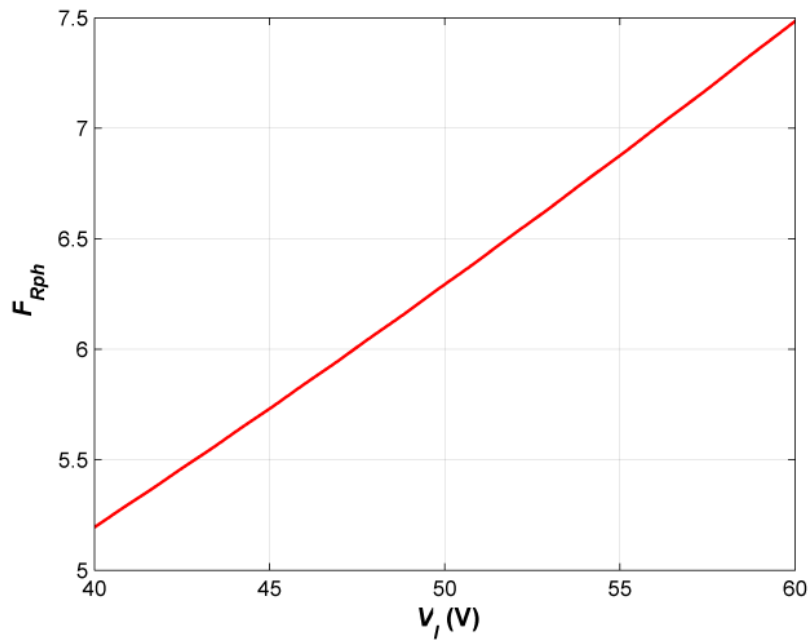
Figure 5.1: Primary winding harmonic loss factor F_{Rph} as a function of the DC input voltage V_I.
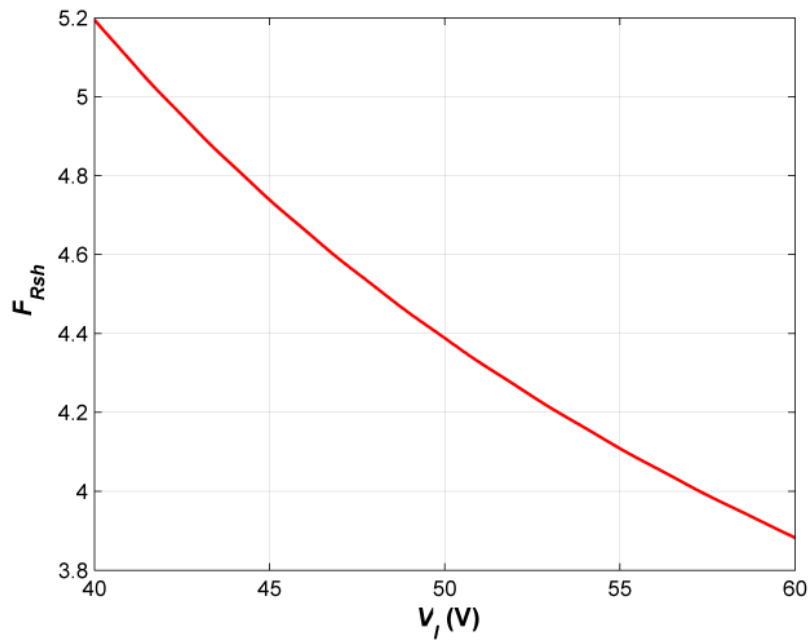
Figure 5.2: Secondary winding harmonic loss factor F_{Rsh} as a function of the DC input voltage V_I.
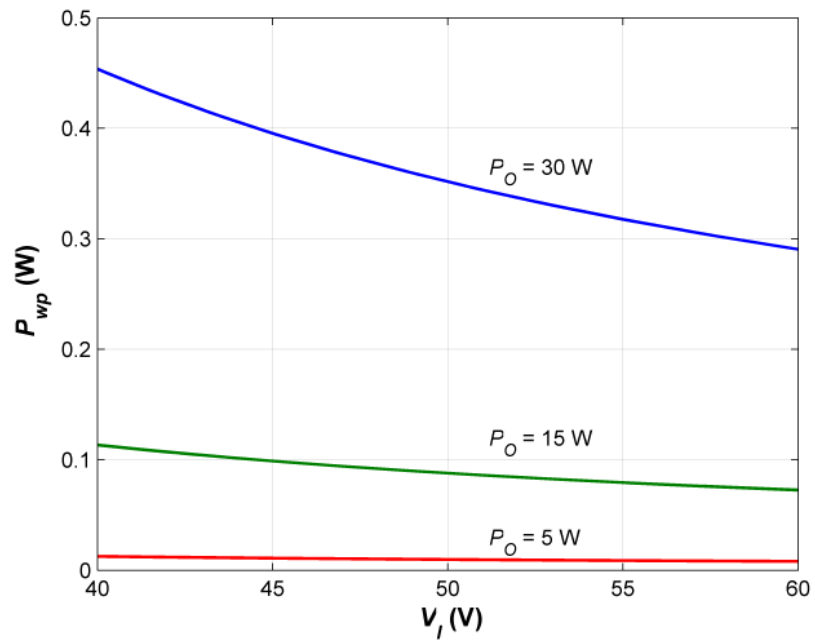
Figure 5.3: Primary winding loss P_{wp} as a function of the DC input voltage V_I at fixed values of the output power P_O.
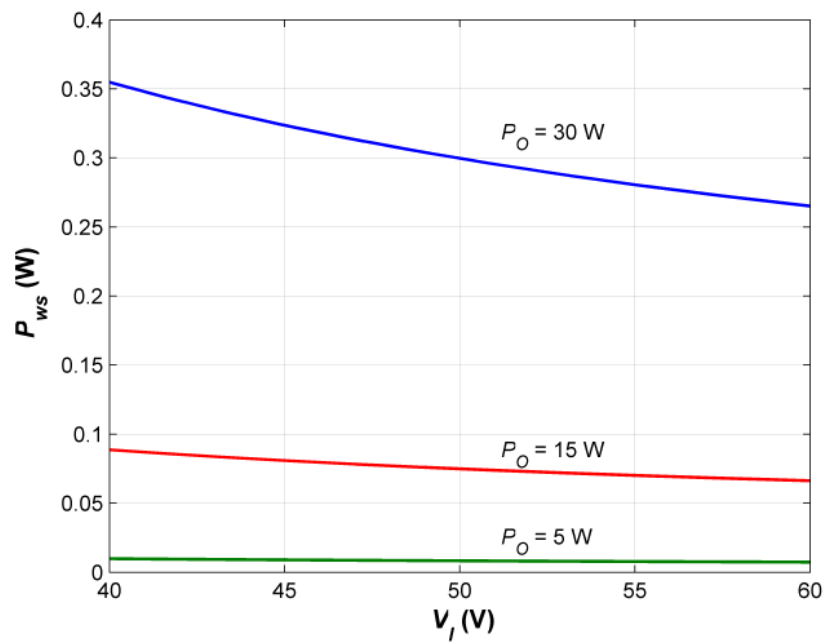
Figure 5.4: Secondary winding loss P_{ws} as a function of the DC input voltage V_I at fixed values of the output power P_O.
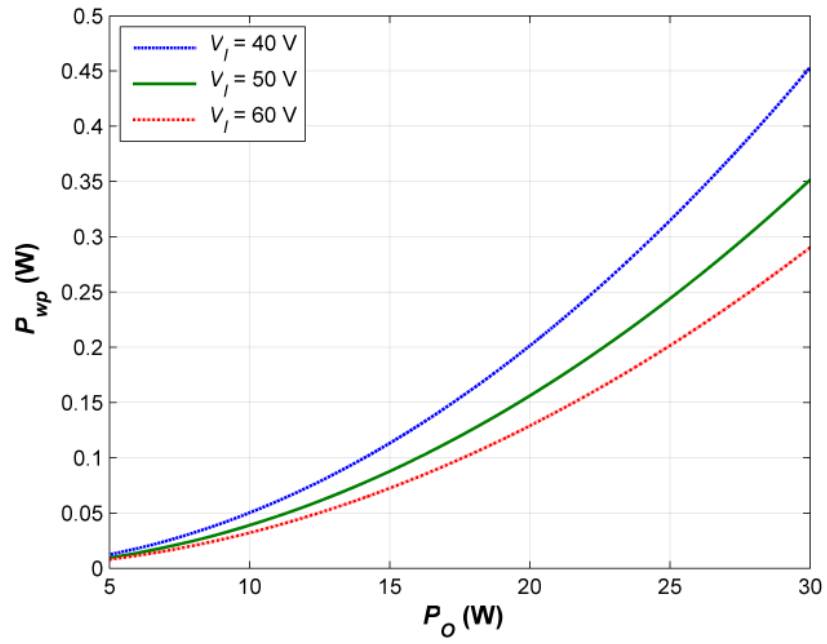
Figure 5.5: Primary winding loss P_{wp} as a function of the output power P_O at fixed values of the DC input voltage V_I.
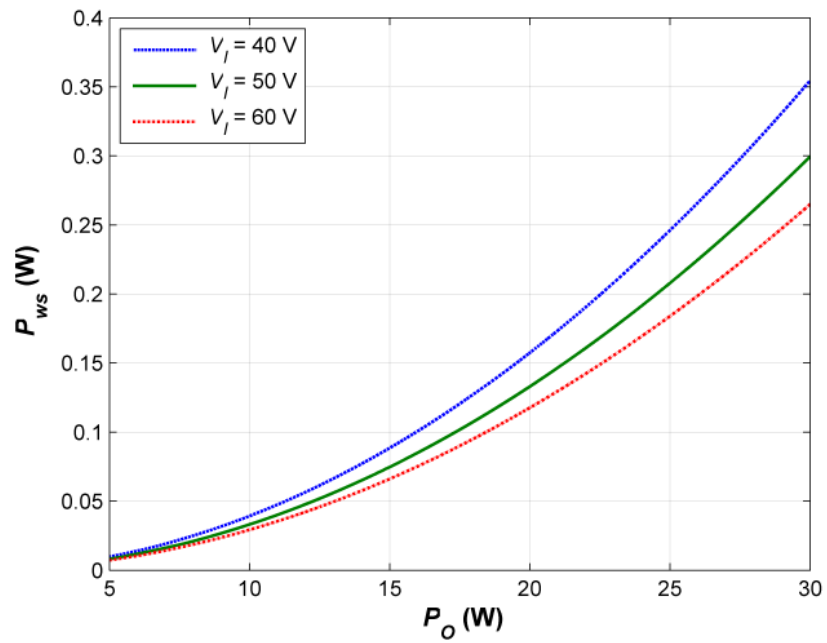
Figure 5.6: Secondary winding loss P_{ws} as a function of the output power P_O at fixed values of the DC input voltage V_I.
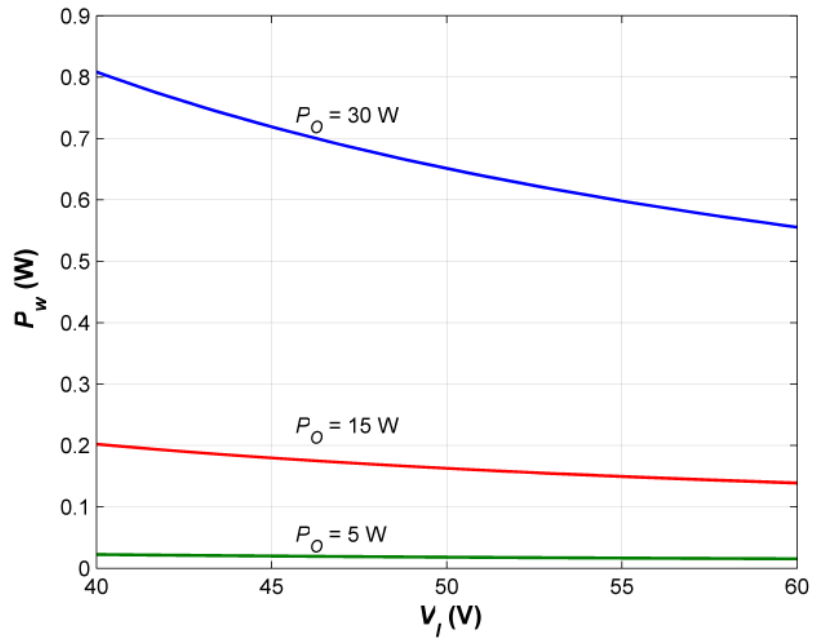
Figure 5.7: Primary and secondary winding loss P_w as a function of the DC input voltage V_I at fixed values of the output power P_O.
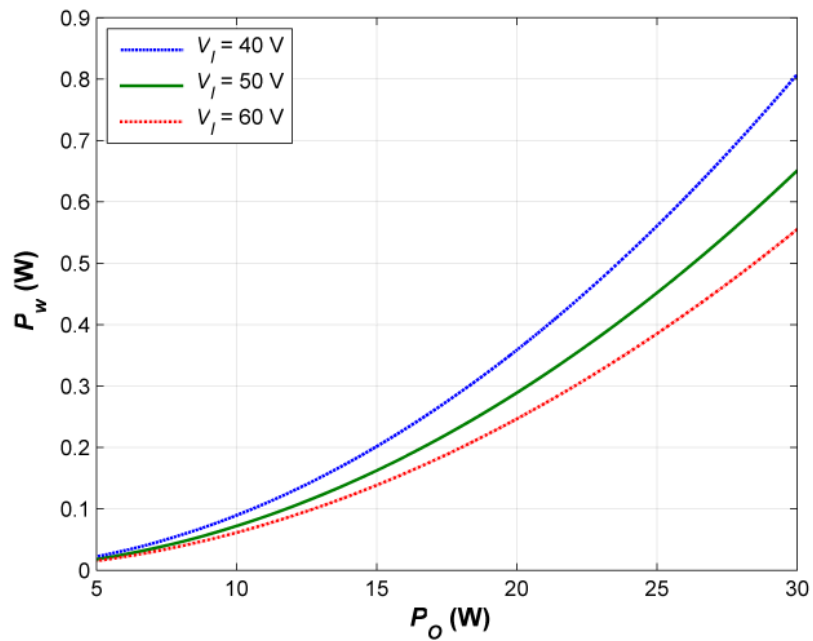
Figure 5.8: Primary and secondary winding loss P_w as a function of the output power P_O at fixed values of the DC input voltage V_I.
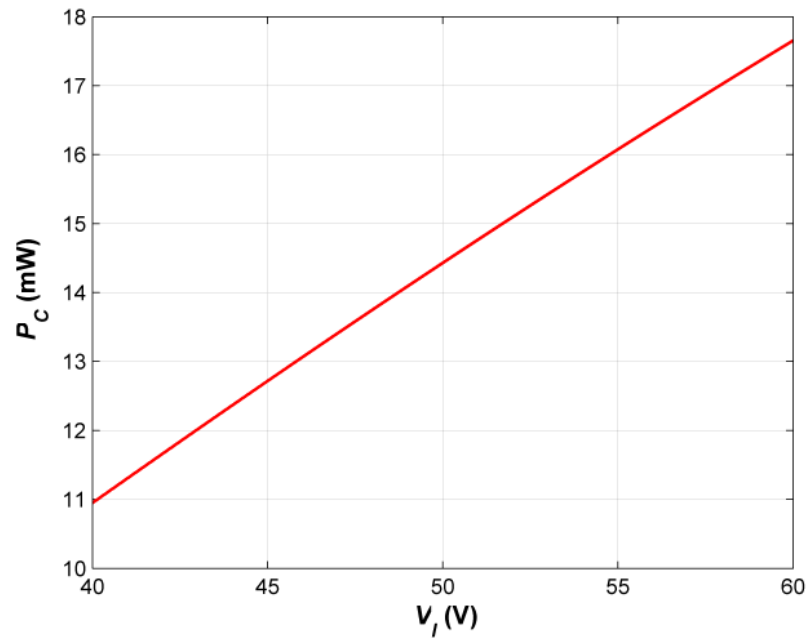
Figure 5.9: Core loss P_C as a function of the DC input voltage V_I.
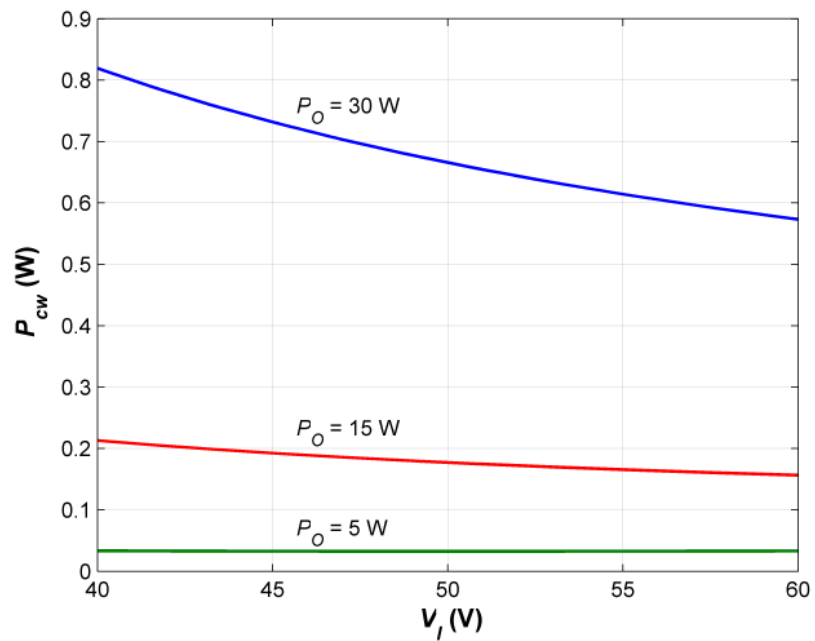
Figure 5.10: Total transformer power loss P_{cw} as a function of the DC input voltage V_I at fixed values of the output power P_O.
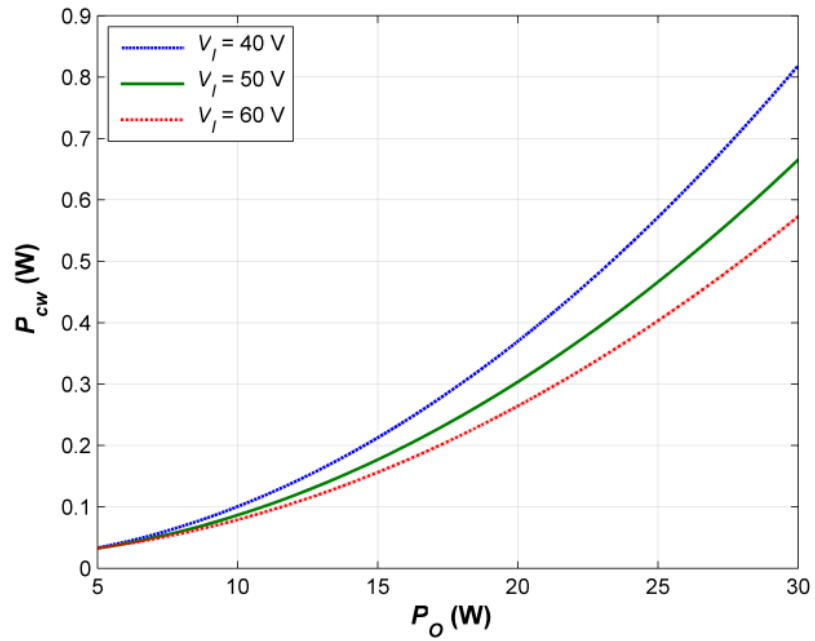
Figure 5.11: Total transformer power loss P_{cw} as a function of the output power P_O at fixed values of the DC input voltage V_I.
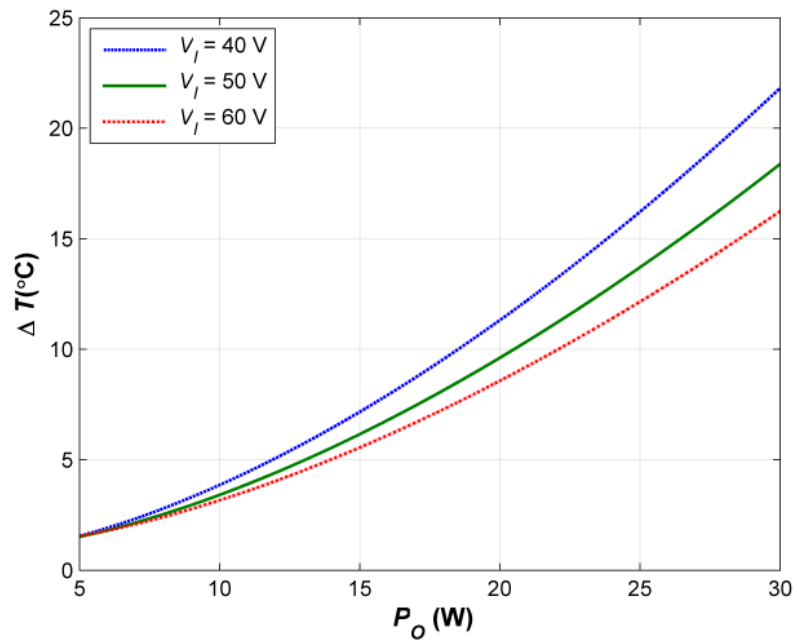
Figure 5.12: Flyback transformer temperature rise as a function of the output power P_O at fixed values of the DC input voltage V_I.
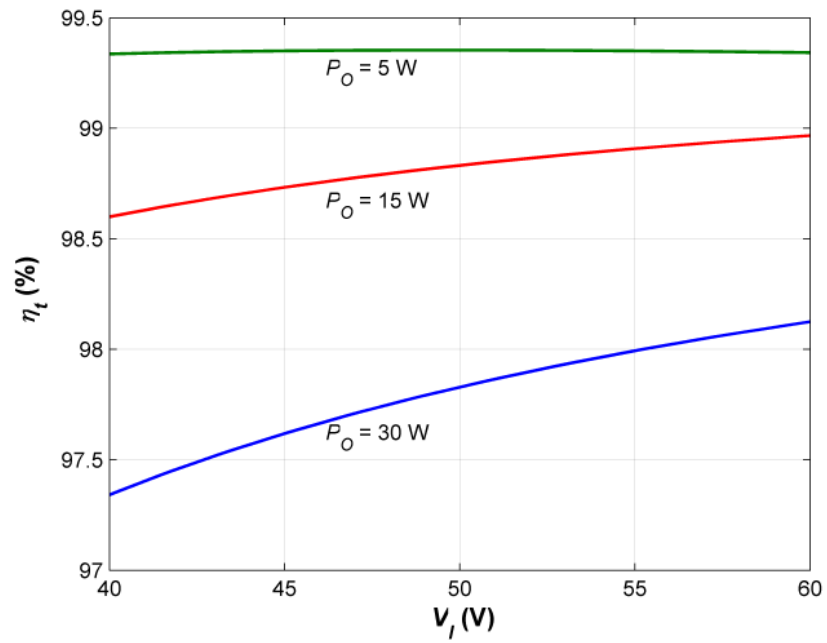
Figure 5.13: Transformer efficiency of the flyback converter in CCM as a function of the DC input voltage V_I at fixed values of the output power P_O.
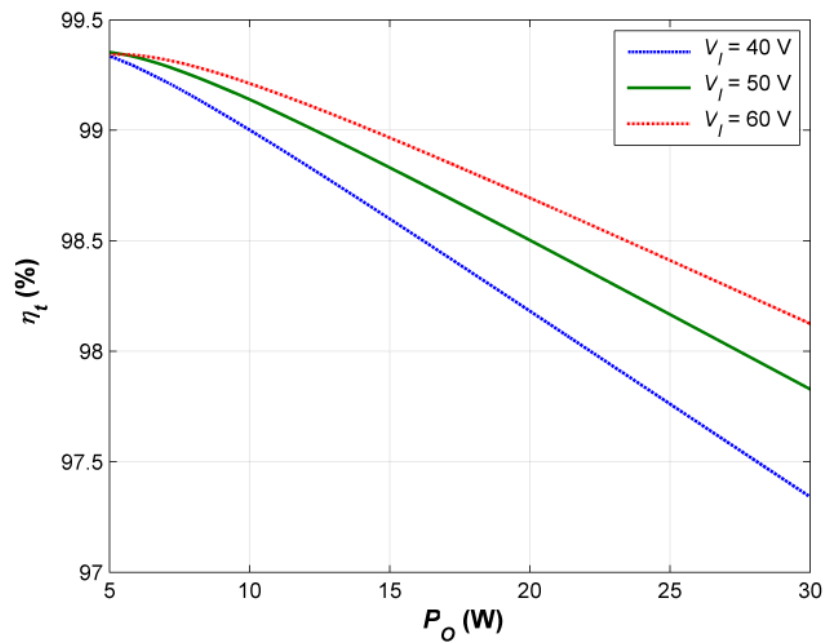
Figure 5.14: Transformer efficiency of the flyback converter in CCM as a function of the output power P_O at fixed values of the DC input voltage V_I.

the plots. From Fig. 5.1, it is clearly seen that the maximum value of F_{Rph} occurs at maximum input voltage. This is because at maximum input voltage, the duty cycle is low and the width of the primary winding current is low and contains many significant harmonics. From Fig. 5.2, it is clearly seen that the maximum value of F_{Rsh} occurs at minimum input voltage. This is because at minimum input voltage, the duty cycle is high and the width of the secondary winding current is low and contains many significant harmonics. For CCM operation, F_{Rph} and F_{Rsh} are independent of the load current. The value of F_{Rph} and F_{Rsh} at minimum input voltage for a specific case of the CCM flyback transformer is predicted to be about 5.195. Using F_{Rph} and the primary winding DC power loss, the plots of primary winding loss as a function of input voltage at fixed values of output power and as a function of output power at fixed values of input voltage, are shown in Figs. 5.3 and 5.5, respectively. The maximum primary winding power loss occurs at full load and minimum input voltage. Using F_{Rsh} and the secondary winding DC power loss, the plots of secondary winding loss as a function of input voltage at fixed values of output power and as a function of output power at fixed values of input voltage, are shown in Figs. 5.4 and 5.6, respectively. The maximum secondary winding power loss occurs at full load and minimum input voltage.

The plots of total winding power loss of the transformer as a function of input voltage at fixed values of output power and as a function of output power at fixed values of input voltage are shown in Figs. 5.7 and 5.8, respectively. The maximum total winding power loss occurs at full load and minimum input voltage. The plot of core loss as a function of input voltage is shown in Fig. 5.9. The plots of total power loss of the transformer as a function of input voltage at fixed values of output power and as a function of output power at fixed values of input voltage are shown in Figs. 5.10 and 5.11, respectively. The maximum total power loss of the transformer

occurs at full load and minimum input voltage. Fig. 5.12 shows the temperature rise in the flyback transformer as a function of output power at fixed values of input voltages. The plots of transformer efficiency as a function of input voltage at fixed values of output power and as a function of output power at fixed values of input voltage are shown in Figs. 5.13 and 5.14, respectively. As expected, the minimum efficiency of the transformer occurs at full load and minimum input voltage.

Figs. 5.15, 5.17, and 5.19 show the spectrum of the primary winding current, the primary winding ac resistance, and the primary winding power loss, respectively, for the flyback transformer in CCM at full load and minimum input voltage. The ac resistances of the primary winding of the transformer measured at 100 kHz, 200 kHz, and 400 kHz were 0.386 Ω, 0.861 Ω, and 1.588 mΩ, respectively, and were in good agreement with the theoretical values presented in Fig. 5.17. Figs. 5.16, 5.18, and 5.20 show the spectrum of the secondary winding current, the secondary winding ac resistance, and the secondary winding power loss, respectively, for the flyback transformer in CCM at full load and minimum input voltage. The ac resistances of the secondary winding of the transformer measured at 100 kHz, 200 kHz, and 400 kHz were 0.275 Ω, 0.706 Ω, and 1.404 Ω, respectively, and were in fairly good agreement with the theoretical values presented in Fig. 5.20. The winding ac resistances were measured using Hewlett Packard 4275A Multi-Frequency LCR meter. Figs. 5.21 and 5.23 show the spectrum of the primary winding current and the primary winding power loss, respectively, for the flyback transformer in CCM at full load and maximum input voltage. Figs. 5.22 and 5.24 show the spectrum of the secondary winding current and the secondary winding power loss, respectively, for the flyback transformer in CCM at full load and maximum input voltage.
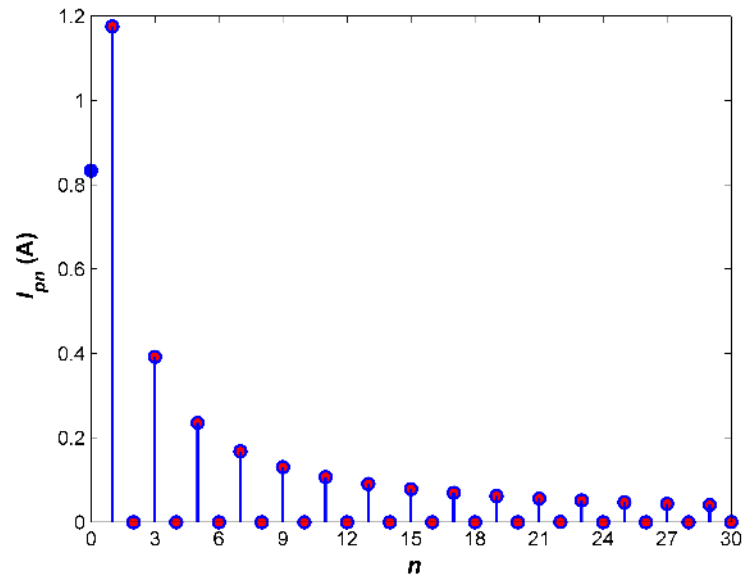
Figure 5.15: The amplitudes of the fundamental component and the harmonics of the flyback transformer primary winding current in CCM at minimum DC input voltage V_I and maximum output power P_O.
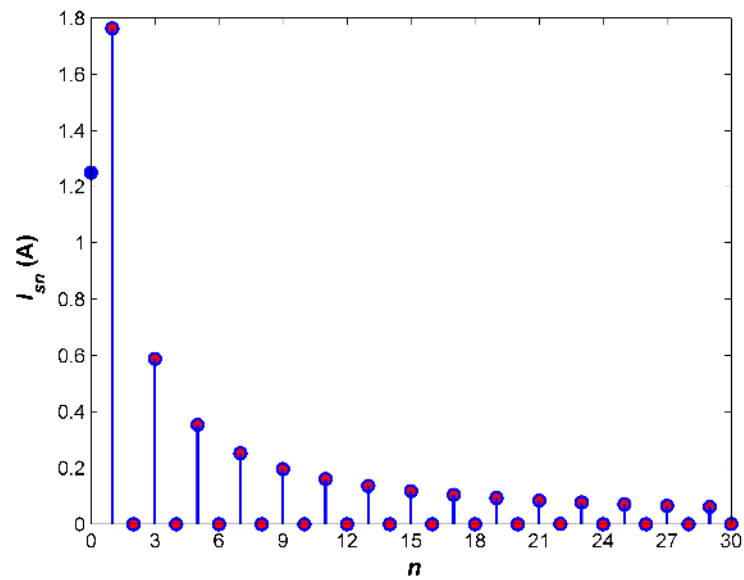
Figure 5.16: The amplitudes of the fundamental component and the harmonics of the flyback transformer secondary winding current in CCM at minimum DC input voltage V_I and maximum output power P_O.
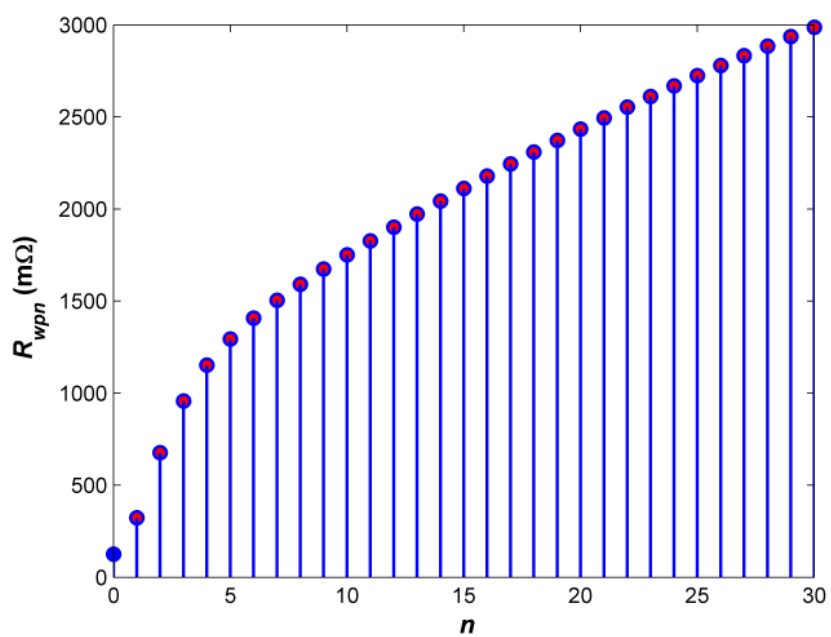
Figure 5.17: Spectrum of the primary winding ac resistance of the flyback transformer.
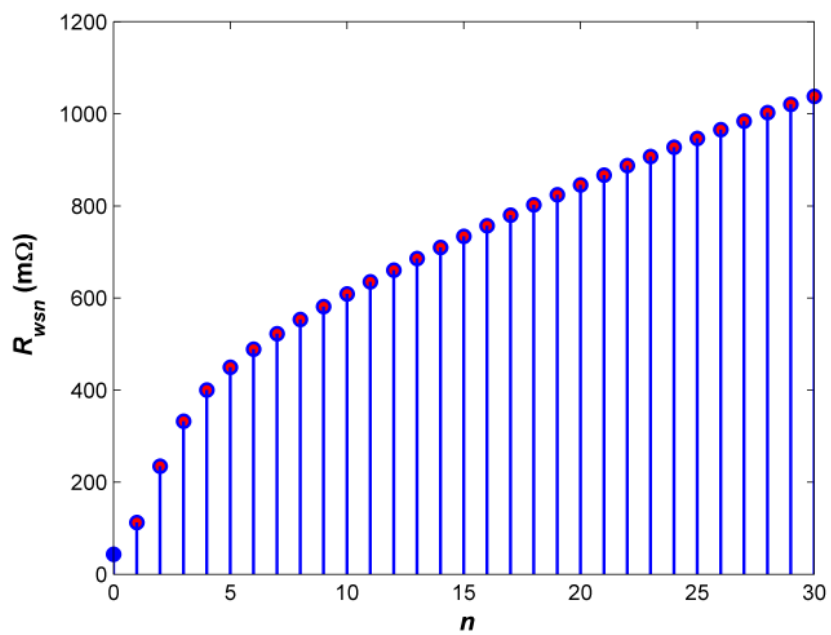
Figure 5.18: Spectrum of the secondary winding ac resistance of the flyback transformer.
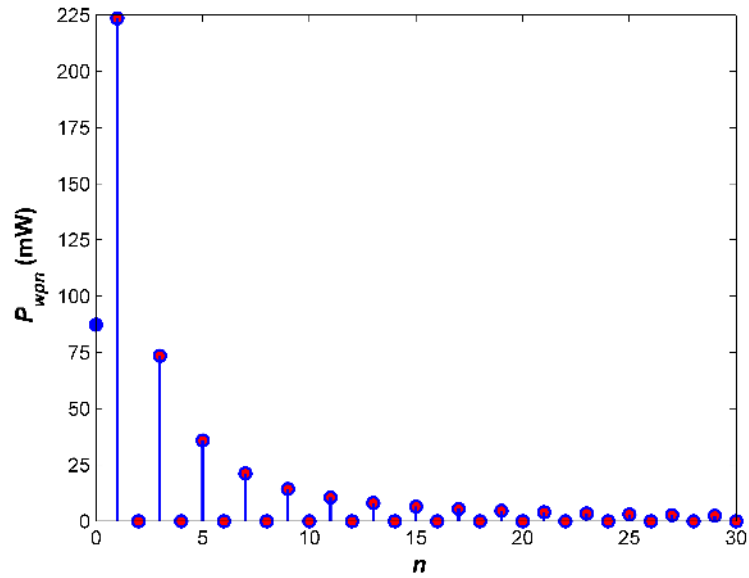
Figure 5.19: Spectrum of the primary winding power loss of the flyback transformer at minimum DC input voltage V_I and maximum output power P_O.
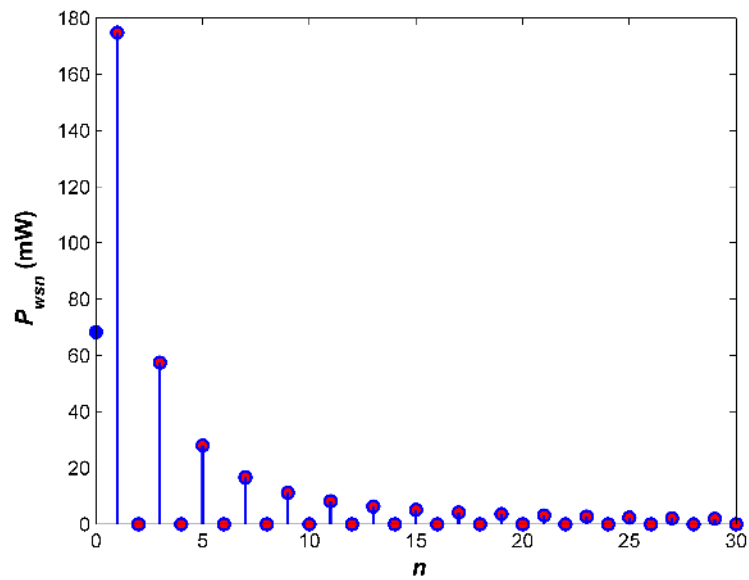
Figure 5.20: Spectrum of the secondary winding power loss of the flyback transformer at minimum DC input voltage V_I and maximum output power P_O.
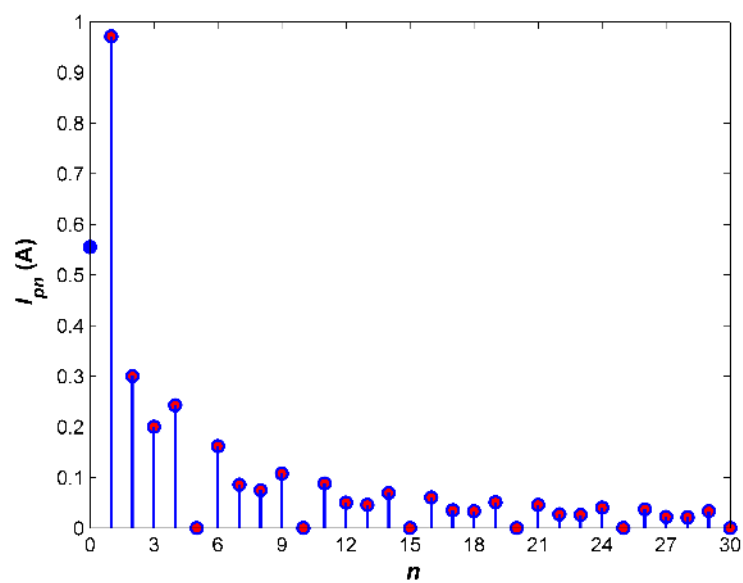
Figure 5.21: The amplitudes of the fundamental component and the harmonics of the flyback transformer primary winding current in CCM at maximum DC input voltage V_I and maximum output power P_O.
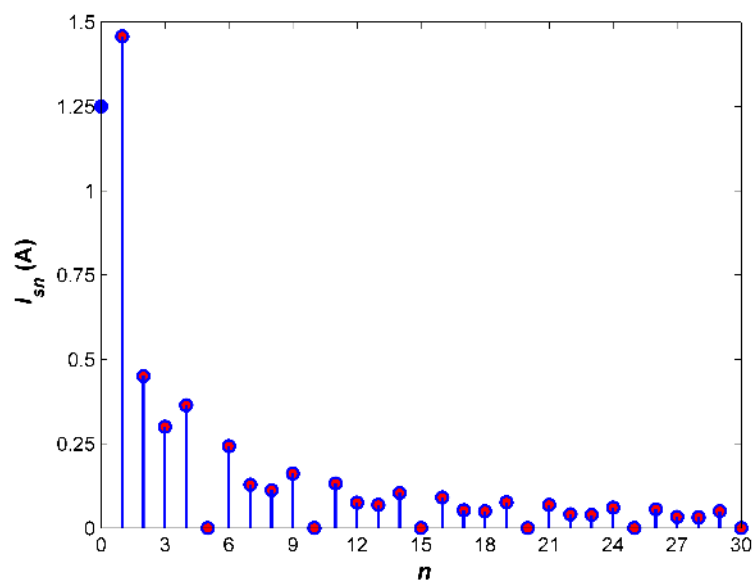
Figure 5.22: The amplitudes of the fundamental component and the harmonics of the flyback transformer secondary winding current in CCM at maximum DC input voltage V_I and maximum output power P_O.
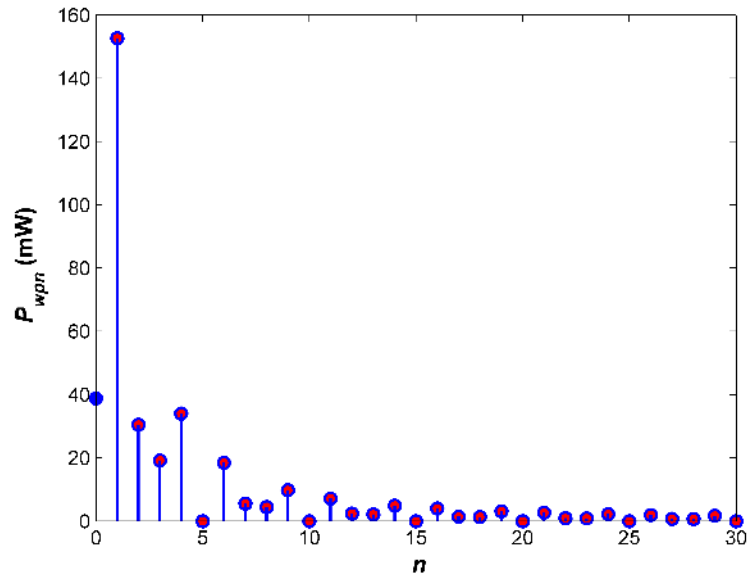
Figure 5.23: Spectrum of the primary winding power loss of the flyback transformer at maximum DC input voltage V_I and maximum output power P_O.
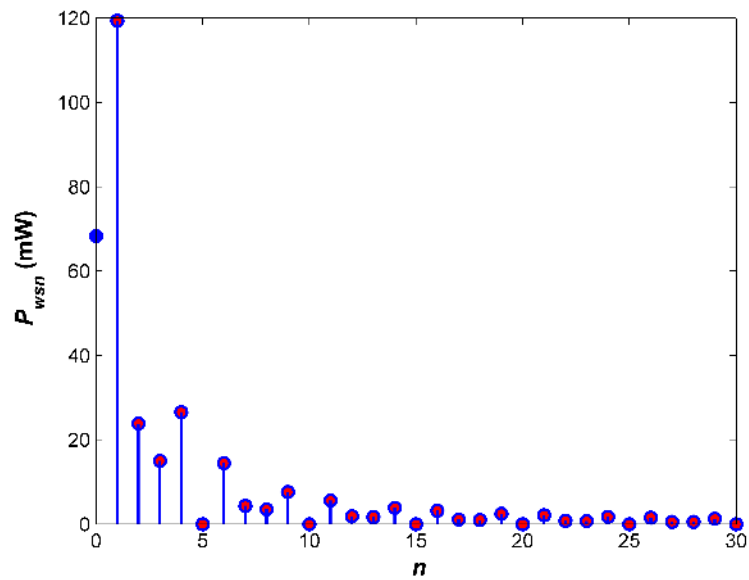
Figure 5.24: Spectrum of the secondary winding power loss of the flyback transformer at maximum DC input voltage V_I and maximum output power P_O.

Table 5.1: Two-Winding Flyback Transformer Design for CCM Operation: Core and Wire Selection

Parameter	Value
Input voltage V_I	50 ± 10 V
Output voltage V_O	24 V
Maximum output power $P_{O\max}$	30 W
Minimum output power $P_{O\min}$	5 W
Minimum DC voltage transfer function M_{VDCmin}	0.4
Maximum DC voltage transfer function M_{VDCmax}	0.6
Transformer primary-to-secondary turns ratio n	1.5
Minimum magnetizing inductance for CCM $L_p \approx L_{m(min)}$	466.56 μH; pick 500 μH
Secondary winding inductance L_s	222 μH
Maximum peak-to-peak primary winding current Δi_{Lpmax}	0.432 A
Maximum DC input current I_{Imax}	0.8333 A
Maximum peak primary winding current I_{pmax}	1.8467 A
Window utilization factor K_u	0.3
Peak flux density B_{pk}	0.31
Maximum current density of the winding wire J_m	6 A/mm^2
Maximum energy stored in the transformer magnetic field W_m	0.852 mJ
Calculated core area product A_p	0.6111 cm^4
Selected core	Magnetics RS 0P-43019
Area product of the selected core A_p	0.63 cm^4
Core cross-sectional area A_c	1.23 cm^2
Core window area W_a	0.5122 cm^2
Mean magnetic path length (MPL) l_c	4.56 cm
Mean length of single turn (MLT) l_t	6.05 cm
Core volume V_c	5.61 cm^3
Core permeability μ_{rc}	$2500 \pm 25\%$
Core saturation flux density B_s	0.49 T
Core power loss density coefficients (P-type ferrite for 100 kHz)	
k	0.0434
a	1.63
b	2.62
Skin depth of copper wire (at 20°C and $f_s = 100$ kHz)	0.209 mm
Selected copper wire	AWG 26
Bare wire diameter of the strand wire d_{is}	0.405 mm
Insulated wire diameter of the strand wire d_{os}	0.452 mm
Bare wire cross-sectional area of the strand wire A_{wsi}	0.1288 mm^2
Insulated wire cross-sectional area of the strand wire A_{wso}	0.1604 mm^2
DC resistance of the strand per unit length R_{wdc}/l_w	0.1345 Ω/m
Cross-sectional area of the primary winding wire A_{wp}	0.3078 mm^2

Table 5.2: TWO-WINDING FLYBACK TRANSFORMER DESIGN FOR CCM OPERATION: ESTIMATION OF POWER LOSSES AND EFFICIENCY

Parameter	Value
Number of strands in the primary winding S_p	2.38; pick 2
Number of turns of the primary winding N_p	29.82; pick 30
Number of turns of the secondary winding N_s	19.88; pick 20
Core air gap length l_g	0.26 mm
Maximum peak magnetic flux density B_{pk}	0.2502 T
Magnetic flux density ac component B_m	0.02439 T
Core power loss density $P_v = k(f_s \text{ in kHz})^a(10B_m)^b$	2.07 mW/cm^3
Core loss $P_c = V_c P_v$	10.99 mW
Total length of the primary winding wire l_{wp}	181.5 cm; pick 187 cm
Primary strand DC and low-frequency resistance R_{wpdcs}	251.5 mΩ
Primary winding wire DC and low-frequency resistance R_{wpdc}	125.8 mΩ
Primary winding DC and low-frequency power loss P_{wpdc}	0.08735 W
Primary winding harmonic loss factor F_{Rph}	5.195
Primary winding total power loss P_{wp}	0.4538 W
Maximum peak secondary winding current I_{smax}	2.8119 A
Cross-sectional area of the secondary winding wire A_{ws}	0.4684 mm^2
Number of strands in the secondary winding S_s	3.63; pick 4
Total length of the secondary winding wire l_{ws}	121 cm; pick 130 cm
Secondary strand DC and low-frequency resistance R_{wsdcs}	0.17485 Ω
Secondary winding wire DC and low-frequency resistance R_{wsdc}	43.71 mΩ
Secondary winding DC and low-frequency power loss P_{wsdc}	0.0685 W
Secondary winding harmonic loss factor F_{Rsh}	5.195
Secondary winding total power loss P_{ws}	0.3548 W
Total DC and low-frequency power loss in both windings P_{wdc}	0.1556 W
Total winding power loss P_w	0.8086 W
Total transfomer power loss P_{cw}	0.8195 W
Total core surface area A_t	31.95 cm^2
Surface power loss density ψ	0.0256 W/cm^2
Temperature rise of the transformer ΔT	21.79°C
Window utilization factor recalculated K_u	0.352
Transformer efficiency at full power and V_{Imin}	97.34%

5.5 Design of Flyback Transformer for DCM

The following specifications are given for the flyback PWM DC-DC converter for DCM operation:

- Input DC voltage range: $V_{Imin} \leq V_I \leq V_{Imax}$ (V)

- Output DC voltage: V_O (V)

- Maximum output current: I_{Omax} (A)

- Switching frequency: f_s (kHz)

The steps to design a two-winding flyback transformer for DCM operation are as follows. The maximum and minimum output power are

$$P_{Omax} = V_O I_{Omax} \text{ (W)} \tag{5.62}$$

and

$$P_{Omin} = V_O I_{Omin} \text{ (W)}. \tag{5.63}$$

The minimum and maximum load resistances are

$$R_{Lmin} = \frac{V_O}{I_{Omax}} \text{ (}\Omega\text{)} \tag{5.64}$$

and

$$R_{Lmax} = \frac{V_O}{I_{Omin}} \text{ (}\Omega\text{)}. \tag{5.65}$$

The minimum and maximum DC voltage transfer functions are

$$M_{VDCmin} = \frac{V_O}{V_{Imax}} \tag{5.66}$$

and

$$M_{VDCmax} = \frac{V_O}{V_{Imin}}. \tag{5.67}$$

The transformer primary-to-secondary turns ratio is

$$n_T = \frac{\eta_{conv} D_{max}}{(1 - D_{max}) M_{VDCmax}}. \tag{5.68}$$

In (5.68), the values of converter efficiency η_{conv} and maximum duty cycle D_{max} are obtained from the converter specifications. The magnetizing inductance required for DCM operation of the converter is

$$L_{pmax} \approx L_{m(max)} = \frac{n_T^2 R_{Lmin}(1 - D_{max})^2}{2f_s} \text{ (}\mu\text{H)}. \tag{5.69}$$

Pick $L_p < L_{pmax}$. The inductance of the secondary winding is

$$L_s = \frac{L_p}{n_T^2} \ (\mu\text{H}).$$ (5.70)

The maximum and minimum duty cycles at full power are

$$D_{max} = M_{VDCmax}\sqrt{\frac{2f_sL_m}{\eta_{conv}R_{Lmin}}}$$ (5.71)

and

$$D_{min} = M_{VDCmin}\sqrt{\frac{2f_sL_m}{\eta_{conv}R_{Lmin}}}.$$ (5.72)

The maximum duty cycle when the diode is ON at full power is

$$D_{1max} = \sqrt{\frac{2f_sL_m}{n_T^2R_{Lmin}}}$$ (5.73)

The maximum DC input current is

$$I_{Imax} = \frac{M_{VDCmax}I_{Omax}}{\eta_{conv}} \ (\text{A}).$$ (5.74)

The maximum peak-to-peak value of the magnetizing current and the primary current ripple is

$$I_{pmax} = \Delta i_{Lp(max)} = \Delta i_{Lm(max)} = \frac{D_{min}V_{Imax}}{f_sL_p} \ (\text{A}).$$ (5.75)

The maximum rms value of the primary winding current is

$$I_{prms(max)} = I_{pmax}\sqrt{\frac{D_{max}}{3}} \ (\text{A}).$$ (5.76)

The maximum energy stored in the magnetic field of the transformer is

$$W_m = \frac{1}{2}L_mI_{Lm(max)}^2 = \frac{1}{2}L_pI_{Lpmax}^2 \ (\text{mJ}).$$ (5.77)

Using (5.8) and (5.77), the core area product is

$$A_p = W_aA_c = \frac{2L_pI_{pmax}^2}{K_uJ_mB_{pk}} = \frac{4W_m}{K_uJ_mB_{pk}} \ (\text{cm}^4).$$ (5.78)

In calculating A_p using (5.78), the typical values of K_u, J_m, and B_{pk} are assumed. Using the core manufacturer's datasheets, a specific core whose A_p is very close to the value calculated in (5.78) is chosen and the following details of the core are obtained:

- Selected core: Core Number

- Core area product: A_p (cm^4)

- Core cross-sectional area: A_c (cm^2)

- Core window area: $W_a = A_p/A_c$ (cm^2)

- Mean magnetic path length (MPL): l_c (cm)

- Mean length of single turn (MLT): l_T (cm)

- Core volume: V_c (cm^3)

- Core surface area: A_t (cm^2)

- Core permeability: μ_{rc}

- Core saturation flux density: B_s (T)

- Core power loss density coefficients: k, a, b

The skin depth of copper wire is

$$\delta_w = \sqrt{\frac{\rho_{Cu(20°C)}}{\pi f_s \mu_0}} \text{ (mm)}. \tag{5.79}$$

To avoid skin effect, the winding wire is made up of multiple strands. The diameter of a bare strand is

$$d_{is} = 2\delta_w \text{ (mm)}. \tag{5.80}$$

Based on the bare strand diameter, a suitable AWG copper wire is chosen and the following details of the selected wire are obtained:

- Selected wire: Wire Number

- Diameter of the bare strand: d_{is} (mm)

- Diameter of the insulated strand: d_{os} (mm)

- Cross-sectional area of the bare strand: A_{wsi} (mm^2)

- Cross-sectional area of the insulated strand: A_{wso} (mm^2)

- DC resistance of the strand per unit length: R_{wdcs}/l_w ($\Omega/$m)

The cross-sectional area of the primary winding wire is

$$A_{wp} = \frac{I_{pmax}}{J_m} \text{ (mm}^2\text{)}. \tag{5.81}$$

The number of strands in the primary winding wire is

$$S_p = \frac{A_{wp}}{A_{wsi}}. \tag{5.82}$$

The core window area allocated for the primary winding is

$$W_{ap} = \frac{W_a}{2} \text{ (cm}^2\text{)}. \tag{5.83}$$

The number of turns of the primary winding is

$$N_p = \frac{K_u W_{ap}}{S_p A_{wso}}. \tag{5.84}$$

The number of turns of the secondary winding is

$$N_s = \frac{N_p}{n_T}. \tag{5.85}$$

The length of the air gap is

$$l_g = \frac{\mu_0 A_c N_p^2}{L_p} - \frac{l_c}{\mu_{rc}} \text{ (mm)}. \tag{5.86}$$

The maximum peak value of the magnetic flux density is

$$B_{pk} = \frac{\mu_0 N_p I_{pmax}}{l_g + \frac{l_c}{\mu_{rc}}} \text{ (T)}. \tag{5.87}$$

The maximum peak value of the ac component of the flux density is

$$B_{m(max)} = \frac{B_{pk}}{2}. \tag{5.88}$$

The core power loss density is

$$P_v = k(f_s \text{ in kHz})^a (10 B_m)^b \qquad (\text{mW/cm}^3). \tag{5.89}$$

The core loss is

$$P_C = V_c P_v \text{ (mW)}. \tag{5.90}$$

The total length of the primary winding wire is

$$l_{wp} = N_p l_T \text{ (cm)}. \tag{5.91}$$

The DC and low-frequency resistance of each strand of the primary winding wire is

$$R_{wpdcs} = \left(\frac{R_{wdcs}}{l_w} \right) l_{wp} \text{ (}\Omega\text{)}. \tag{5.92}$$

Hence, the DC and low-frequency resistance of the primary winding wire is

$$R_{wpdc} = \frac{R_{wpdcs}}{S_p} \text{ (}\Omega\text{)}. \tag{5.93}$$

The DC and low-frequency power loss in the primary winding is

$$P_{wpdc} = R_{wpdc} I_{Imax}^2 \text{ (W)}. \tag{5.94}$$

Using (4.44), the harmonic primary winding loss factor F_{Rph} for DCM is calculated, from which, the primary winding power loss is obtained as

$$P_{wp} = F_{Rph} P_{wpdc} \text{ (W)}. \tag{5.95}$$

The maximum current through the secondary winding is

$$I_{smax} = n \Delta i_{Lp(max)} \text{ (A)}. \tag{5.96}$$

The maximum rms value of the secondary winding current is

$$I_{srms(max)} = I_{smax} \frac{D_{1max}}{3} \text{ (A)}. \tag{5.97}$$

The cross-sectional area of the secondary winding wire is

$$A_{ws} = \frac{I_{smax}}{J_m} \text{ (mm}^2\text{)}. \tag{5.98}$$

The number of strands in the secondary winding wire is

$$S_s = \frac{A_{ws}}{A_{wsi}}. \tag{5.99}$$

The total length of the secondary winding wire is

$$l_{ws} = N_s l_T \text{ (cm)}. \tag{5.100}$$

The DC and low-frequency resistance of each strand of the secondary winding wire is

$$R_{wsdcs} = \left(\frac{R_{wdcs}}{l_w} \right) l_{ws} \text{ (}\Omega\text{)}. \tag{5.101}$$

Hence, the DC and low-frequency resistance of the primary winding wire is

$$R_{wsdc} = \frac{R_{wsdcs}}{S_s} \text{ (}\Omega\text{)}. \tag{5.102}$$

The DC and low-frequency power loss in the secondary winding is

$$P_{wsdc} = R_{wsdc} I_{Omax}^2 \text{ (W)}. \tag{5.103}$$

Using (4.51), the harmonic secondary winding loss factor F_{Rsh} for DCM is calculated, from which, the secondary winding power loss is obtained as

$$P_{ws} = F_{Rsh} P_{wsdc} \text{ (W)}. \tag{5.104}$$

The DC and low-frequency power loss in both primary and secondary windings is

$$P_{wdc} = P_{wpdc} + P_{wsdc} \text{ (W)}. \tag{5.105}$$

The total power loss in both primary and secondary windings is

$$P_w = P_{wp} + P_{ws} \text{ (W)}. \tag{5.106}$$

Sum of the core loss and the winding resistance loss in the transformer is

$$P_{cw} = P_C + P_w \text{ (W)}. \tag{5.107}$$

The efficiency of the transformer at full power is

$$\eta_t = \frac{P_O}{P_O + P_{cw}}. \tag{5.108}$$

The surface power loss density is

$$\psi = \frac{P_{cw}}{A_t} \text{ (W/cm}^2). \tag{5.109}$$

The temperature rise of the transformer is

$$\Delta T = 450 \psi^{0.826} \text{ (°C)}. \tag{5.110}$$

The core window utilization factor recalculated is

$$K_u = \frac{(N_p S_p + N_s S_s) A_{wso}}{W_a}. \tag{5.111}$$

5.6 Characteristics of High-Frequency Flyback Transformer for DCM

The theory of winding losses due to harmonics will be illustrated by the case study of the transformer used in the flyback converter operating in DCM. The following specifications of the flyback converter are used: DC input voltage $V_I = 100 \pm 20$ V, DC output voltage $V_O = 48$ V, maximum output power $P_{O\max} = 60$ W, and switching frequency $f_s = 100$ kHz. Using (5.62) - (5.111) the parameters of the flyback transformer are calculated and listed in Tables 5.3 and 5.4.
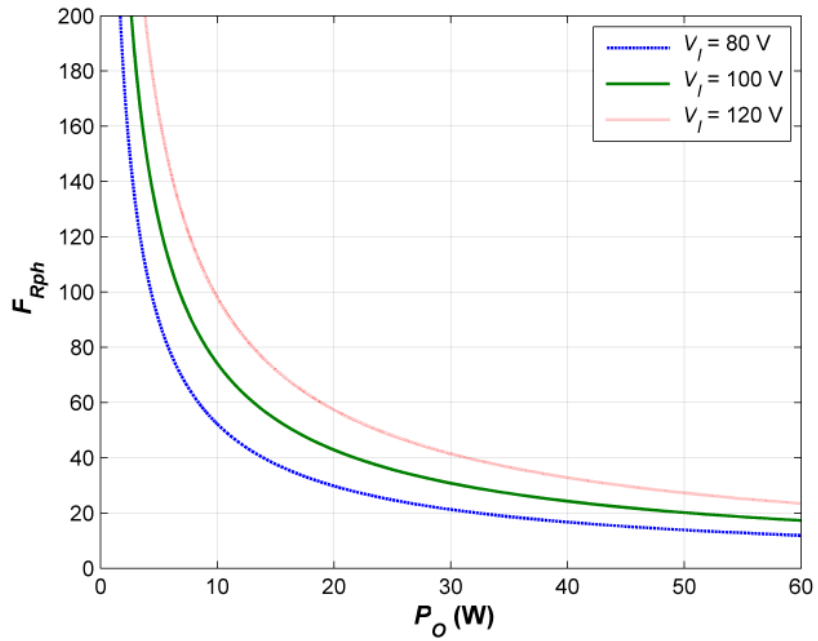
Figure 5.25: Primary winding harmonic loss factor F_{Rph} as a function of the output power P_O at fixed values of the DC input voltage V_I.

Figure 5.26: Primary winding harmonic loss factor F_{Rph} as a function of the DC input voltage V_I at fixed values of the output power P_O.
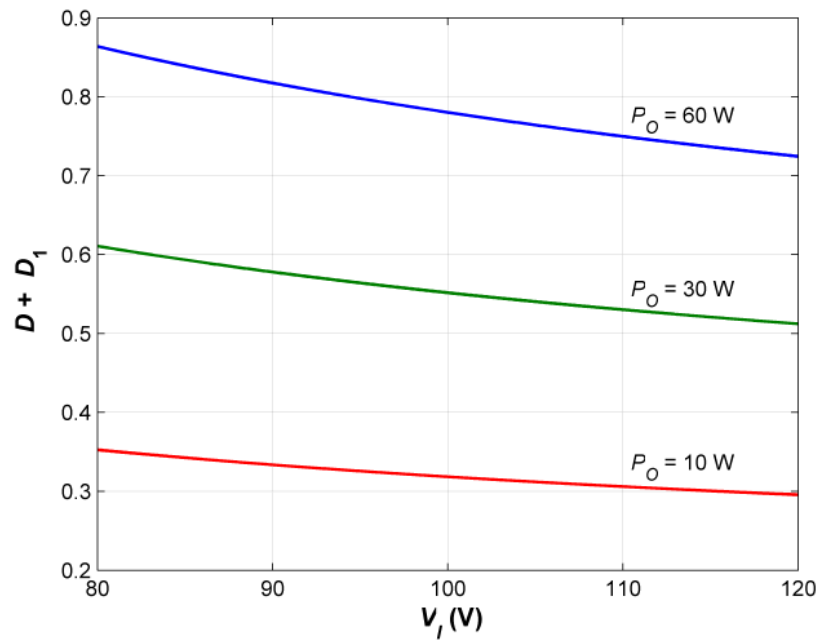
Figure 5.27: $D + D_1$ as a function of the DC input voltage V_I at fixed values of the output power P_O.
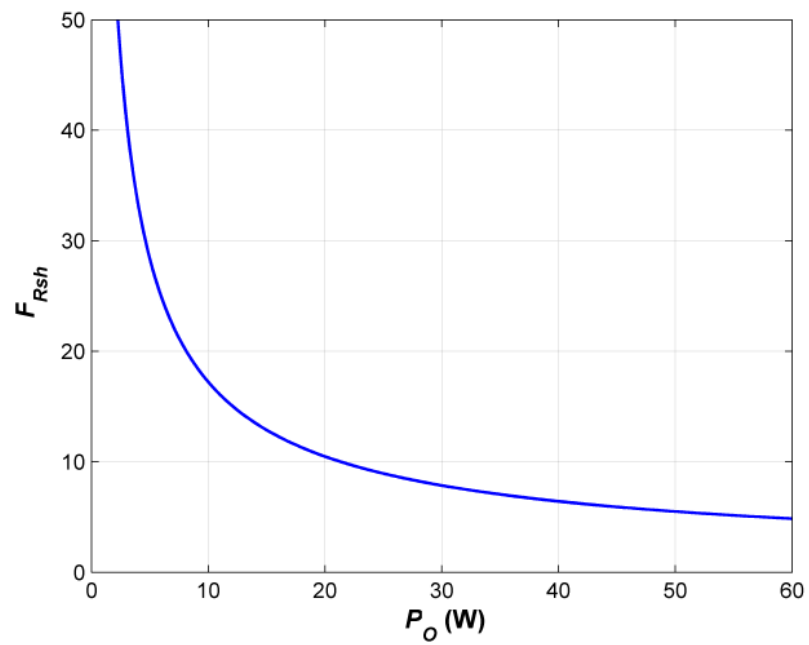
Figure 5.28: Secondary winding harmonic loss factor F_{Rsh} as a function of the output power P_O.
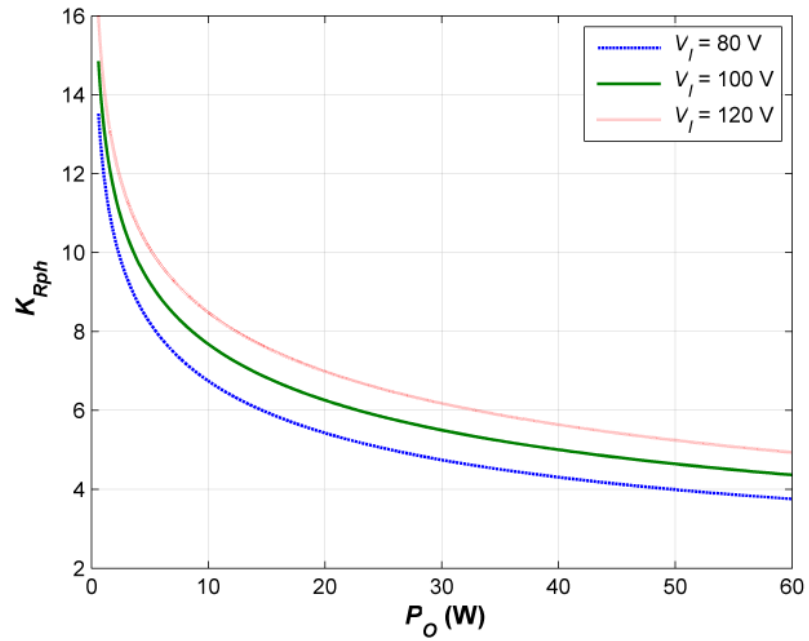
Figure 5.29: Effective primary winding resistance factor K_{Rph} as a function of the output power P_O at fixed values of the DC input voltage V_I.
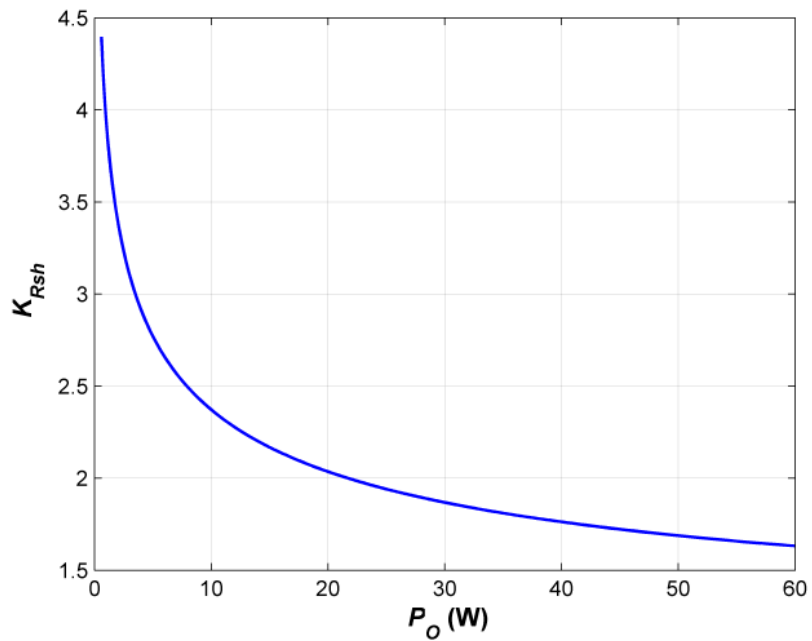
Figure 5.30: Effective secondary winding resistance factor K_{Rsh} as a function of the output power P_O.
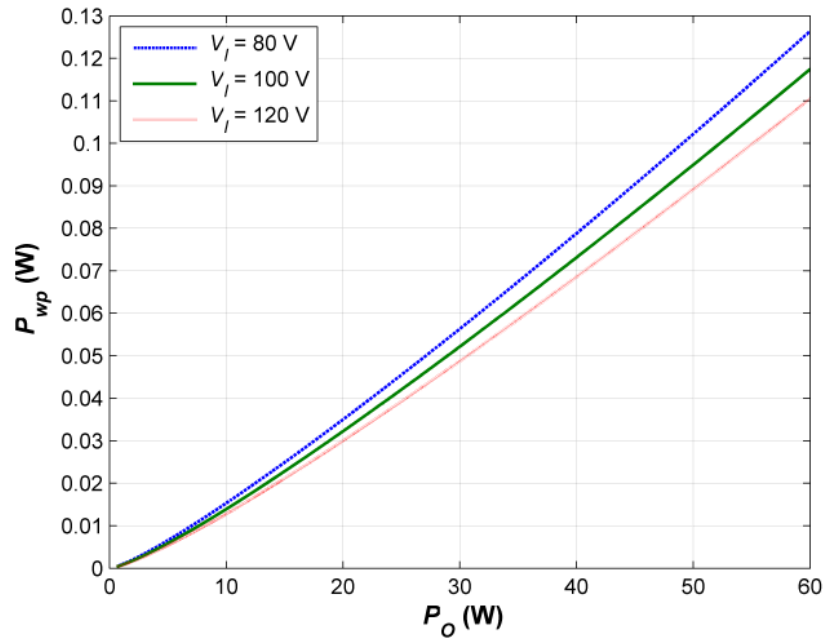
Figure 5.31: Primary winding loss P_{wp} as a function of the output power P_O at fixed values of the DC input voltage V_I.
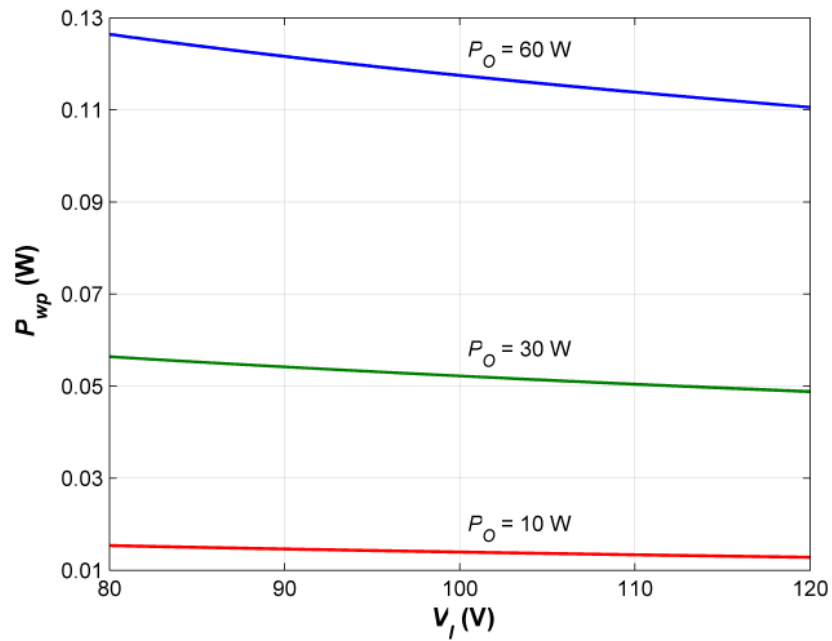
Figure 5.32: Primary winding loss P_{wp} as a function of the DC input voltage V_I at fixed values of the output power P_O.
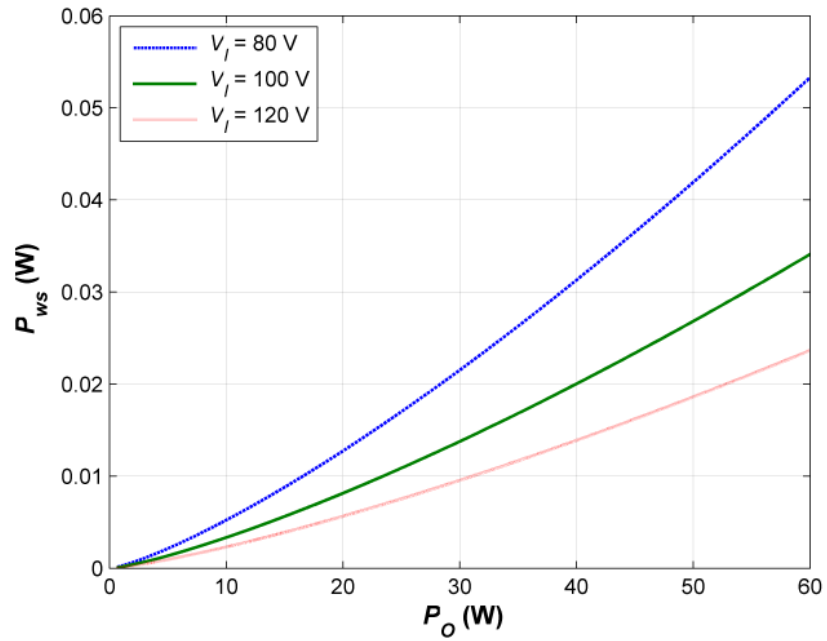
Figure 5.33: Secondary winding loss P_{ws} as a function of the output power P_O at fixed values of the DC input voltage V_I.
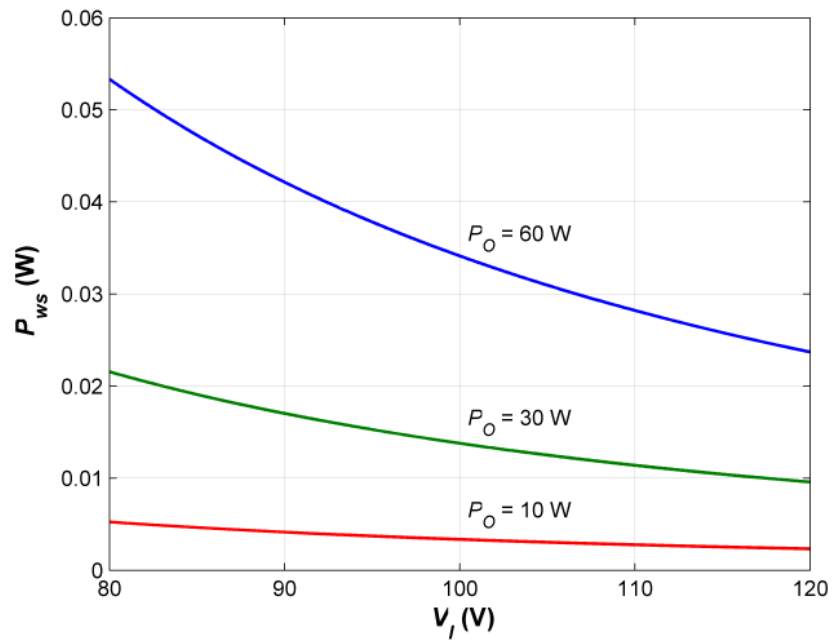
Figure 5.34: Secondary winding loss P_{ws} as a function of the DC input voltage V_I at fixed values of the output power P_O.
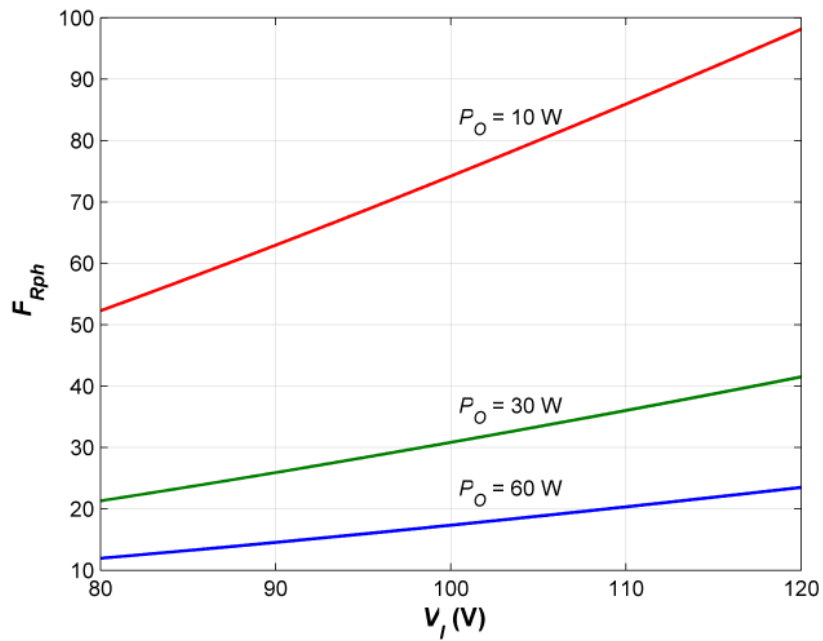
Figure 5.35: Primary and secondary winding loss P_w as a function of the output power P_O at fixed values of the DC input voltage V_I.
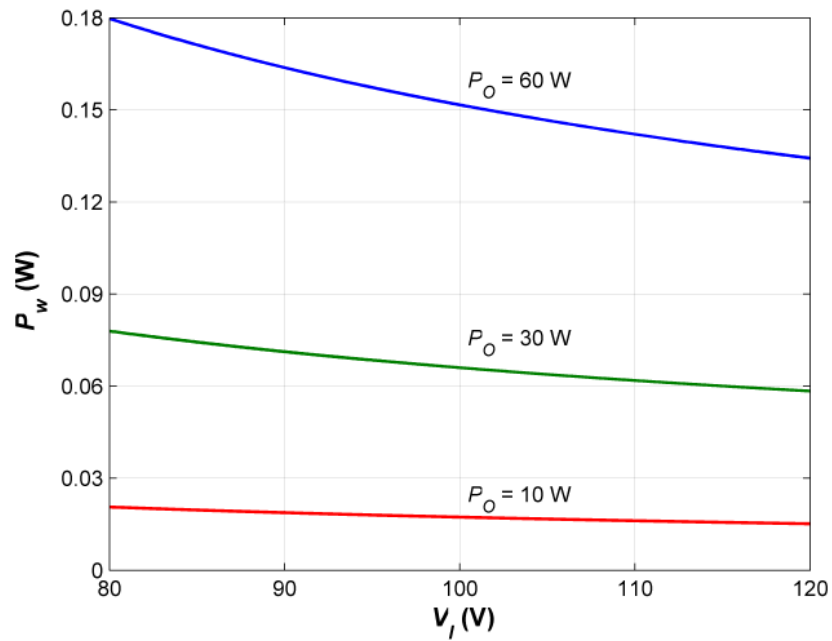
Figure 5.36: Primary and secondary winding loss P_w as a function of the DC input voltage V_I at fixed values of the output power P_O.
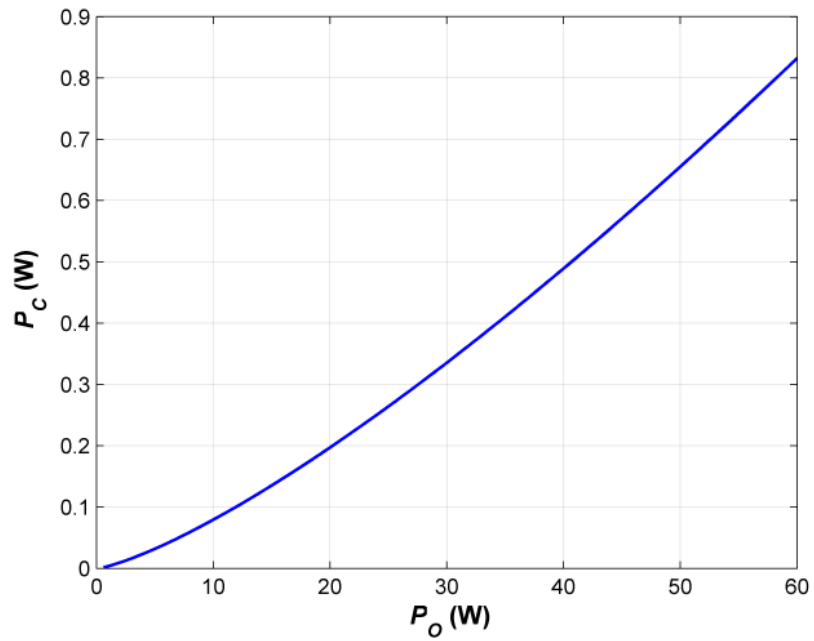
Figure 5.37: Core loss P_C as a function of the output power P_O.
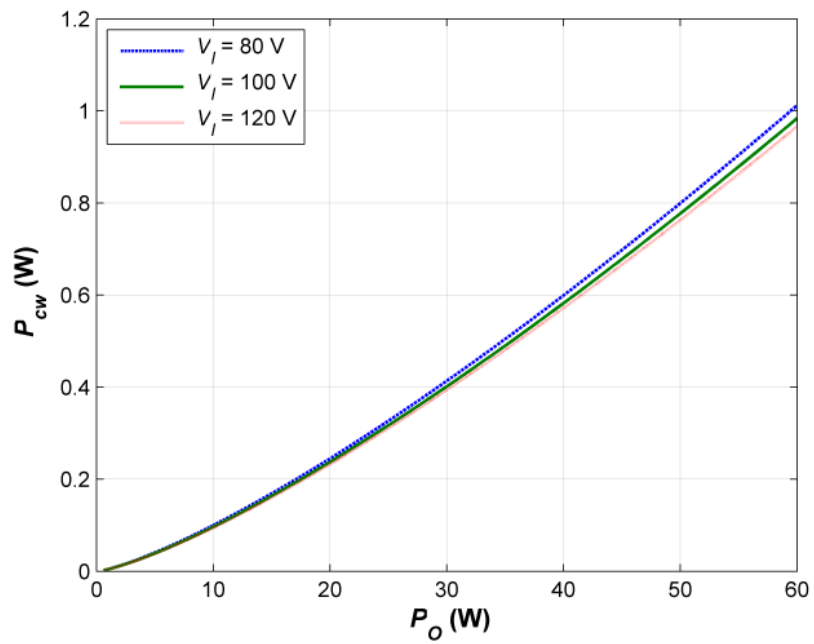
Figure 5.38: Total transformer power loss P_{cw} as a function of the output power P_O at fixed values of the DC input voltage V_I.
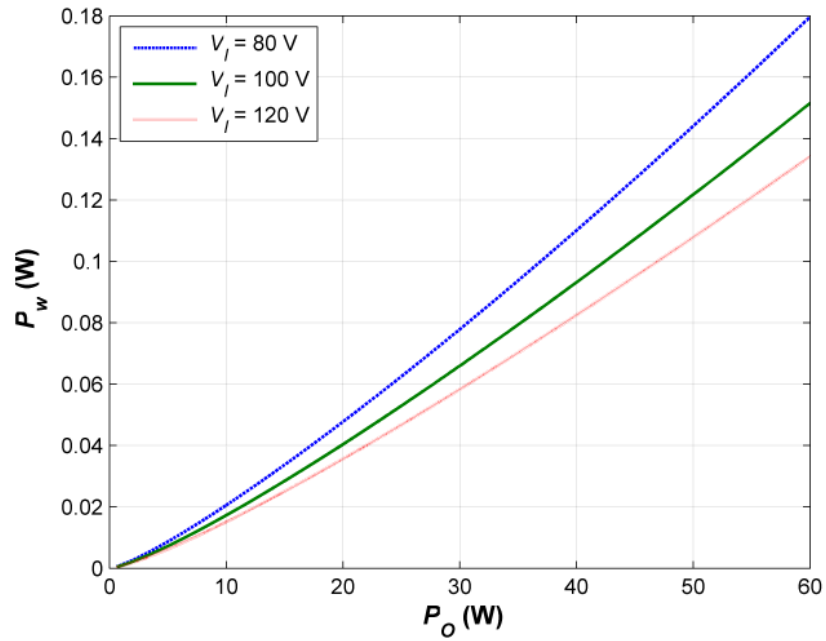
In this section, the computed characteristics of the designed transformer are presented for a wide range of operating conditions of the flyback converter in DCM i.e., over the entire range of the load current and the DC input voltage. Plots of primary winding harmonic loss factor F_{Rph} as functions of output power and input voltage are shown in Figs. 5.25 and 5.26, respectively, using (4.32), (4.24), and (4.44) for $N_l = 2$, $d/\delta_{w1} = 1.9378$, $d/p = 0.8$, and $n = 100$. Plot of secondary winding harmonic loss factor F_{Rsh} as a function of output power is shown in Fig. 5.25, using (4.32), (4.24), and (4.51) for $N_l = 1$, $d/\delta_{w1} = 1.9378$, $d/p = 0.8$, and $n = 100$. Table 5.5 gives the variation of F_{Rph} and F_{Rsh} with respect to the number of harmonics n at full power and maximum DC input voltage. The values of F_{Rph} and F_{Rsh} were calculated with $n = 100$ for all the plots. When $D + D_1$ is close to 1, a lower number of harmonics n is sufficient, typically $n = 50$. When $D + D_1$ is low, then higher number of harmonics is needed, typically $n = 100$. From Figs. 5.25 - 5.28, it is clearly seen that the maximum values of F_{Rph} and F_{Rsh} occur at light load and maximum input voltage. This is because at light load, the duty cycle is low and the primary/secondary winding current contains many significant harmonics. The values of F_{Rph} and F_{Rsh} at full load and maximum input voltage for a specific case of the DCM flyback transformer are predicted to be about 23 and 5, respectively. Plots of effective primary and secondary resistance factors K_{Rph} and K_{Rsh} are shown in Figs. 5.29 and 5.30, respectively for $n = 100$. The values of K_{Rph} and K_{Rsh} at full load and maximum input voltage for a specific case of the DCM flyback transformer are predicted to be about 5 and 1.6, respectively. As the output power P_O decreases, both K_{Rph} and K_{Rsh} increase because of the decrease in the duty cycle. Using F_{Rph} and the primary winding DC power loss, the plots of primary winding loss as a function of output power at fixed values of input voltage and as a function of input voltage at fixed values of output power, are shown in Figs. 5.31 and 5.32, respectively. The maximum primary winding power

loss occurs at full load and minimum input voltage. Using F_{Rsh} and the secondary winding DC power loss, the plots of secondary winding loss as a function of output power at fixed values of input voltage and as a function of input voltage at fixed values of output power, are shown in Figs. 5.33 and 5.34, respectively. The maximum secondary winding power loss occurs at full load and minimum input voltage.

The plots of total winding power loss of the transformer as a function of output power at fixed values of input voltage and as a function of input voltage at fixed values of output power, are shown in Figs. 5.35 and 5.36, respectively. The maximum total winding power loss occurs at full load and minimum input voltage. The plot of core loss as a function of output power is shown in Fig. 5.37. The plot of total power loss of the transformer as a function of output power at fixed values of input voltage is shown in Fig. 5.38. The maximum total power loss of the transformer occurs at full load and minimum input voltage. Fig. 5.39 shows the efficiency of the transformer as a function of output power. As expected, the minimum efficiency of the transformer occurs at full load and minimum input voltage. Fig. 5.40 shows the temperature rise in the flyback transformer as a function of output power at fixed values of input voltages.

Figs. 5.41, 5.43, and 5.45 show the spectrum of the primary winding current, the primary winding ac resistance, and the primary winding power loss, respectively, for the flyback transformer in DCM at full load and minimum input voltage. The ac resistances of the primary winding of the transformer measured at 100 kHz, 200 kHz, and 400 kHz were 35.1 mΩ, 76.8 mΩ, and 138 mΩ, respectively, and were in excellent agreement with the theoretical values presented in Fig. 5.43. Figs. 5.42, 5.44, and 5.45 show the spectrum of the secondary winding current, the secondary winding ac resistance, and the secondary winding power loss, respectively, for the flyback transformer in DCM at full load and minimum input voltage. The ac resistances
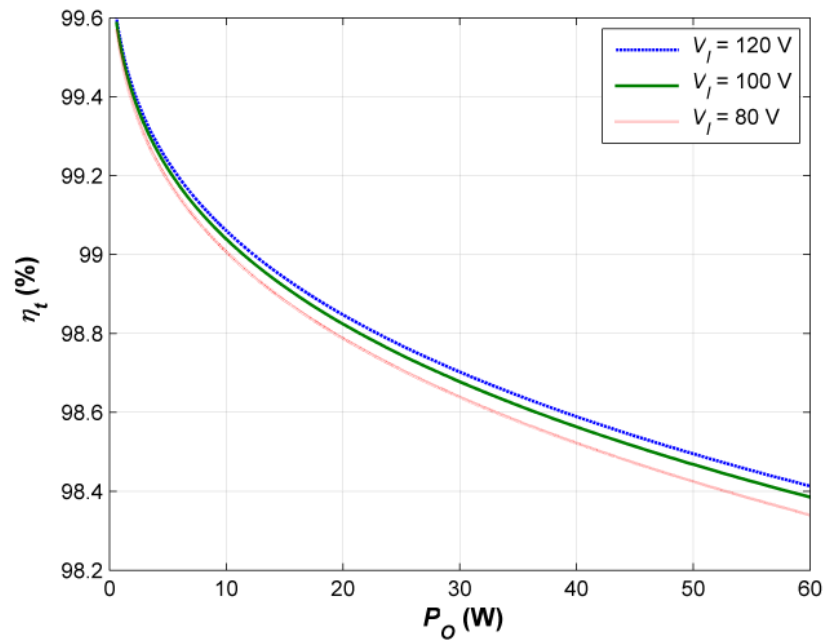
Figure 5.39: Transformer efficiency of the flyback converter in DCM as a function of the output power P_O at fixed values of the DC input voltage V_I.
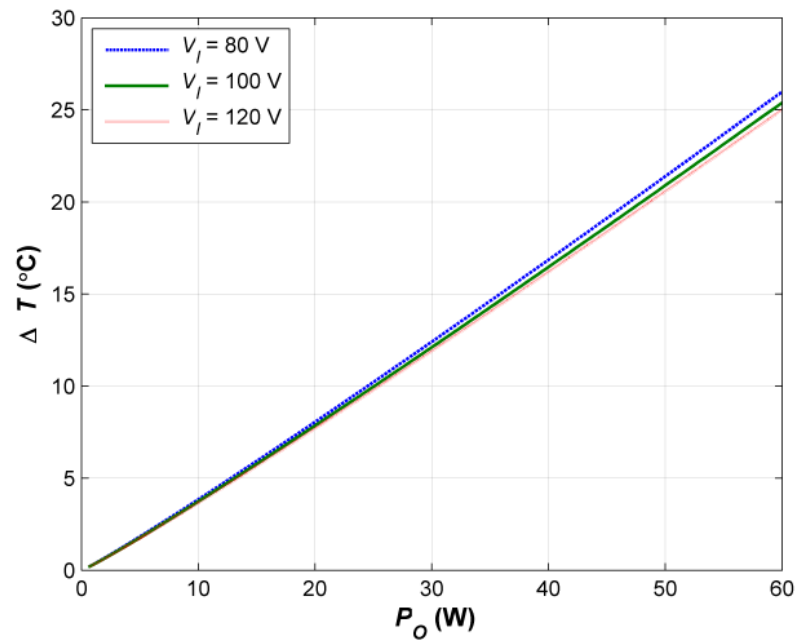
Figure 5.40: Flyback transformer temperature rise as a function of the output power P_O at fixed values of the DC input voltage V_I.
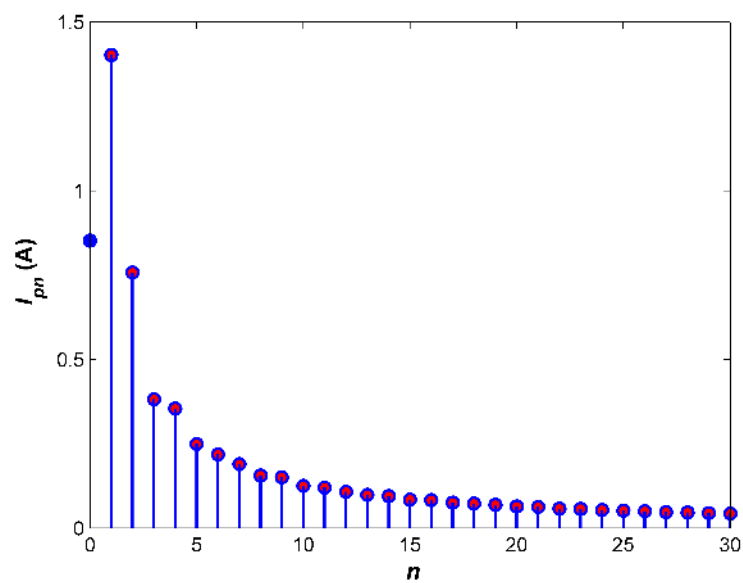
Figure 5.41: The amplitudes of the fundamental component and the harmonics of the flyback transformer primary winding current at minimum DC input voltage and maximum output power.
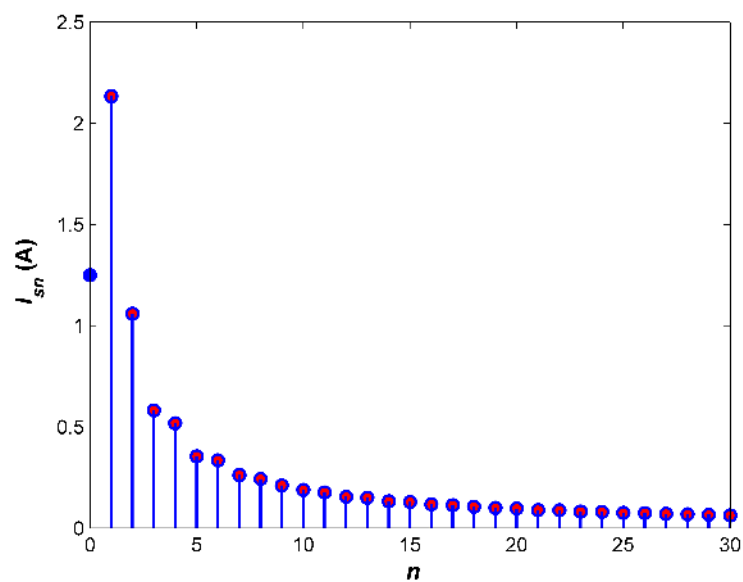
Figure 5.42: The amplitudes of the fundamental component and the harmonics of the flyback transformer secondary winding current at minimum DC input voltage and maximum output power.
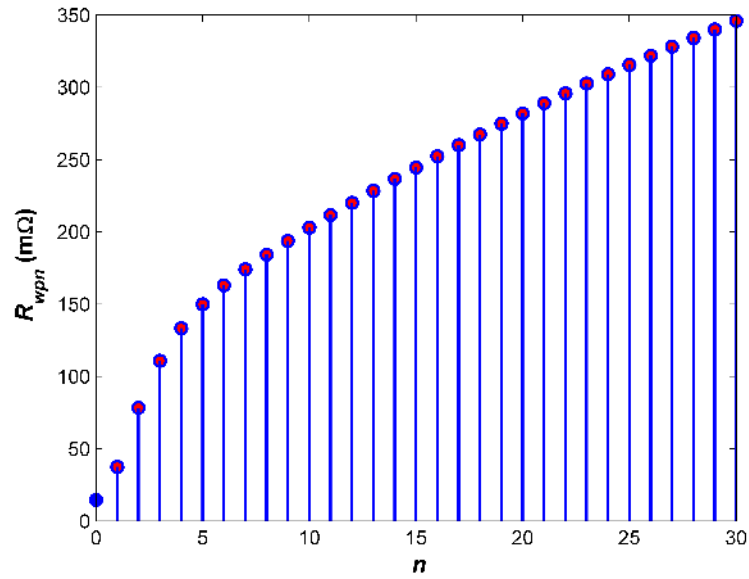
Figure 5.43: Spectrum of the primary winding ac resistance of the flyback transformer.
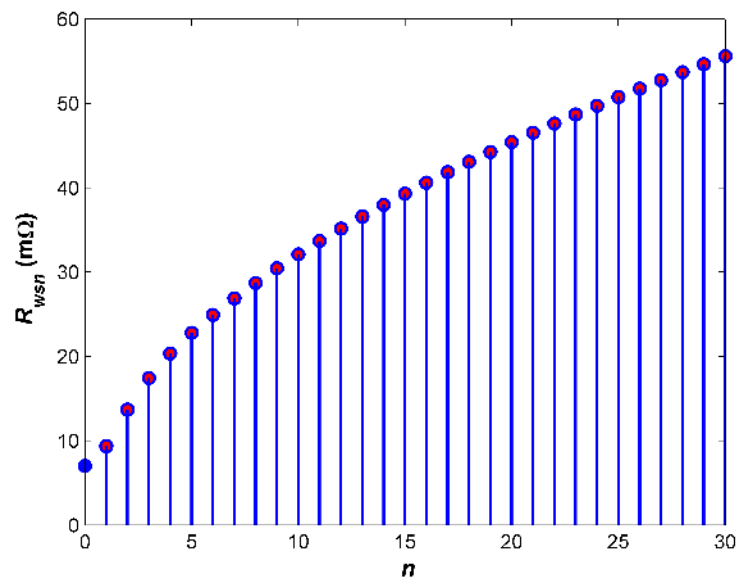
Figure 5.44: Spectrum of the secondary winding ac resistance of the flyback transformer.
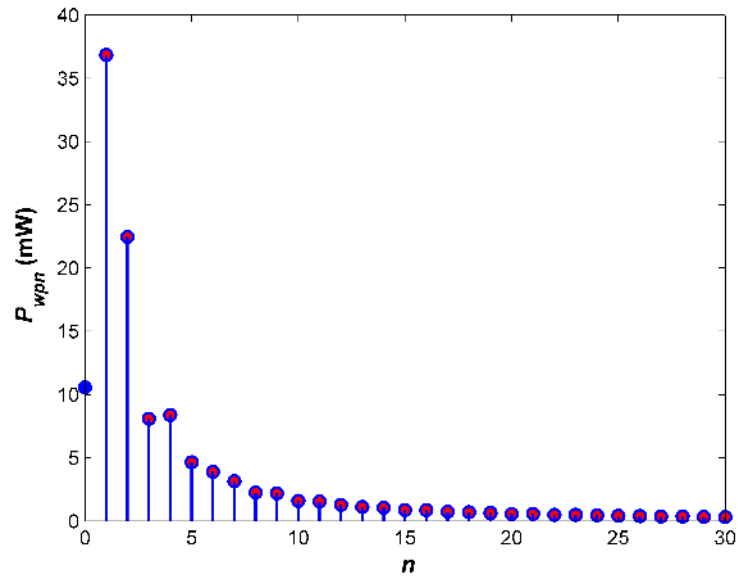
Figure 5.45: Spectrum of the primary winding power loss of the flyback transformer at minimum DC input voltage and maximum output power.
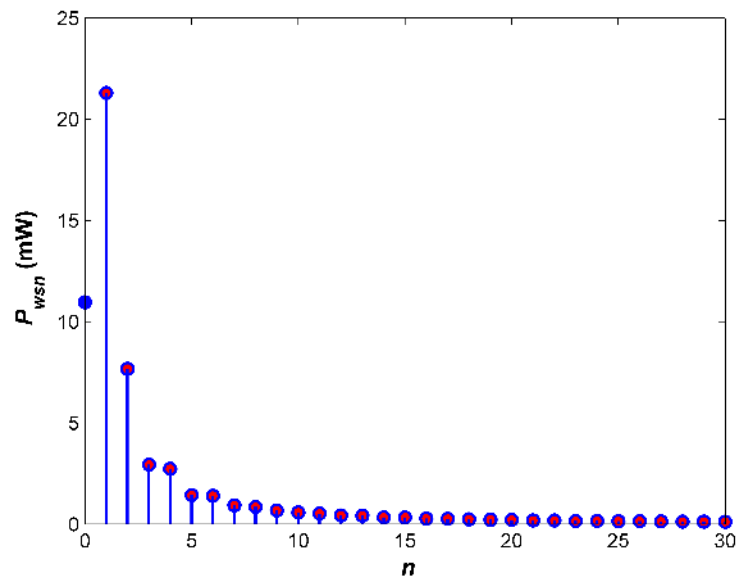
Figure 5.46: Spectrum of the secondary winding power loss of the flyback transformer at minimum DC input voltage and maximum output power.

Table 5.3: TWO-WINDING FLYBACK TRANSFORMER DESIGN FOR DCM OPERATION: CORE AND WIRE SELECTION

Parameter	Value
Input voltage V_I	100 ± 10 V
Output voltage V_O	48 V
Maximum output power $P_{O\max}$	60 W
Switching frequency f_s	100 kHz
Minimum DC voltage transfer function M_{VDCmin}	0.4
Maximum DC voltage transfer function M_{VDCmax}	0.6
Transformer primary-to-secondary turns ratio n_T	1.466
Maximum magnetizing inductance for DCM $L_p \approx L_{m(max)}$	103.16 μH; pick 82 μH
Secondary winding inductance L_s	38.15 μH
Maximum duty cycle D_{max}	0.418
Minimum duty cycle D_{min}	0.2786
Minimum duty cycle when the diode is on D_{1max}	0.4457
Maximum DC input current I_{Imax}	0.8523 A
Maximum peak primary winding current $I_{pmax} = \Delta i_{Lpmax}$	4.077 A
Maximum primary rms current $I_{prms\max}$	1.521 A
Window utilization factor K_u	0.3
Peak flux density B_{pk}	0.25
Maximum current density of the winding wire J_m	5 A/mm^2
Maximum energy stored in the transformer magnetic field W_m	0.681 mJ
Calculated core area product A_p	0.7264 cm^4
Selected core	Magnetics PC 0P-43019
Area product of the selected core A_p	0.73 cm^4
Core cross-sectional area A_c	1.37 cm^2
Core window area W_a	0.5328 cm^2
Mean magnetic path length (MPL) l_c	4.52 cm
Mean length of single turn (MLT) l_t	6.078 cm
Core volume V_c	6.19 cm^3
Core permeability μ_{rc}	$2500 \pm 25\%$
Core saturation flux density B_s	0.49 T
Core power loss density coefficients (P-type ferrite for 100 kHz)	
k	0.0434
a	1.63
b	2.62
Skin depth of copper wire (at 20°C and $f_s = 100$ kHz)	0.209 mm
Selected copper wire	AWG 26
Bare wire diameter of the strand wire d_{is}	0.405 mm
Insulated wire diameter of the strand wire d_{os}	0.452 mm
Bare wire cross-sectional area of the strand wire A_{wsi}	0.1288 mm^2
Insulated wire cross-sectional area of the strand wire A_{wso}	0.1604 mm^2
DC resistance of the strand per unit length R_{wdc}/l_w	0.1345 Ω/m

Table 5.4: TWO-WINDING FLYBACK TRANSFORMER DESIGN FOR DCM OPERATION: ESTIMATION OF POWER LOSSES AND EFFICIENCY

Parameter	Value
Cross-sectional area of the primary winding wire A_{wp}	0.8154 mm^2
Number of strands in the primary winding S_p	6.33; pick 6
Number of turns of the primary winding N_p	10.34; pick 10
Number of turns of the secondary winding N_s	6.82; pick 7
Core air gap length l_g	0.191 mm
Maximum peak magnetic flux density B_{pk}	0.245 T
Magnetic flux density ac component B_m	0.1225 T
Core power loss density $P_v = k(f_s \text{ in kHz})^a (10B_m)^b$	134.4 mW/cm^3
Core loss $P_c = V_c P_v$	0.832 W
Total length of the primary winding wire l_{wp}	60.78 cm; pick 65 cm
Primary strand DC and low-frequency resistance R_{wpdcs}	0.0874 Ω
Primary winding wire DC and low-frequency resistance R_{wpdc}	14.57 mΩ
Primary winding DC and low-frequency power loss P_{wpdc}	0.01058 W
Primary winding harmonic loss factor F_{Rph}	11.95
Primary winding total power loss P_{wp}	0.1264 W
Maximum peak secondary winding current I_{smax}	5.97 A
Maximum secondary rms current $I_{srms(\max)}$	2.3 A
Cross-sectional area of the secondary winding wire A_{ws}	1.194 mm^2
Number of strands in the secondary winding S_s	9.27; pick 9
Total length of the secondary winding wire l_{ws}	42.54 cm; pick 47 cm
Secondary strand DC and low-frequency resistance R_{wsdcs}	0.0632 Ω
Secondary winding wire DC and low-frequency resistance R_{wsdc}	7.02 mΩ
Secondary winding DC and low-frequency power loss P_{wsdc}	0.01096 W
Secondary winding harmonic loss factor F_{Rsh}	4.86
Secondary winding total power loss P_{ws}	0.0532 W
Total DC and low-frequency power loss in both windings P_{wdc}	0.02154 W
Total winding power loss P_w	0.1796 W
Total transformer power loss P_{cw}	1.011 W
Total core surface area A_t	31.95 cm^2
Surface power loss density ψ	0.0316 W/cm^2
Temperature rise of the transformer ΔT	25.94°C
Window utilization factor recalculated K_u	0.2973
Transformer efficiency at full power and V_{Imin}	98.34%

of the secondary winding of the transformer measured at 100 kHz, 200 kHz, and 400 kHz were 15.48 mΩ, 28.22 mΩ, and 494.7 mΩ, respectively, and were in fairly good agreement with the theoretical values presented in Fig. 5.44. The winding ac

Table 5.5: VARIATION OF F_{Rph} AND F_{Rsh} WITH RESPECT TO NUMBER OF HARMONICS n AT P_{Omax} AND V_{Imax}

Number of Harmonics n	F_{Rph}	F_{Rsh}
1	5.33	2.71
2	10.66	3.32
3	13.66	3.56
5	15.86	3.89
10	18.79	4.25
25	21.28	4.57
50	22.58	4.74
100	23.51	4.86
200	24.17	4.95
500	24.72	5.03

resistances were measured using Hewlett Packard 4275A Multi-Frequency LCR meter.

6   Conclusions

6.1   Summary

The steady-state analysis of the hard-switching two-switch flyback converter for CCM and DCM operations, taking switch output capacitance and transformer leakage inductance into account, have been presented. Incorporation of an additional switch and two clamping diodes into the classical single-switch flyback topology provides a simple mechanism to limit the switch overvoltage. This turn-off voltage stress is predictable and well determined. The theoretical analyses have been verified by experimental results. Clamping of the switch overvoltage is achieved. The power transistors are turned on under reduced stresses. These stresses are also well determined. The uncertainty of the voltage stress in the single-switch flyback converter is removed in the two-switch flyback converter at the expense of an additional switch and two clamping diodes. The detailed analysis and experimental results provide an in-depth understanding of the converter operation. The two-switch flyback converter is a simple topology with a high practical value for low power applications.

The circuit operation and steady-state analysis of the proposed ZCT two-switch flyback converter have been presented. The theoretical analysis of the soft-switching ZCT two-switch flyback converter has been verified by simulation and experimental results. All the semiconductor devices in the proposed ZCT two-switch flyback converter are operated under zero-current switching condition, thereby resulting in reduced turn-off switching losses of the converter. The maximum voltages across the main switches are limited to the DC input voltage.

General expressions for the winding power loss for transformer primary and secondary periodic nonsinusoidal current waveforms have been derived. Dowell's theory has been applied only to sinusoidal current waveform cases in magnetic devices. Fourier expansions of transformer current waveforms have been derived for single-

ended isolated DC-DC converters for both CCM and DCM operations. The winding power loss due to harmonics of the transformer current is not negligible. Examples illustrating the design of two-winding flyback transformer for both CCM and DCM operations have been presented.

Two expressions for the winding power loss for periodic nonsinusoidal transformer current waveform have been derived. A case study for copper losses in a flyback PWM converter operating in CCM has been presented. For CCM operation of PWM converters, the winding power loss due to harmonics of the transformer current is not negligible. This loss changes when the DC input voltage and the load current of the converter is varied. The maximum winding current loss occurs at the minimum DC input voltage V_I and maximum output power for the CCM flyback converter. The primary winding harmonic loss factor F_{Rph} increases as the DC input voltage increases, whereas, the secondary winding harmonic loss factor F_{Rsh} decreases as the DC input voltage increases, both of which occur irrespective of the change in load power.

For DCM operation of PWM converters, the winding power loss due to harmonics of the transformer currents is not negligible. The number of significant harmonics in PWM converters operating in DCM is high, of the order of 50-100. As the duty cycle decreases, the number of significant harmonics increases. The power losses in both windings change when the DC input voltage and the load current of the converter is varied. The maximum winding power loss occurs at full load and minimum DC input voltage for the flyback converter. The primary winding harmonic loss factor F_{Rph} and the secondary winding harmonic loss factor F_{Rsh} significantly increase as $D + D_1$ decreases, both of which occur when the output power decreases. The effective primary resistance factor K_{Rph} and the effective secondary resistance factor K_{Rsh} also significantly increase as $D + D_1$ decreases. The core loss of the transformer increases

with increasing output power.

6.2   Dissertation Contributions

The contributions of this work to the field of research are:

- Analytical work comprising steady-state analysis and design procedure of the basic hard-switching two-switch flyback PWM DC -DC converter for both CCM and DCM modes are presented.

- A new soft-switching two-switch flyback converter topology with reduced switch voltage stress is proposed.

- Principle of circuit operation, steady-state analysis, and design procedure of the proposed soft-switching ZCT two-switch flyback converter are given.

- A general expression for the transformer winding power loss for periodic nonsinusoidal waveform is derived.

- Fourier expansions of transformer current waveforms for single-ended isolated DC-DC converters operated in CCM and DCM modes are carried out.

- Two specific expressions for the winding power loss in a two-winding flyback transformer are given, for both CCM and DCM modes.

- The harmonic winding loss factors F_{Rph} and F_{Rsh}, for a two-winding transformer are introduced.

- Using the area product method, detailed step-by-step procedures to design a two-winding transformer for both CCM and DCM cases are presented.

References

[1] R. E. Tarter, *Principles of Solid-State Power Conversion.* H. W. Sams, Indianapolis, 1985.

[2] B. K. Bose, *Power Electronics: Evolution, Technology, and Applications.* IEEE Press, NJ, 1991.

[3] M. H. Rashid, *Power Electronics, Circuits, Devices, and Applications.* Prentice-Hall, NJ, 1993.

[4] N. Mohan, T. M. Undeland, and W. P. Robbins, *Power Electronics: Converters, Application, and Design.* John Wiley & Sons, Hoboken, 2003.

[5] M. K. Kazimierczuk, *Pulse-Width Modulated DC-DC Power Converters.* John Wiley & Sons, Chichester, 2008.

[6] *Flyback Converter Serves Battery-Powered CCD Applications.* Maxim Application Note APP655, 2001.

[7] H.-S. Choi, *Design Guidelines for Off-Line Flyback Converters Using Fairchild Power Switch.* Fairchild Semiconductor Application Note AN4137, 2003.

[8] *Universal Input, 15 V Output, 90 W Flyback Power Supply.* International Rectifier Reference Design IRISMPS5, 2004.

[9] T. Cleveland, *Bi-Directional, Portable Power-Management System for Multi-Cell, Li-Ion Battery Pack Applications.* Battery Power Products & Technology, 2007.

[10] D. V. Comiskey, *Practical Guidelines to Designing an EMI Compliant PoE Powered Device with Isolated Flyback.* TI Literature SLUA469, 2008.

[11] *200 W Audio Amplifier Power Supply.* Power Integrations Reference Design Report RDR-203, 2009.

[12] W. Mcmurray. Selection of snubbers and clamps to optimize the design of transistor switching converters. *IEEE Trans. Ind. Appl*, IA-16, pp. 513-523, July-August 1980.

[13] N. P. Papanikolaou and E. C. Tatakis. Active voltage clamp in flyback converters operating in CCM mode under wide load variation. *IEEE Trans. Ind. Electron.*, 51, no. 3, pp. 632-640, June 2004.

[14] A. Hren, J. Korelic, and M. Milanovic. RC-RCD clamp circuit for ringing losses reduction in a flyback converter. *IEEE Trans. Circuits and Systems-II: Express Briefs*, 53, no. 5, pp. 369-373, May 2006.

[15] T. Ninomiya, T. Tanaka, and K. Harada. Analysis and optimization of a nondissipative LC turn-off snubber. *IEEE Trans. Power Electron.*, 3, no. 2, pp. 147-156, April 1998.

[16] S. B. Yaakov and G. Ivensky. Passive lossless snubbers for high frequency PWM converters. In *IEEE Appl. Power Electron. Conf.,* Dallas, TX, Mar., 1999.

[17] B. Carsten. Design techniques for transformer active reset circuits at high frequency and power levels. In *Proc. High Freq. Power Conversion Conf.,* pp. 235-245, 1990.

[18] R. Watson, F. C. Lee, and G. C. Hua. Utilization of an active clamp circuit to achieve soft switching in flyback converters. *IEEE Trans. Power Electron.*, 11, no. 1, pp. 162-169, January 1996.

[19] H. Chung, S. Y. Hui, and W. H. Wang. An isolated ZVS/ZCS flyback converter using the leakage inductance of the coupled inductor. *IEEE Trans. Ind. Electron.*, 45, no. 4, pp. 679-682, August 1998.

[20] H. Chung, S. Y. Hui, and W. H. Wang. A zero-current-switching PWM flyback converter with a simple auxiliary switch. *IEEE Trans. Power. Electron.*, 14, no. 2, pp. 329-342, March 1999.

[21] B.-R. Lin and F.-Y. Hsieh. Soft-switching zeta-flyback converter with a buck-boost type of active clamp. *IEEE Trans. Ind. Electron.*, 54, no. 5, pp. 2813-2822, October 2007.

[22] C. M. Wang. A novel ZCS-PWM flyback converter with a simple ZCS PWM commutation cell. *IEEE Trans. Ind. Electron.*, 55, no. 2, pp. 749-757, February 2008.

[23] E. Adib and H. Farzanehfard. Family of zero-current transition PWM converters. *IEEE Trans. Ind. Electron.*, 55, no. 8, pp. 3055-3063, August 2008.

[24] E. Bennett and S. C. Larson. Effective resistance to alternating currents of multilayer winding. *Trans. Amer. Inst. Elect. Eng.*, 55, pp. 1010-1017, August 1940.

[25] P. J. Dowell. Effects of eddy currents in transformer winding. *Proc. IEE*, 113, no. 8, pp. 1387-1394, August 1966.

[26] M. P. Perry. Multiple layer series connected winding design for minimum losses. *IEEE Trans. Power Appr. Syst.*, PAS-98, no. 1, pp. 116-123, January/February 1979.

[27] P. S. Venkataraman. Winding eddy current losses in switch mode power transformers due to rectangular wave currents. In *Proc. Powercon 11,* Section A-1, 1984, pp. 1-11.

[28] B. Carsten. High frequency conductor losses in switch mode magnetics. In *Proc. PCI,* Munich, Germany, 1986, pp. 161-182.

[29] J. Jongsma. High frequency ferrite power transformer and choke design, part 3: Transformer winding design, part 4: Improved method of power choke design. Technical report, Philips Electronic Components and Materials, Technical Publication, no. 27, Philips, The Netherlands, 1986.

[30] J. P. Vandalec and P. D. Ziogos. A novel approach for minimizing high frequency transformer copper loss. *IEEE Trans. Power Electron.*, 3, no. 3, pp. 266-276, July 1988.

[31] J. Rosa. Calculation of flux linkages in multiwinding transformers. In *IEEE Power Electron. Spec. Conf.,* 86CH2310-1, 1986, pp. 639-644.

[32] N. R. Coonrod. Transformer computer design aid for higher frequency switching power supplies. In *IEEE Power Electron. Spec. Conf.,* 84CH2000-8, 1984, pp. 257-267.

[33] W. G. Hurley, W. Wölfle, and J. G. Breslin. Optimized transformer design: Inclusive of high-frequency effects. *IEEE Trans. Power Electron.*, 13, no. 4, pp. 369-376, July 1999.

[34] W. G. Hurley, E. Gath, and J. G. Breslin. Optimizing the ac resistance of multilayer transformer windings with arbitrary current waveforms. *IEEE Trans. Power Electron.*, 15, no. 2, pp. 369-376, March 2000.

[35] A. M. Urling, V. A. Niemela, G. R. Skutt, and T. G. Wilson. Characterizing high-frequency effects in transformer windings - a guide to several significant articles. In *IEEE Appl. Power Electron. Conf.,* 84CH2000-8, March, 1989, pp. 373-385.

[36] R. Petkov. Optimized design of a high-power high-frequency transformer. *IEEE Trans. Power Electron.*, 11, no. 1, pp. 33-42, January 1996.

[37] M. Bartoli, N. Noferi, A. Reatti, and M. K. Kazimierczuk. Modeling winding losses in high-frequency power inductors. *Journal of Circuits, Systems and Computers*, 5, no. 4, pp. 607-626, December 1995.

[38] M. Bartoli, N. Noferi, A. Reatti, and M. K. Kazimierczuk. Modeling litz-wire winding losses in high-frequency power inductors. In *IEEE Power Electron. Spec. Conf.,* June, 1996, pp. 1690-1696.

[39] W. T. McLyman, *Transformer and Inductor Design Handbook.* 3rd Ed., Marcel Dekker, New York, 2004.

[40] G. Wolf. Mains isolating switch-mode power supply. Technical report, Philips Electronic Application Bulletin, vol. 32, no. 1, February, 1973.

[41] D. Skendzic. Two transistor flyback converter design for EMI control. In *IEEE Int. Symposium on Emag. Comp.,* August, 1990, pp. 130-133.

Relevant Publications

Peer-reviewed Journal Articles

1. Dakshina Murthy Bellur and Marian K. Kazimierczuk, Harmonic winding loss in buck DC-DC converter for discontinuous conduction mode, *IET Power Electronics, accepted for publication*, vol. 3, 2010.

2. Dakshina Murthy Bellur and Marian K. Kazimierczuk, Two-switch flyback PWM DC-DC converter in discontinuous-conduction mode, *International Journal of Circuit Theory and Application, accepted for publication*, vol. 38, 2010, early view published online in Wiley Interscience (www.interscience.wiley.com). DOI: 10.1002/cta.672.

3. Dakshina Murthy Bellur and Marian K. Kazimierczuk, Winding loss due to harmonics in high frequency transformers for DC-DC converters in discontinuous conduction mode, *IET Power Electronics, accepted for publication*, vol. 4, 2011.

4. Dakshina Murthy Bellur and Marian K. Kazimierczuk, Two-switch flyback PWM DC-DC converter in continuous-conduction mode, *International Journal of Circuit Theory and Applications, accepted for publication*, vol. 38, 2010.

5. Dakshina Murthy Bellur and Marian K. Kazimierczuk, Two-transistor Zeta-flyback DC-DC converter with reduced transistor voltage stress, *IET Electronics Letters*, vol. 46, no. 10, 2010, pp. 719-720.

Conference Proceedings

1. Dakshina Murthy Bellur and Marian K. Kazimierczuk, Two-switch flyback-forward PWM DC-DC converter with reduced switch voltage stress, *IEEE International Symposium on Circuits and Systems*, Paris, May 30-June 2, 2010, pp. 3705-3708.

2. Dakshina Murthy Bellur and Marian K. Kazimierczuk, Review of zero-current switching flyback PWM DC-DC converters, *Proceedings of Electrical Insulation Conference and Electrical Manufacturing Expo*, Nashville, TN, September 29-October 1, 2009.

3. Dakshina Murthy Bellur and Marian K. Kazimierczuk, PSpice and MATLAB applications in teaching power electronics to graduate students at Wright State University, *ASEE North Central Section Conference*, Dayton, OH, March, 2008.

4. Dakshina M. Bellur and Marian K. Kazimierczuk, DC-DC converters in electric vehicle applications, *Proceedings of Electrical Insulation Conference and Electrical Manufacturing Expo*, Nashville, TN, October, 2007, pp. 286-293.

5. Dakshina Murthy Bellur and Marian K. Kazimierczuk, Active-clamp circuits for flyback PWM DC-DC converter, *Proceedings of Electrical Insulation Conference and Electrical Manufacturing Expo*, Indianapolis, IN, September, 2006.

6. Dakshina Murthy and Marian K. Kazimierczuk, Performance evaluation of flyback converter, *Proceedings of Electrical Insulation Conference and Electrical Manufacturing Expo*, Indianapolis, IN, October, 2005, pp. 408-416.

Author's Biography

Dakshina Murthy Bellur was born in Gubbi, Karnataka, India on the first day of January, 1981. He received the B.E. degree in electrical engineering from Visvesvaraya Technological University, Belgaum, India in 2003, and M.S. and Ph.D. degrees in electrical engineering from Wright State University (WSU), Dayton, OH in 2006 and 2010, respectively.

From 2005 to 2006, he was a Lab Teaching Assistant, and from 2006 to 2010, a Graduate Teaching and Research Assistant with the Department of Electrical Engineering, Wright State University, Dayton, OH. He was a summer research intern at Cummins Power Generation, Minneapolis, MN from June 2008 to September 2008. His research interest include PWM DC-DC converters, resonant converters, high-frequency magnetics, power semiconductor devices, renewable energy systems, energy harvesting, and engineering education.

The author is a member of Phi Kappa Phi, student member of IEEE, IEEE Circuits and Systems Society (CAS), and Electrical Manufacturing and Coil Winding Association (EMCWA). He was a session chair of the 2008 ASEE North Central Section Conference. He was the recipient of the Excellence in Teaching Award for teaching assistants, College of Engineering and Computer Science, WSU in 2008 and also the recipient of the Outstanding Graduate Student in Engineering Award, School of Graduate Studies, WSU in 2010.